THESE DE DOCTORAT DE
L'UNIVERSITE PIERRE ET MARIE CURIE

Spécialité

Mécanique des fluides
(Ecole doctorale SMAER)

Présentée par

M. Zhenlan GAO

Pour obtenir le grade de

DOCTEUR de l'UNIVERSITÉ PIERRE ET MARIE CURIE

Sujet de la thèse :

Transition to chaos of natural convection between two vertical differentially heated plates

soutenue le 18 novembre 2013

devant le jury composé de : (préciser la qualité de chacun des membres).

Mme Bérengère Podvin	Chargé de Recherche CNRS	Directrice de thèse
Mme Anne Sergent	Maître de conférences	Co-encadrante de thèse
M. Daniel Henry	Directeur de Recherche CNRS	Rapporteur
M. Innocent Mutabazi	Professeur des Universités	Rapporteur
M. François Charru	Professeur des Universités	Membre de jury
M. Patrick Le Quéré	Directeur de Recherche CNRS	Membre de jury
M. Maurice Rossi	Professeur des Universités	Président de jury
Mme Laurette S. Tuckerman	Directeur de Recherche CNRS	Membre de jury
M. Shihe Xin	Professeur des Universités	Invité

Zhenlan GAO

Etude des instabilités de la convection naturelle entre deux plaques verticales différentiellement chauffées

Résumé

La transition vers le chaos de la convection naturelle d'air entre deux plaques infinies verticales différentiellement chauffées est étudiée. La première instabilité est une bifurcation de fourche conduisant à des rouleaux 2D. L'équation de Ginzburg-Landau est dérivée pour cette première bifurcation et comparée aux résultats de la DNS. La DNS 2D montre que les rouleaux sont instables via une bifurcation de Hopf. L'écoulement devient ensuite quasipériodique puis chaotique. A plus haut Rayleigh (Ra), l'écoulement redevient stationnaire. La DNS dans une configuration 3D comprenant quatre rouleaux verticaux, mais de petite dimension transverse, montre que les rouleaux 2D deviennent 3D par une bifurcation de fourche. Puis l'écoulement devient oscillant via une bifurcation de Hopf. On observe une cascade de doublement de période des motifs 3D, dominée par un mécanisme de modulation du nombre des rouleaux. Lorsqu'un seul rouleau est considéré, le scénario sous-harmonique devient persistant et conduit au chaos. A plus grand Ra, on oberve une intermittence de crise, correspondant au déplacement du rouleau d'une demi-hauteur. L'analyse de stabilité linéaire des rouleaux est effectuée avec la méthode d'Arnoldi. Les résultats sont comparés avec la simulation nonlinéaire dans un domaine de grande dimension transverse. Les rouleaux 2D bifurquent vers un état 3D composé de rouleaux ondulés, qui devienent ensuite des rouleaux brisés. L'écoulement devient oscillant via une bifurcation de Hopf. A plus haut Rayleigh une bifurcation sous-harmonique est observée, qui conduit au chaos temporel.

Mots-clés : convection naturelle, instabilités, bifurcation, chaos, simulation numérique directe (DNS)

Résumé en anglais

The transition to chaos of the natural convection of air between two infinite differentially heated vertical plates is studied. The first instability is a pitchfork bifurcation leading to steady 2D rolls. A Ginzburg-Landau equation is derived analytically for the flow around the first bifurcation and compared with DNS results. 2D DNS shows that rolls become unstable via a Hopf bifurcation. At higher Rayleigh numbers, the flow becomes quasiperiodic then chaotic. At still higher Rayleigh numbers the flow becomes steady again. DNS in a 3D configuration with a small transverse extent shows that 2D rolls undergo another pitchfork bifurcation to a 3D pattern, which consists of deformed rolls connected by counter-rotating vortices. The flow then becomes oscillatory via a Hopf bifurcation. Chaotic behavior subsequently occurs through a sequence of period-doubling bifurcations, which gives way to a spatial modulation pattern. When only one roll is allowed in the domain, the cascade of period-doubling bifurcations becomes persistent, leading the flow to temporal chaos. At higher Ra, a crisis-induced intermittency is observed, as the flow structures shift vertically by half a vertical wavelength. We use the Arnoldi method to determine the unstable transverse wavenumbers. 3D DNS in a domain of large extent shos that the 2D rolls bifurcate to a steady 3D pattern consisting of pinched rolls, which gives way to broken rolls. Then the flow becomes oscillatory via a Hopf bifurcation. Subsequently, a period-doubling bifurcation is observed, and eventually the flow becomes temporally chaotic.

Keywords : natural convection, instabilities, bifurcation, chaos, direct numerical simulation (DNS)

Acknowledgment

First of all, I would like to express my sincere gratitude to my principal advisor, Mrs. Bérengère Podvin, for the energy and time that she devoted during the three years. I have greatly benefitted from her incredible insight and intuition, as well as her patience. Her guidance helped me in all the time of research and writing of this thesis.

Secondly, I want to thank Mrs. Anne Sergent, my second advisor. Her investment at the beginning helped me rapidly master the numerical technics, which constitutes an essential good starting point for my Ph.D study. Without her continuous support, I could not finish my thesis within three years.

I need to thank Mr. Shihe Xin, who generously provides me his several codes. He spent a lot of time to debug the parallelization algorithm and the Arnoldi method in the specific configuration I studied. I would like also to thank Mr. Patrick Le Quéré, who offers me one of his codes written about 20 years ago in FORTRAN 77 with very well written documentation. It helps me quickly understand the numerical methods for fluid mechanics.

I am grateful for the help of Mrs. Laurette S. Tuckerman, who helped me a lot for the research and writing of my first publication, especially for her enthusiasm, motivation, and immense knowledge and ideas.

I would like to thank my two rapporteurs: Mr. Daniel Henry and Mr. Innocent Mutabazi, for their careful lecture of my thesis and the important comments for improvement. My gratitude also goes to other committees of my final defense: Mr. Maurice Rossi and Mr. François Charru, for their encouragement, questions, and insightful comments.

My sincere thanks also go to Mr. Jalel Chergui, Mr. Anh-Tuan Dang, and the colleagues in AMIC. Without their technical support, I cannot obtain some many interesting results. I need especially to thank Mr. Jalel Chergui, for his continuous support, even sometimes the questions are quite naive.

Besides these persons mentioned above, I need to thank my laboratory LIMSI-CNRS, for the financial support of training courses in CNRS, the summer schools, several national and international conferences, *etc.* My thanks go to my fellow labmates in LIMSI as well. They are Jeremy Basley, Laurent Cadet, Loic Cappanera, Christelle Douay, Atam Ercan, Charles Garnier,

Florimond Guéniat, Lyes Kahouadji, Franky Luddens, Lin Ma, Huong-Lan Tran, Julie Tryoen, Ludomir Oteski, Bejamin Piton, Richard Paridaens, Guillaume Prigent, Sébastien Wullens and other colleagues. Thanks to them, the three years in LIMSI was colorful.

I would never forget the supports of my old friends in Arts et Metiers ParisTech as well, especially the one from Mr. Zhaopeng Qiu, Mr. Kai Pan, and my ancien Mr. Samuel Bernard. I would like to thank Mrs. Ping Huang-Lisle in ParisTech international office for her suggestions since my arrival in France.

Last but not the least, I would like to thank my parents, for their endless love and support throughout my life.

Most of the simulations were carried out on the superclusters in IDRIS-CNRS under the project DARI0326.

Contents

Chapter 1

Introduction

Natural convection in a fluid layer between two differentially heated plates is of substantial interest for many industrial applications, such as heat exchangers in reactors or insulation of buildings (e.g. double-paned windows). In the classic Rayleigh-Bénard convection, the fluid lies between two horizontal plates and is heated from below so that the thermal gradient is opposite to the direction of gravity. It has drawn sustained attention for more than one hundred years [1, 2, 3]. The second most studied configuration is a fluid layer between two vertical plates maintained at different temperatures. In this configuration, the thermal gradient is orthogonal to the direction of gravity. A number of studies have shed some light on its specific dynamics, since Batchelor's pioneering work [4], but most of these studies are two-dimensional. The detailed sequence of bifurcations leading to chaos in the 3D configuration has not yet been established, which constitutes the essential interest of the present thesis. In this chapter, we firstly present the physical problem, then review significant previous studies on the subject, and then we give an outline of our work and show how it constitutes a complementary contribution to the existing body of knowledge.

1.1 Physical Problem

We consider the flow of air between two infinite vertical plates maintained at different temperatures. The configuration is represented in Figure 1.1. The distance between the two plates is D, the periodic height and depth of the plates are L_z and L_y respectively. The temperature difference between the plates is set to ΔT. The x direction is normal to the plates, y represents the transverse direction, and the gravity g is opposite to the vertical direction z.

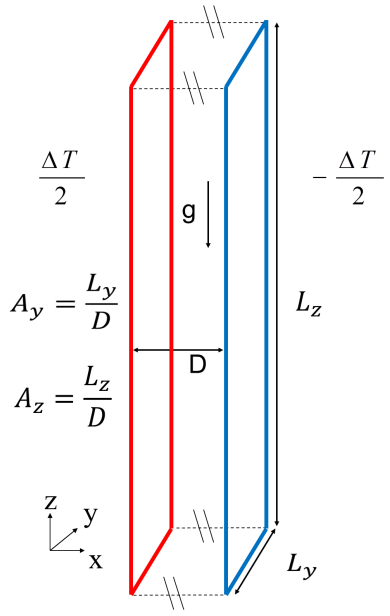

Figure 1.1: Study domain

The Boussinesq approximation is used to study this problem, which means that all the fluid properties such as the kinetic viscosity ν, thermal diffusivity κ, and thermal expansion coefficient β are constant. Density variations are neglected in the mass conservation equation so that the velocity field is assumed to have a zero divergence. Density variations appear only in the buoyant term of the momentum conservation equation, where the density varies as a linear function of temperature.

Four nondimensional parameters characterize the flow: the Prandtl number $Pr = \nu/\kappa$, which represents the ratio between the viscous and the thermal diffusion; the transverse and vertical aspect ratios $A_y = L_y/D$ and $A_z = L_z/D$ (A_y does not appear in two-dimensional studies); and the Rayleigh number based on the gap between the two plates $Ra = \frac{g\beta\Delta T D^3}{\nu\kappa}$, which represents the ratio between the buoyancy effect and the diffusive effects. Only the Rayleigh number dependence is considered in the present study. The Prandtl number is fixed and equal to 0.71, since most of the previous studies are concerned with gases with $Pr = 0.71$, such as air.

The flow is governed by the Navier-Stokes equations within the Boussinesq approximation. We choose the reference parameters to be $\frac{\kappa}{D}\sqrt{Ra}$ for the velocity, D for the length, and ΔT for

the temperature. Then the nondimensionalized equations are:

$$\nabla \cdot \vec{u} = 0 \tag{1.1}$$

$$\frac{\partial \vec{u}}{\partial t} + \vec{u} \cdot \nabla \vec{u} = -\nabla \tilde{p} + \frac{Pr}{\sqrt{Ra}} \Delta \vec{u} + Pr \tilde{\theta} \hat{z} \tag{1.2}$$

$$\frac{\partial \tilde{\theta}}{\partial t} + \vec{u} \cdot \nabla \tilde{\theta} = \frac{1}{\sqrt{Ra}} \Delta \tilde{\theta} \tag{1.3}$$

with Dirichlet boundary conditions at the plates

$$\vec{u}(0, y, z, t) = \vec{u}(1, y, z, t) = 0, \quad \tilde{\theta}(0, y, z, t) = 0.5, \quad \tilde{\theta}(1, y, z, t) = -0.5 \tag{1.4}$$

and periodic conditions in the y and z directions. Here t denotes time, $\vec{u} = (u, v, w)$ is the velocity vector, p is the pressure, θ is the temperature.

1.2 State of the Art

The natural convection heated from the sidewalls was first studied by Batchelor [4]. Experimental studies are necessarily conducted in cavities of finite aspect ratios, while early linear stability analyses were applied to an infinite configuration. The effect of horizontal boundaries was accounted for in such studies by a positive temperature stratification [5]. A large number of studies have been devoted to the case of the cavities with different aspect ratios [4, 6, 7, 8]. The case we study here is that of infinite plates with no stratification, which is likely to be a model of a very tall cavity.

1.2.1 Laminar region

Batchelor's study [4] of the flow in a vertical differentially heated 2D slot is considered to be the first work on this subject. He came to the conclusion that the laminar flow regime depends only on the Rayleigh number and aspect ratio of the cavity. In the experimental investigation of Eckert and Carlson [9], the flow was classified into three regimes: if Ra is small (conduction regime), the fluid temperature is independent of height, and heat is transferred between the

two vertical walls by conduction. The velocity profile has a centro-symmetric (cubic) form. As Ra increases, a stable vertical temperature gradient develops in the core of the flow, and the vertical velocity progressively decreases. This is called the transition regime. Finally, if Ra is sufficiently large, the flow is almost completely confined in the boundary layers at the walls, and the dominant mode of heat transfer is convection. This regime is referred to as the convective regime.

1.2.2 Early experimental investigations

The first investigations about the transition of natural convection between differentially heated vertical plates relied on experimental descriptions. Elder [10] observed the onset of secondary flow and 'cat's-eyes' tertiary flow in his experiments with two fluids: paraffin and silicone oil. Vest and Arpaci [11] observed the onset of secondary convection in air flow, and compared it with their calculations of secondary flow stream patterns as shown in Figure 1.2. Oshima [12] considered convection in a rectangular water-filled cavity heated through two vertical side-walls. He observed the development of the wavy motions of streamlines into rows of periodic vortices, which then burst into turbulence.

1.2.3 2D linear stability analysis

Early computations of the flow structure were based on stability analysis in the neighbourhood of the critical Rayleigh number Ra_c and were limited to the 2D case. Vest and Arpaci [11] relied on 2D linear stability to calculate secondary-flow stream patterns. Gill and Davey [5] focused on the mechanism due to the buoyancy-driven instability, and showed that the nature of instabilities (with respect to stationary or traveling wave disturbances) depended on the Rayleigh number, aspect ratio, and Prandtl number, in the case of vertical differentially heated slot. Korpela [13] carried out the linear stability dependence analysis on the Prandtl number. He found that the critical disturbance modes are hydrodynamically driven and stationary when $Pr < 12.45$, while they are thermally driven and oscillatory when $Pr > 12.45$. Bergholz [14] investigated the 2D linear stability of the flow for different Prandtl numbers and different vertical

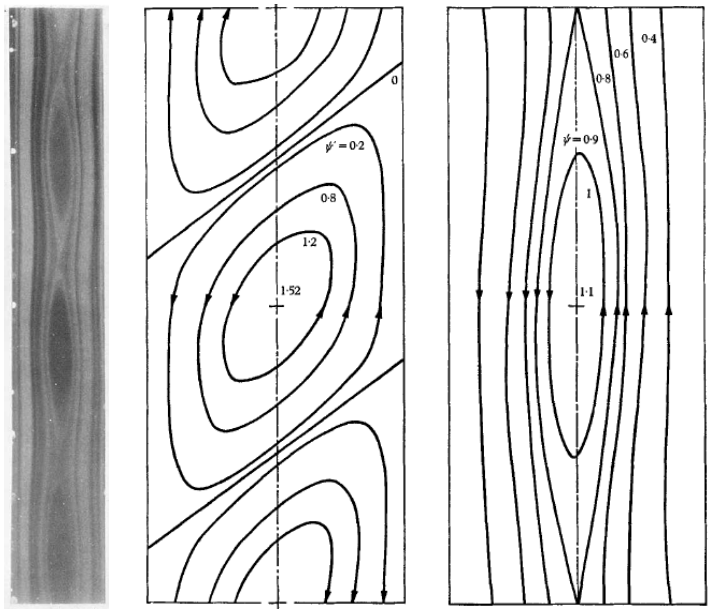

(a) (b) (c)

Figure 1.2: (a) Streak photograph of convection rolls from experiment at $Gr = 9500$, $A_z = 33$, $Pr = 0.71$. Streamline pattern obtained by numerical calculation. (b) Disturbance. (c) Total flow at $Gr = 7877$, $Pr = 0.71$. Vest and Aparci J. Fluid Mech. 1969 [11]

thermal stratifications which model the effect of a finite vertical aspect ratio. It was found that in the small Pr regime, the nature of instability is changed from stationary to oscillatory, as the vertical thermal stratification exceeds a certain magnitude. On the other hand, in the large Pr regime, the transition is from traveling-wave to stationary instability with increasing stratification. Tao and Zhuang [15] carried out the analysis of different instability mechanisms occurring in cavities. They found that secondary rolls and traveling waves are absolutely and convectively unstable, respectively.

1.2.4 2D nonlinear studies

Weakly nonlinear stability calculations in 2D were carried out in [16, 17, 18]. Daniels and Weinstein [16] obtained an amplitude equation at high Rayleigh number and large Prandtl number, with the presence of a vertical thermal stratification, in which case the unstable disturbance modes are stationary. Cornet and Lamarque [17] worked on the case of air ($Pr = 0.71$), and obtained the perturbation amplitude around the first instability, but there was at that

time no available numerical or experimental data with which to compare. A similar analysis for water ($Pr = 7.5$) was carried out by Mizushima and Gotoh [18]. They showed that the curve of the mean Nusselt number Nu versus Grashof number Gr had a small hump at the critical Grashof number Gr_c instead of having a constant positive slope (Figure 1.3). A Newton-Raphson method to compute equilibria was used by Mizushima and Saito [19] in the zero-Prandtl-number limit. Mizushima [20] extended this analysis to secondary equilibrium solutions for various values of Prandtl number. More bifurcation diagrams were obtained in the case of air by Mizushima and Tanaka [21, 22] for subsequent bifurcations. They obtained a very complicated bifurcation diagram, which showed that the bifurcation structure of the steady-state solution is composed of a smooth transition and a saddle-node branch. The change of flow pattern is due to the transition from the saddle-node branch to the smooth transition branch.

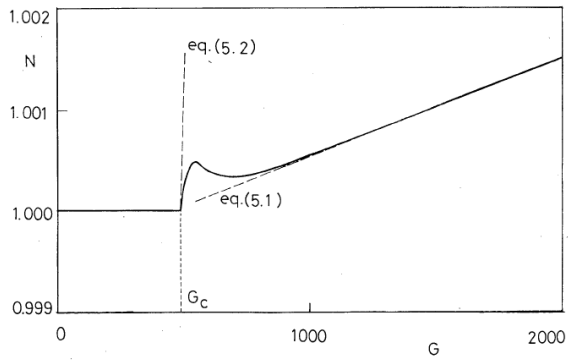

Figure 1.3: Mean Nusselt number vs Gr, $Pr = 7.5$. Mizushima and Gotoh, *J. Phys. Soc. Japan*, 1983 [18]

The agreement between the patterns predicted by theory and experimental observations of the first instabilities suggests that convection between 2D infinite plates is a good representation of what happens in tall cavities. However, there is some evidence that these simplified assumptions may not provide an accurate picture of the real dynamics. Firstly, the influence of the aspect ratio - what exactly makes a cavity "tall enough" - may be difficult to determine intuitively. From Bergholz [14], it can be seen that the nature of the most unstable disturbances for water ($Pr = 7.5$) switches from a stationary to a traveling state for a critical aspect ratio

$A \sim 70$. Moreover, the nature of the higher-order bifurcations is likely to be affected by the presence of horizontal boundaries. Xin [23] carried out 2D numerical simulations of natural convection of air in a confined cavity as well as between infinite plates (a channel). Transition to the chaotic state was observed at a relatively low Rayleigh number in the cavity, while only regular patterns could be obtained in the channel.

1.2.5 Recent 3D experimental investigations

Although most numerical simulations [24, 25, 26, 27, 28, 29] have been carried out in the 2D case, there is evidence that the flow becomes rapidly three-dimensional as the Rayleigh (or Grashof) number increases, as was observed by Wright *et al.* [30] in their experiments for tall air-filled cavities with an aspect ratio $A_z = 40.8$. They observed several regimes in the procedure of transition as shown in Figure 1.4. When Ra is between 4850 and 6220, the flow is in the conduction regime. When $Ra \sim 6800$, the secondary flow appears, which is characterized by co-rotating rolls. A downward motion of the secondary cells is observed at the small rate $v_{cell} \sim 3.4mm/s$ ($v^\star = 0.07$ scaled with the reference velocity $\sqrt{g\beta\Delta TL}$). The secondary flow is stable for $Ra \sim 7300 - 8600$, with a downward velocity $v_{cell} \sim 9.8mm/s$ ($v^\star = 0.17$) for the co-rotating rolls. When Ra is increased to $9600 - 10500$, the secondary flow becomes unstable. The secondary cells move and rotate faster and impact the adjacent fluid. The cells no longer always move downward. Occasional interactions between the rolls are also observed. For $Ra \sim 11600 - 12600$, the flow becomes 3D, with cells of variable sizes and shapes, and random movements. At $Ra \sim 13600 - 54800$, the flow transits to full turbulence. The flow in this regime consists of both co-rotating, counter-rotating cells, and paired cells. Their length scales are generally smaller than the secondary rolls observed at lower Ra. The downward motion of secondary cells was also independently observed by Lartigue *et al.* [29]. However, the dimensionless downward velocities obtained numerically (2D) and experimentally are respectively $v^\star = 0.0110$ and $v^\star = 0.0107$ at $Ra = 9222$ which are much lower than values obtained by Wright *et al.* [30] at even higher Rayleigh numbers. No physical explanation was available for this disagreement.

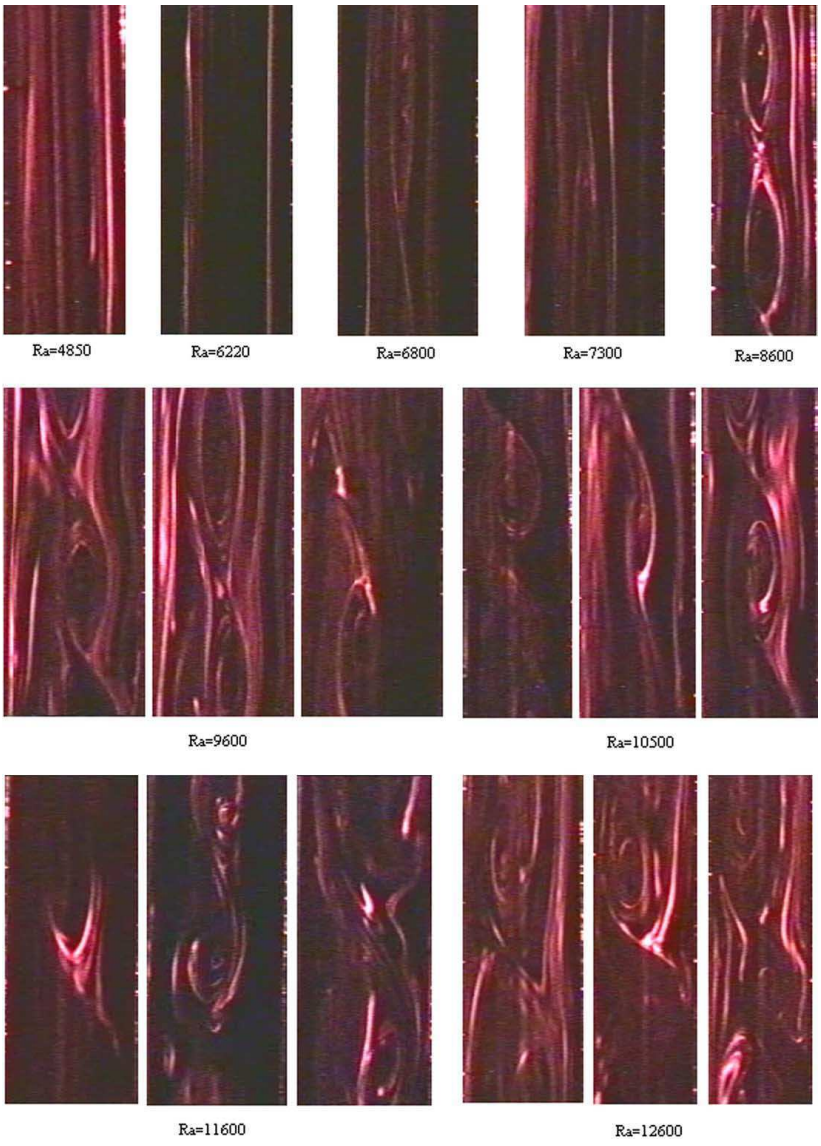

Figure 1.4: Streak flow pattern at *Ra* from 4850 to 12 600. Wright *et al.* Int. J. Heat Mass Trans. 2006 [30]

1.2.6 3D numerical studies

Experimental observations agree with several 3D linear stability calculations [31, 32], which predicted that the flow in a tall air-filled cavity should become rapidly three-dimensional. Nagata and Busse [31] considered a shear layer of fluid with sidewalls at different temperatures. Their 3D computations of equilibria were performed in the limit of vanishing Prandtl number. Since $Pr = 0$, the velocity of the base flow has a cubic profil and the first instability should be associated with a stationary disturbance. (In the case $Pr \neq 0$, the nature of the first instability could be a traveling wave.) The stability diagram for the secondary rolls shows the limits of the Eckhaus instability, a monotone instability, and an oscillatory instability. A steady 3D pattern was found to be associated with the secondary monotone instability as shown in Figure 1.5 (a). The growth rate of the 3D pattern was found to be weakly dependent on k_z, the vertical wavenumber of the primary rolls, and the growth rates are only positive for a finite range of transverse wavenumber k_y. They also found that although the critical transverse wavenumber k_{yc} was found to be about 1.6 at $k_z = 2.8$, when the vertical wavenumber of primary rolls was set to $k_z = 2.6$, $k_y = 2.0$ is preferred at higher Gr. They also explored the perturbation associated with the oscillatory instability (Figure 1.5 (b)), where the waves propagate in the positive or the negative y-directions. They noted that the existence of this oscillatory pattern is improbable, since the steady 3D pattern associated with the monotone instability already gives way to a new 3D pattern before Ra reaches the limit of the oscillatory instability [31]. This new 3D pattern shifts backward and forward periodically in time and has a wavelength twice that of the steady 3D flow in the spanwise direction, due to a subharmonic instability.

By the same method as Nagata and Busse [31], Chait and Korpela [32] analyzed the stability of the secondary flow in a vertical enclosure filled with air at $Pr = 0.71$. Besides the monotone instability found by Nagata and Busse [31], which was noted as monotone instability A, they found another monotone instability, which was referred to as monotone instability B in their paper. The occurence of these two kinds of monotone instability as well as the Eckhaus instability depends on the wavenumbers of primary rolls in the vertical direction as shown in the stability diagram (Figure 1.6). In fact, the stability curve of monotone instability A con-

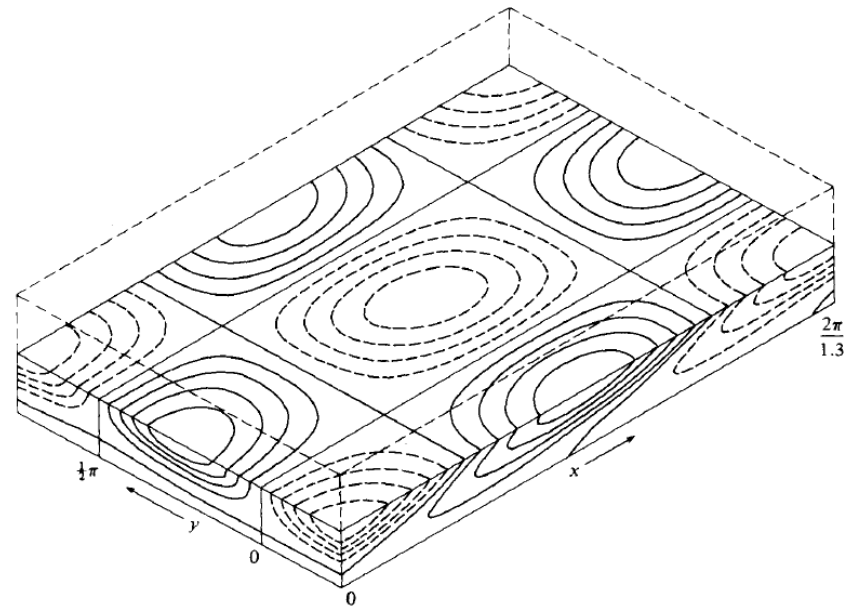

(a)

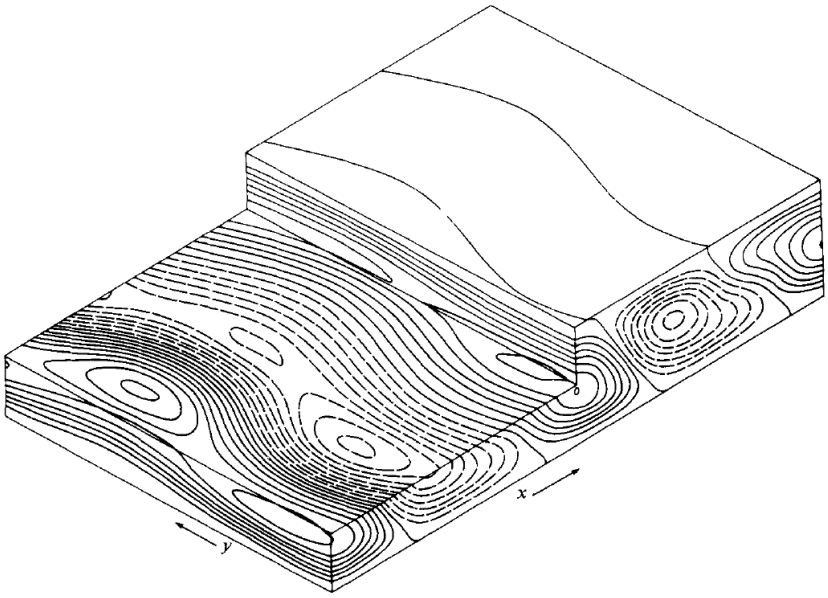

(b)

Figure 1.5: Vertical velocity isocontours of 3D flow pattern: (a) steady 3D pattern associated with the monotone instability, (b) 3D perturbation pattern associated with the oscillatory instability. (Note: the x direction in their paper is the vertical direction z in our configuration.) Nagata and Busse J. Fluid Mech. 1983 [31]

strains the domain of stable rolls from above while the neutral curve of monotone instability B originates in the vicinity of the critical point ($k_{zc} = 2.81$ and $Gr_c = 8037$). To the left of it, i.e. for lower wavenumbers, the primary rolls are unstable. The characteristic wavelength of the 3D pattern associated with the monotone B instability was found to be much larger than the original wavelength of the 2D rolls ($k_z = k_{zc} + \Delta k_z$, where $\Delta k_z = 0.6$, and $k_y = 0.4$ for Gr up to 9000). The corresponding pattern consists of periodic thickening and thinning secondary rolls in the transverse direction y, which resembles the skewed varicose instability in Rayleigh-Bénard convection.

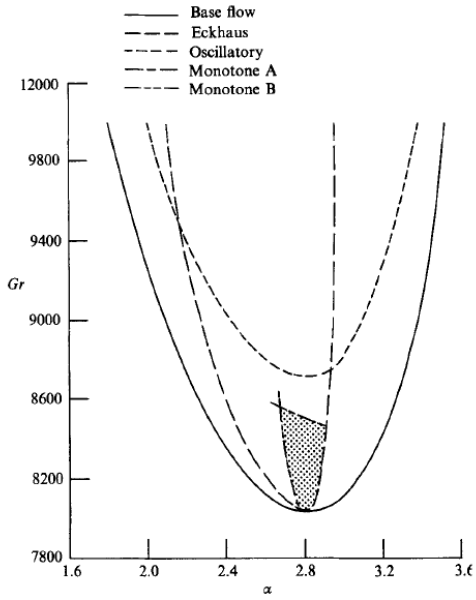

Figure 1.6: Stability diagram of the multicellular flow for air ($Pr = 0.71$). The shaded area represents the domain of stable secondary rolls. (Note: α in the figure corresponds to k_z in our notation.) Chait and Korpela J. Fluid Mech. 1989 [32]

Clever and Busse [33] carried out a successive stability analysis of the air flow ($Pr = 0.71$) by following the same approach as Nagata *et al.* [31] and Chait *et al.* [32], with the consideration of the possible symmetries of the tertiary and quarternary flow. They identified a steady 3D pattern, which consists of staggered vortices. It then bifurcated into a traveling wave of invariant shape at higher Rayleigh numbers as shown in Figure 1.7. The corresponding motion of the traveling wave was downward, which seems to be in agreement with the experimental results of Wright *et al.* [30] and experimental and numerical results by Lartigue *et al.* [29]. However,

the moving pattern obtained numerically by Clever and Busse [33] is 3D, while the descending rolls are 2D in the observations of Wright *et al.* [30] and Lartigue *et al.* [29]. Moreover, this invariant traveling pattern is different from the oscillatory, quarternary flow found by Nagata and Busse [31] for the limiting case of $Pr = 0$. Additionally, Clever and Busse [33] measured the Nusselt number at the wall and found that the 3D pattern flow is less efficient for the heat transfer than the secondary co-rotating roll.

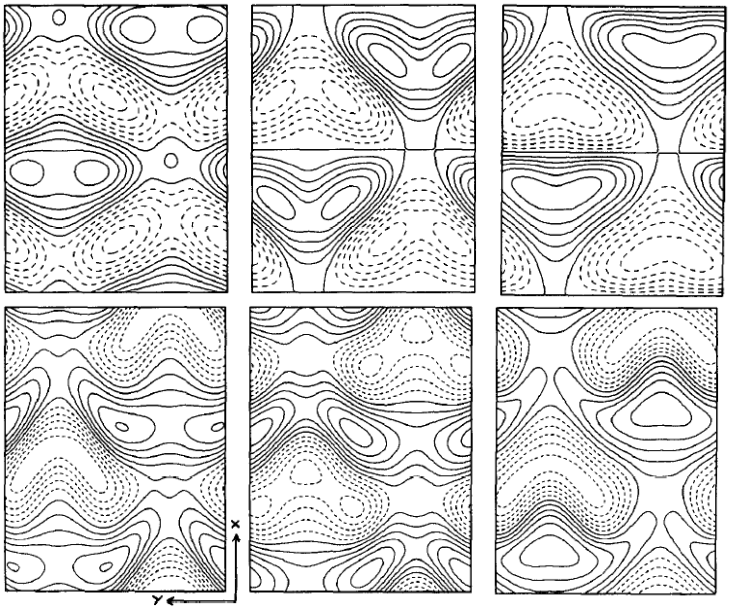

Figure 1.7: Three dimensional flow pattern. Isocontours of horizontal velocity u in planes $x = 0.3$ (left), $x = 0$ (middle), and $x = -0.3$ (right). Upper row: stable tertiary flow pattern; Botton row: drifting quarternary flow pattern. (Note: the x direction in their paper is the vertical direction z in our configuration.) Clever and Busse, Chaos Sol. Frac. 1995 [33]

1.2.7 Non-Boussinesq approach

A Ginzburg-Landau model was used by Suslov and Paolucci [34, 35] to describe the three-dimensional flow between infinite plates in the case of non-Boussinesq convection for a variety of Prandtl numbers. However, the approach remains limited to a region around the critical Rayleigh number.

1.2.8 Transition to chaos

Theoretically, several theoretical models of the transition to chaos were proposed for dissipative dynamical systems [36]. Some of them have been observed in Rayleigh-Bénard convection experiments. Quasi-periodicity and a sequence of period-doubling bifurcations were observed by Maurer and Libchaber [37] and by Giglio, Musazzi and Perini [38]. Pomeau and Manneville [39] proposed the intermittency scenario as a possible route to chaos. They classified the intermittency into three types, by the way in which the Floquet multiplier crosses the unit circle. In the Rayleigh-Bénard convection experiment carried out by Bergé *et al.* [40], Pomeau-Manneville type-I intermittency was observed.

The route to chaos and chaotic behavior of the flow in laterally and differentially heated cavities with adiabatic horizontal walls has attracted some attention as well [6, 7, 8, 41, 42]. These studies were carried out at very large Rayleigh number ($Ra > 10^8$) and were usually limited to 2D. Paolucci and Chenoweth [6] found that the route to chaos in the cavity with small aspect ratios (about 1/2 to 3) is through a Hopf bifurcation, then quasi-periodicity. This is also reported by Le Quéré [7] as a general behavior for the case of the cavities with different aspect ratios. Xin and Le Quéré [8] focused on chaotic flow in the differentially heated cavity of aspect ratio 4. They showed that the temporal behavior of the flow at Ra up to 10^{10} was chaotic, and the flow structure was anisotropic, but laminar regimes were still visible. Ishida *et al.* [42] computed the first and second largest Lyapunov exponents for air convection in a rectangular cavity, which they used as a criterion to identify the periodic, quasi-periodic, and chaotic regimes of the flow. The Feigenbaum scenario was reported to exist in the case of a vibrational square cavity heated from the sides [43], where a Pomeau-Manneville type-I intermittency is subsequently observed. Bratsun *et al.* [44] carried out extensive experimental and numerical studies of the successive bifurcations of the flow at $Pr = 26$. At this high Prandtl number, the primary instability consists of traveling waves. In their two dimensional simulations, they successively observed periodicity, two-frequency quasi-periodicity (2D torus), three-frequency quasi-periodicity (3D torus), and finally chaos (destruction of higher dimensional torus). In their three dimensional simulation and experiments, they established the route to chaos as fol-

lows: a Hopf bifurcation leading to a periodic flow, then a pitchfork bifurcation leading to a 3D periodic flow. Later on, a secondary Hopf bifurcation gives the birth of quasi-periodicity (torus), and finally chaos occurs due to the corrugation of the torus. No equivalent study has been performed for air as far as we know. We plan to determine this in the thesis.

1.2.9 Turbulent regime

At still higher Rayleigh numbers, the turbulent regime has been well documented. Phillips [45] compared 3D direct numerical simulation results with the experiments of Elder [46] and showed that most of the turbulence was generated by the shear layer at the center of the slot. Versteegh and Niewstadt [47, 48] computed energy budgets to determine scaling laws and wall functions with a direct application to turbulence modeling. Although the presence of spiral structures has been noted by Wang *et al.*, [49] for air at $Ra = 5.4 \times 10^5$, a complete coherent-structure-based description is still missing. As noted by Hall [50], "there has been apparently no attempt to look for coherent structures embedded in the flows as has become routine in shear flows". Few models for the dynamics of such structures have yet been proposed [50].

Some DNS studies [47] suggest that a substantial part of the energy in the turbulent regime is associated with patterns which are similar to the most linearly unstable mode. This situation presents some analogy with Rayleigh-Bénard convection, where the large-scale structures identified in the turbulent regime share common features with the convection cells observed at near-critical Rayleigh numbers [3, 51, 52]. In addition, determining key instability mechanisms in a canonical configuration will be useful for studying more complex geometries and/or including additional physics such as radiation or mixed convection.

1.3 Objectives and outline of thesis

The goal of the present study is to provide a description of the transition to chaos of natural convection of air between two infinite plates, and to determine the role of transverse effects in this transition. Our study is based on direct numerical simulations. Unlike the linear or weakly linear stability analysis that are only valid in the neighbourhood of the critical Rayleigh

number, DNS allows us to follow the branches of possible solutions and to determine the nature of bifurcations at Rayleigh numbers far beyond Ra_c. Results from numerical simulations depend on the periodic dimensions of the plates. If the periodic vertical (transverse) dimension is not large enough, this may hamper the development of the vertical (transverse) instabilities in this direction. Nevertheless we believe that they may constitute a necessary step towards a better understanding of the dynamics of unsteady natural convection. Determing the basic instability patterns at moderate Rayleigh numbers could help us understand the flow in the fully turbulent regime [33, 47, 52, 49]. Our goal is to determine the influence of 3D effects in various configurations of small and large extent.

The thesis is organized as follows. The numerical method is presented in Chapter 2. Chapter 3 is devoted to the 2D analysis and 2D simulations. We firstly recall standard theoretical results based on linear and weakly nonlinear stability analysis of the flow between two differentially heated vertical plates. We derive analytically a Ginzburg-Landau equation to represent the flow around the first bifurcation. Then we briefly present results for 2D direct numerical simulation for Rayleigh numbers Ra up to about $3Ra_c$. We show that a chaotic regime can only be found over a limited range of Rayleigh numbers. In Chapter 4, we present the results of 3D numerical simulations for the configuration $A_y = 1$ and $A_z = 10$, a confined domain in the transverse direction. The sequence of the instabilities leading to chaos and corresponding physics are described in detail. A specific 3D structure is identified. In Chapter 5, we study the dynamics of one of these structures in a limited domain $A_y = 1$ and $A_z = 2.5$, which constitutes a minimal flow unit (MFU). In Chapter 6, we consider larger domains. The Arnoldi method is used to investigate the stability of the 2D rolls from which we determine the most unstable transverse wavenumbers. The predictions of linear stability analysis are confronted with 3D nonlinear simulations. A general conclusion is given in Chapter 7.

Chapter 2

Numerical methods

2.1 Introduction

In this chapter, we present the numerical methods used in the DNS codes. We firstly present the 2D code [23], which is a mixed Galerkin-collocation code and is based on the Uzawa algorithm. Then we present the 3D code [53], which is a collocation code using a pressure correction algorithm. The 3D code is implemented in a parallel architecture.

2.2 Numerical methods for 2D simulation

The 2D Navier-Stokes equation within the Boussinesq approximation reads as:

$$\begin{aligned}
&\frac{\partial u}{\partial x}+\frac{\partial w}{\partial z}=0\\
&\frac{\partial u}{\partial t}+u\frac{\partial u}{\partial x}+w\frac{\partial u}{\partial z}=-\frac{\partial p}{\partial x}+\frac{Pr}{\sqrt{Ra}}(\frac{\partial^2 u}{\partial x^2}+\frac{\partial^2 u}{\partial z^2})\\
&\frac{\partial w}{\partial t}+u\frac{\partial w}{\partial x}+w\frac{\partial w}{\partial z}=-\frac{\partial p}{\partial z}+\frac{Pr}{\sqrt{Ra}}(\frac{\partial^2 w}{\partial x^2}+\frac{\partial^2 w}{\partial z^2})+Pr\theta\\
&\frac{\partial \theta}{\partial t}+u\frac{\partial \theta}{\partial x}+w\frac{\partial \theta}{\partial z}=\frac{1}{\sqrt{Ra}}(\frac{\partial^2 \theta}{\partial x^2}+\frac{\partial^2 \theta}{\partial z^2})
\end{aligned} \tag{2.1}$$

with Dirichlet boundary conditions at the plates

$$u(0,y,z,t)=u(1,y,z,t)=0,\quad w(0,y,z,t)=w(1,y,z,t)=0, \tag{2.2}$$

$$\theta(0,y,z,t)=0.5,\quad \theta(1,y,z,t)=-0.5 \tag{2.3}$$

and periodic conditions in z-direction. Here (u, w) are the horizontal and vertical velocities in the 2D plane (x,z).

This code uses the spectral Galerkin-collocation method for the spatial discretization. A second-order mixed explicit-implicit scheme is used for the temporal discretization. The complete Navier-Stokes system is solved by inverting the Uzawa operator to ensure incompressibility. The numerical algorithms are detailed as follows.

2.2.1 Spatial discretization

The code relies on a Chebyshev collocation discretization in the horizontal direction x and a Fourier discretization in the vertical direction z. The differentiation in the horizontal direction x is performed in the physical space by multiplying the variables with the differentiation matrix D_x, while the differentiation in the vertical direction z is performed in the Fourier space, which is simply a mulplication of the variables with ik, where k is the wavenumber of a given mode.

2.2.2 Temporal discretization

The dimensionless system of advection-diffusion equations can be written in a compact form as:

$$\frac{\partial f}{\partial t} + \mathbf{V}\nabla f = \nabla^2 f \tag{2.4}$$

where f represents u, v, w, or θ. For the temporal discretization, the diffusive term is treated implicitly, while the convective term is treated explicitly. A second order discretization is used for the time-derivative, so we get

$$\frac{3f^{n+1} - 4f^n + f^{n-1}}{2\Delta t} + 2(\mathbf{V}\nabla f)^n - (\mathbf{V}\nabla f)^{n-1} = \nabla^2 f^{n+1} \tag{2.5}$$

This scheme can be recast into the general form of a Helmholtz equation for the unknown f^{n+1} as:

$$\nabla^2 f^{n+1} - \lambda f^{n+1} = S_f \tag{2.6}$$

where $\lambda = \frac{3}{2\Delta t}$ and $S_f = \frac{-4f^n + f^{n-1}}{2\Delta t} + 2(\mathbf{V}\nabla f)^n - (\mathbf{V}\nabla f)^{n-1}$. Applying this discretization strategy to the Navier-Stokes equations system Eq (2.1), we obtain the numerical schemes as following:

$$\frac{\partial u^{n+1}}{\partial x} + \frac{\partial w^{n+1}}{\partial z} = 0 \tag{2.7}$$

$$\frac{Pr}{\sqrt{Ra}}\nabla^2 u^{n+1} - \frac{3}{2\Delta t}u^{n+1} = \frac{\partial p^{n+1}}{\partial x} - \frac{4u^n - u^{n-1}}{2\Delta t} + 2(\mathbf{V}\nabla u)^n - (\mathbf{V}\nabla u)^{n-1} \tag{2.8}$$

$$\frac{Pr}{\sqrt{Ra}}\nabla^2 w^{n+1} - \frac{3}{2\Delta t}w^{n+1} = \frac{\partial p^{n+1}}{\partial z} - \frac{4w^n - w^{n-1}}{2\Delta t} + 2(\mathbf{V}\nabla w)^n - (\mathbf{V}\nabla w)^{n-1} + Pr\theta^{n+1} \tag{2.9}$$

$$\frac{1}{\sqrt{Ra}}\nabla^2 \theta^{n+1} - \frac{3}{2\Delta t}\theta^{n+1} = -\frac{4\theta^n - \theta^{n-1}}{2\Delta t} + 2(\mathbf{V}\nabla\theta)^n - (\mathbf{V}\nabla\theta)^{n-1} \tag{2.10}$$

This is a Stokes problem, which consists of three general Helmholtz equations and an equation of incompressibility for the fluid.

2.2.3 The Uzawa operator

The Uzawa algorithm [54] is based on elimination of the velocity in the time-dependent Stokes problem. Let $\mathbf{HU}$, $\mathbf{HW}$, $\mathbf{H\Theta}$ be the Helmholtz operators for u, w, θ respectively. Dropping the time discretization index, we can write the Stokes problem as:

$$\mathbf{HU}u = \frac{\partial p}{\partial x} - Su \tag{2.11}$$

$$\mathbf{HW}w = \frac{\partial p}{\partial z} - Sw + Pr\theta \tag{2.12}$$

$$\mathbf{H\Theta}\theta = -S\theta \tag{2.13}$$

$$\frac{\partial u}{\partial x} + \frac{\partial w}{\partial z} = 0 \tag{2.14}$$

along with some boundary conditions for u, w and θ. Formal inversion of (2.11) and (2.12) yields

$$u^{n+1} = \mathbf{HU}^{-1}\frac{\partial p}{\partial x} - \mathbf{HU}^{-1}Su \tag{2.15}$$

$$w^{n+1} = \mathbf{HW}^{-1}\frac{\partial p}{\partial z} - \mathbf{HW}^{-1}Sw + \mathbf{HW}^{-1}Pr\theta \tag{2.16}$$

Enforcing the incompressibility leads to an equation for the pressure which can be written as

$$\left(\frac{\partial}{\partial x}\mathbf{H}\mathbf{U}^{-1}\frac{\partial}{\partial x}+\frac{\partial}{\partial z}\mathbf{H}\mathbf{W}^{-1}\frac{\partial}{\partial z}\right)p=\frac{\partial}{\partial x}\mathbf{H}\mathbf{U}^{-1}Su+\frac{\partial}{\partial z}\mathbf{H}\mathbf{W}^{-1}Sw-\frac{\partial}{\partial z}\mathbf{H}\mathbf{W}^{-1}Pr\theta \tag{2.17}$$

By inverting the operator $(\frac{\partial}{\partial x}\mathbf{H}\mathbf{U}^{-1}\frac{\partial}{\partial x}+\frac{\partial}{\partial z}\mathbf{H}\mathbf{W}^{-1}\frac{\partial}{\partial z})$, we can obtain the pressure. Then computing the pressure gradient and solving the two Helmholtz equations (2.11)- (2.13) leads to the solution u^{n+1} and w^{n+1}.

2.3 Numerical methods for 3D simulation

The Navier-Stokes equations are rewritten as follows:

$$\begin{aligned}
&\frac{\partial u}{\partial x}+\frac{\partial v}{\partial y}+\frac{\partial w}{\partial z}=0\\
&\frac{\partial u}{\partial t}+u\frac{\partial u}{\partial x}+v\frac{\partial u}{\partial y}+w\frac{\partial u}{\partial z}=-\frac{\partial p}{\partial x}+\frac{Pr}{\sqrt{Ra}}(\frac{\partial^2 u}{\partial x^2}+\frac{\partial^2 u}{\partial y^2}+\frac{\partial^2 u}{\partial z^2})\\
&\frac{\partial v}{\partial t}+u\frac{\partial v}{\partial x}+v\frac{\partial v}{\partial y}+w\frac{\partial v}{\partial z}=-\frac{\partial p}{\partial y}+\frac{Pr}{\sqrt{Ra}}(\frac{\partial^2 v}{\partial x^2}+\frac{\partial^2 v}{\partial y^2}+\frac{\partial^2 v}{\partial z^2})\\
&\frac{\partial w}{\partial t}+u\frac{\partial w}{\partial x}+v\frac{\partial w}{\partial y}+w\frac{\partial w}{\partial z}=-\frac{\partial p}{\partial z}+\frac{Pr}{\sqrt{Ra}}(\frac{\partial^2 w}{\partial x^2}+\frac{\partial^2 w}{\partial y^2}+\frac{\partial^2 w}{\partial z^2})+Pr\theta\\
&\frac{\partial \theta}{\partial t}+u\frac{\partial \theta}{\partial x}+v\frac{\partial \theta}{\partial y}+w\frac{\partial \theta}{\partial z}=\frac{1}{\sqrt{Ra}}(\frac{\partial^2 \theta}{\partial x^2}+\frac{\partial^2 \theta}{\partial y^2}+\frac{\partial^2 \theta}{\partial z^2})
\end{aligned} \tag{2.18}$$

with Dirichlet boundary conditions at the plates

$$\begin{aligned}
&u(0,y,z,t)=u(1,y,z,t)=0,\quad v(0,y,z,t)=v(1,y,z,t)=0,\\
&w(0,y,z,t)=w(1,y,z,t)=0,\\
&\tilde{\theta}(0,y,z,t)=0.5,\quad \tilde{\theta}(1,y,z,t)=-0.5
\end{aligned} \tag{2.19}$$

and periodic conditions in y and z directions.

This code uses a spectral collocation method for the spatial discretization. The equations are integrated in time with a second-order mixed explicit-implicit scheme. Incompressibility is enforced by the projection-correction method. The domain decomposition is carried out by the

Schur complement and implemented with the MPI library.

2.3.1 Temporal discretization

Applying the same scheme used in the 2D code to the 3D Navier-Stokes equation system (2.18), we obtain the numerical scheme as follows:

$$\frac{\partial u^{n+1}}{\partial x} + \frac{\partial v^{n+1}}{\partial y} + \frac{\partial w^{n+1}}{\partial z} = 0 \tag{2.20}$$

$$\frac{Pr}{\sqrt{Ra}}\nabla^2 u^{n+1} - \frac{3}{2\Delta t}u^{n+1} = \frac{\partial p^{n+1}}{\partial x} - \frac{4u^n - u^{n-1}}{2\Delta t} + 2(\mathbf{V}\nabla u)^n - (\mathbf{V}\nabla u)^{n-1} \tag{2.21}$$

$$\frac{Pr}{\sqrt{Ra}}\nabla^2 v^{n+1} - \frac{3}{2\Delta t}v^{n+1} = \frac{\partial p^{n+1}}{\partial y} - \frac{4v^n - v^{n-1}}{2\Delta t} + 2(\mathbf{V}\nabla v)^n - (\mathbf{V}\nabla v)^{n-1} \tag{2.22}$$

$$\frac{Pr}{\sqrt{Ra}}\nabla^2 w^{n+1} - \frac{3}{2\Delta t}w^{n+1} = \frac{\partial p^{n+1}}{\partial z} - \frac{4w^n - w^{n-1}}{2\Delta t} + 2(\mathbf{V}\nabla w)^n - (\mathbf{V}\nabla w)^{n-1} + Pr\theta^{n+1} \tag{2.23}$$

$$\frac{1}{\sqrt{Ra}}\nabla^2 \theta^{n+1} - \frac{3}{2\Delta t}\theta^{n+1} = -\frac{4\theta^n - \theta^{n-1}}{2\Delta t} + 2(\mathbf{V}\nabla\theta)^n - (\mathbf{V}\nabla\theta)^{n-1} \tag{2.24}$$

2.3.2 Spatial discretization

The spatial discretization is based on a spectral collocation method as shown in Figure 2.1. In the horizontal direction x, Chebyshev modes are used, where the unkowns are defined on the Gauss-Lobatto points $x = \cos\frac{i\pi}{N}$, $0 \le i \le N$. In the transverse direction y, Fourier modes are used, as the periodic condition is imposed as the boundary condition in this direction. Thus, the mesh in this direction is homogeneous. In the vertical direction z, the simulation domain is decomposed into 4 to 16 subdomains. Although a periodic boundary condition is imposed in z for the full domain, Chebyshev modes are used for each subdomain in this direction. The periodicity in this direction is ensured by the periodic communicator implemented with the MPI library.

In practice, all the discrete variables are stored in a matrix. Matrices for the spatial differentiation are constructed, named D_x, D_y, D_z, etc. Thus, the spatial differentiation can be simply done by multiplying the original matrix of the variable by the differentiation matrix. For the second differentiation, the multiplication is performed twice.

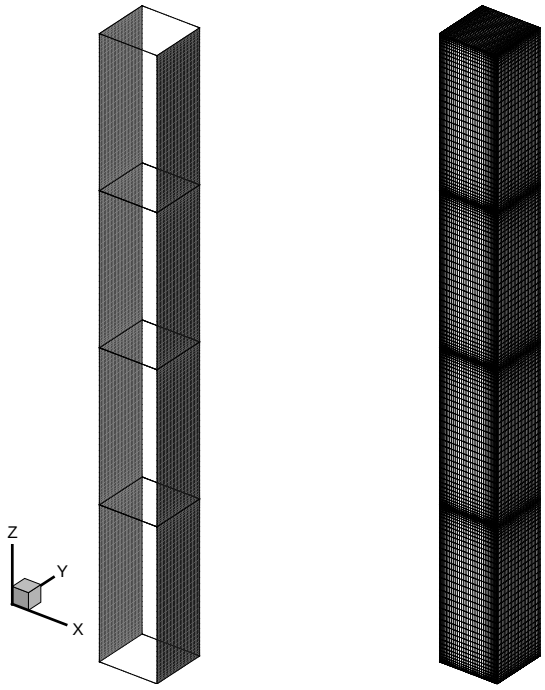

(a) (b)

Figure 2.1: (a) Decomposition of subdomains, (b) Mesh, $A_y = 1$, $A_z = 10$.

2.3.3 Solution of the general Helmholtz problem

The general 3D Helmholtz problem reads as

$$(\nabla^2 - \lambda) f = S \tag{2.25}$$

where $\nabla^2 = \frac{\partial^2}{\partial x^2} + \frac{\partial^2}{\partial y^2} + \frac{\partial^2}{\partial z^2}$ and S represents the source term. The idea to solve this equation in the discrete form is to invert the operator $(\nabla^2 - \lambda)$. In our code, the matrix-diagonalisation method is employed [55, 56]. In fact, the second derivative, for example $\frac{\partial^2}{\partial x^2}$, in the discrete form constitutes a regular matrix, which is diagonalisable and invertible, so we have $D_x^2 = P\Lambda_x P^{-1}$, $D_y^2 = Q\Lambda_y Q^{-1}$, $D_z^2 = R\Lambda_z R^{-1}$, where Λ_x, Λ_y, Λ_z are diagonal matrices containing the eigenvalues of D_x^2, D_y^2, D_z^2, respectively, and the matrices P, Q, R are formed by the eigenvectors of D_x^2, D_y^2, D_z^2, respectively. In the discrete form, the 3D Helmholtz equation takes

the following form:

$$(\mathbf{I}_z \otimes \mathbf{I}_y \otimes D_x^2 + \mathbf{I}_z \otimes D_y^2 \otimes \mathbf{I}_x + D_z^2 \otimes \mathbf{I}_y \otimes \mathbf{I}_x - \mathbf{I}_z \otimes \mathbf{I}_y \otimes \mathbf{I}_x \lambda)F = S \tag{2.26}$$

where $\otimes$ is the Kronecker product operator. Multiplying Eq (2.26) by $(P^{-1} \otimes Q^{-1} \otimes R^{-1})$, we can write this equation into the eigenspace in the following way. For the first term on the left side of Eq (2.26), we have

$$\begin{aligned}
&(R^{-1} \otimes Q^{-1} \otimes P^{-1})(\mathbf{I}_z \otimes \mathbf{I}_y \otimes D_x^2) \\
&= (R^{-1} \otimes Q^{-1} \otimes P^{-1})(\mathbf{I}_z \otimes \mathbf{I}_y \otimes P\Lambda_x P^{-1}) \\
&= (R^{-1} \otimes Q^{-1})(\mathbf{I}_z \otimes \mathbf{I}_y) \otimes (P^{-1} P \Lambda_x P^{-1}) \\
&= (R^{-1} \otimes Q^{-1})(\mathbf{I}_z \otimes \mathbf{I}_y) \otimes (\Lambda_x P^{-1}) \\
&= (\mathbf{I}_z \otimes \mathbf{I}_y \otimes \Lambda_x)(R^{-1} \otimes Q^{-1} \otimes P^{-1})
\end{aligned}$$

by using twice the property $(A \otimes B)(C \otimes D) = AC \otimes BD$. With similar treatment for the other terms, we can obtain

$$(\mathbf{I}_z \otimes \mathbf{I}_y \otimes \Lambda_x + \mathbf{I}_z \otimes \Lambda_y \otimes \mathbf{I}_x + \Lambda_z \otimes \mathbf{I}_y \otimes \mathbf{I}_x - \mathbf{I}_z \otimes \mathbf{I}_y \otimes \mathbf{I}_x \lambda)\tilde{F} = \tilde{S} \tag{2.27}$$

or

$$A\tilde{F} = \tilde{S}$$

where $\tilde{F} = (R^{-1} \otimes Q^{-1} \otimes P^{-1})F$, $\tilde{S} = (R^{-1} \otimes Q^{-1} \otimes P^{-1})S$ and $A = \mathbf{I}_z \otimes \mathbf{I}_y \otimes \Lambda_x + \mathbf{I}_z \otimes \Lambda_y \otimes \mathbf{I}_x + \Lambda_z \otimes \mathbf{I}_y \otimes \mathbf{I}_x - \mathbf{I}_z \otimes \mathbf{I}_y \otimes \mathbf{I}_x \lambda$. Therefore, to solve the 3D Helmholtz problem, we firstly multiply the source term S by $(R^{-1} \otimes Q^{-1} \otimes P^{-1})$, then invert the operator A to obtain $\tilde{F}$. Finally, multiplying $\tilde{F}$ by $P \otimes Q \otimes R$, we get the solution F.

2.3.4 Prediction-correction method

Solution of the incompressible Navier-Stokes equations requires the solution of Helmholtz equation (2.25), together with an appropriate treatment of the pressure term, so that the condition

of zero velocity divergence can be satisfied. Several methods exist for this treatment. The projection-correction method is implemented in the 3D DNS code which we use in this thesis.

Prediction

In the code, the time-stepping starts with the resolution of the transport equation of temperature (2.24). By using variables obtained at the time-steps n and $n-1$, the Helmholtz equation (2.24) can be solved as described in the last subsection (2.3.3), so θ^{n+1} is obtained. Then, we ignore the equation of mass conservation (2.20), and suppose the pressure p^n obtained at the previous step as the pressure at the present step p^*, and inject it into the equations (2.21)- (2.23), so we get three Helmholtz equations:

$$(\nabla^2 - \lambda)u^* = S_u + a\frac{\partial p^*}{\partial x} \tag{2.28}$$

$$(\nabla^2 - \lambda)v^* = S_v + a\frac{\partial p^*}{\partial y} \tag{2.29}$$

$$(\nabla^2 - \lambda)w^* = S_w + a\frac{\partial p^*}{\partial z} + Pr\theta^{n+1} \tag{2.30}$$

where S_f represents the source term $S_f = \frac{\sqrt{Ra}}{Pr}(\frac{-4f^n+f^{n-1}}{2\Delta t} + 2(\mathbf{V}\nabla f)^n - (\mathbf{V}\nabla f)^{n-1})$, $a = \frac{\sqrt{Ra}}{Pr}$, and $\lambda = \frac{3\sqrt{Ra}}{2Pr\Delta t}$. By solving these three equations (2.28)- (2.30), we obtain the velocity field u^*,v^*,w^*.

Correction

Incompressibility i.e. equation (2.20) is enforced by adjusting the pressure term. Equations (2.21)- (2.23) and (2.28)- (2.30) lead to the following equations:

$$(\nabla^2 - \lambda)(u^{n+1} - u^*) = a\frac{\partial(p^{n+1} - p^*)}{\partial x} \tag{2.31}$$

$$(\nabla^2 - \lambda)(v^{n+1} - v^*) = a\frac{\partial(p^{n+1} - p^*)}{\partial y} \tag{2.32}$$

$$(\nabla^2 - \lambda)(w^{n+1} - w^*) = a\frac{\partial(p^{n+1} - p^*)}{\partial z} \tag{2.33}$$

which can be recast into the form

$$(\nabla^2 - \lambda)(\mathbf{V}^{n+1} - \mathbf{V}^*) = a\nabla(p^{n+1} - p^*) \tag{2.34}$$

Applying the divergence on both sides of (2.34), and using $\nabla \cdot \mathbf{V}^{n+1} = 0$ leads to

$$-(\nabla^2 - \lambda)\nabla V^* = a\nabla^2(p^{n+1} - p^*) \tag{2.35}$$

Suppose that there exists a potential ϕ satisfying

$$\nabla \cdot \mathbf{V}^* = \nabla^2\phi \tag{2.36}$$

we can obtain the scalar ϕ by solving the Poisson equation (2.36). Substituting (2.36) into equation (2.35), we obtain

$$p^{n+1} = p^* + \frac{\lambda}{a}\phi - \frac{1}{a}\nabla^2\phi \tag{2.37}$$

Since $\frac{\lambda}{a} = \frac{3}{2\Delta t}$ and $a \sim \sqrt{Ra}$, $-\frac{1}{a}\nabla^2\phi$ is negligible compared to the other terms in (2.37), thus in practice the pressure is corrected as

$$p^{n+1} = p^* + \frac{\lambda}{a}\phi \tag{2.38}$$

Introduction of (2.38) into (2.34) leads to

$$V^{n+1} = V^* - \nabla\phi + \frac{1}{\lambda}\nabla^2(V^{n+1} - V^*) \tag{2.39}$$

where the last term on the right side is $\sqrt{Ra}$ times smaller than the other terms, since $\lambda \sim \sqrt{Ra}$, thus in practice the velocity can be simply updated as

$$V^{n+1} = V^* - \nabla\phi \tag{2.40}$$

2.3.5 Schur complement

As presented above, the Navier-Stokes equations can be recast into several Helmholtz problems. The idea of domain decomposition is to divide the simulation domain into several subdomains. The simulation of each subdomain is carried out on individual processors. Since these problems are second-order problems, uniqueness of the solution over the whole domain is guaranteed through imposing the continuity of the variables and their derivatives across the interfaces. The jump condition at the interface $[[\frac{\partial f}{\partial z}]] = 0$ is enforced through an influence matrix technique [53]. The Helmholtz problems are discretized and turned into a linear system $\mathbf{K}f = \mathbf{S}$. The matrix K associated with the spectral discretization is very large and dense and difficult to invert. By means of domain decomposition, the dense matrix $\mathbf{K}$ can be turned into a matrix with several dense blocks as in Eq (2.41).

Here we suppose the domain is divided into three subdomains, so the matrix $\mathbf{K}$ contains three dense blocks $\mathbf{A_{nn}}$, (n is the system dimension) which can be solved on three different processors. On each processor, we solve a Helmholtz problem with Dirichlet boundary conditions. However, in order to ensure that the variables are continuous across the interface, we can set the elements at the two interfaces in matrix $\mathbf{K}$ equal to 1. In this way, we obtain the matrix $\mathbf{K}$ in Eq (2.41), but the derivative $\frac{\partial f}{\partial z}$ is not continuous across the interface.

The idea for the construction of a Schur complement is to find a linear relation between f and $\frac{\partial f}{\partial z}$ at the interface. For the first interface, we set $\tilde{S}$ the unit vector to be $\tilde{S}_1 = (0, ..., 0, 1, 0, ..., 0, 0, 0, ..., 0)^T$ as in Eq (2.41), and solve the system $\mathbf{K}f_1 = \tilde{S}_1$ to obtain a solution f_1. Then we can calculate its derivative $\frac{\partial f_1}{\partial z}$ and the corresponding jump at the interface, which constitutes the first column of the Schur matrix M. For the second interface, we set $\tilde{S}$ to be $\tilde{S}_2 = (0, ..., 0, 0, 0, ..., 0, 1, 0, ..., 0)^T$ as in Eq (2.41), and solve $\mathbf{K}f_2 = \tilde{S}_2$ to obtain f_2. Then we calculate its derivative $\frac{\partial f_2}{\partial z}$ and the corresponding jump at the interface, which corresponds to the second column of the Schur matrix M. By repeating this procedure, we build the Schur

matrix M.

$$K = \begin{bmatrix} & & & 0 & & & & 0 & & & \\ & \mathbf{A_{nn}} & & \vdots & & & & \vdots & & & \\ & & & 0 & & & & 0 & & & \\ 0 & \cdots & 0 & \mathbf{1} & 0 & \cdots & 0 & 0 & 0 & \cdots & 0 \\ & & & 0 & & & & 0 & & & \\ & & & \vdots & & \mathbf{A_{nn}} & & \vdots & & & \\ & & & 0 & & & & 0 & & & \\ 0 & \cdots & 0 & 0 & 0 & \cdots & 0 & \mathbf{1} & 0 & \cdots & 0 \\ & & & 0 & & & & 0 & & & \\ & & & \vdots & & & & \vdots & & \mathbf{A_{nn}} & \\ & & & 0 & & & & 0 & & & \end{bmatrix}; \quad \tilde{S}_1 = \begin{bmatrix} 0 \\ \vdots \\ 0 \\ \mathbf{1} \\ 0 \\ \vdots \\ 0 \\ 0 \\ 0 \\ \vdots \\ 0 \end{bmatrix} \quad \tilde{S}_2 = \begin{bmatrix} 0 \\ \vdots \\ 0 \\ 0 \\ 0 \\ \vdots \\ 0 \\ \mathbf{1} \\ 0 \\ \vdots \\ 0 \end{bmatrix} \tag{2.41}$$

For the whole system $\mathbf{K}f = S$, we first give some arbitrary values V_{arbi1}, V_{arbi2} to the elements of S at the interfaces, as $(S_{bc1}, ..., V_{arbi1}, ..., V_{arbi2}, ..., S_{bc2})$, where S_{bc1} and S_{bc2} are the boundary conditions of whole system. By solving the system $\mathbf{K}f = S$, we obtain a solution $\tilde{f}$, and then calculate the jumps of its derivative $\frac{\partial \tilde{f}}{\partial z}$ at the interfaces. As the values at the interfaces were given arbitrarily, we must a correction to S so that $\frac{\partial f}{\partial z}$ is continuous at the interfaces. By using the Schur matrix M constructed above, this can be simply achieved via

$$S_{interface} = V_{arbi} - M^{-1}\frac{\partial \tilde{f}}{\partial z} \tag{2.42}$$

where $S_{interface}$ is a vector containing the elements of S at the interfaces. With these new values of S at the interfaces, we can solve the system $\mathbf{K}f = S$, where $S = (S_{bc1}, \cdots, S_{interface1}, \cdots, S_{interface2}, \cdots, S_{bc2})$. We obtain f and its derivative $\frac{\partial f}{\partial z}$, which are now continuous across the interfaces.

This algorithm was implemented with the MPI library [53]. For the step of Schur matrix construction, the derivatives $\frac{\partial f_1}{\partial z}$ and $\frac{\partial f_2}{\partial z}$ at the interfaces are independently calculated on each

processor. Then a SENDRECV command is used on each processor to gether the derivative values at the interfaces on the neighbour subdomains. Once these data exchanged, the jumps of the derivatives are calculated on each processor, which constitutes the columns of the Schur matrix. Solution of the Helmholtz equation at the interfaces are performed in the similar way. The derivatives $\frac{\partial \tilde{f}}{\partial z}$ given by the arbitrary interfaces values are calculated independently on each processor. Then a SENDRECV command is also used to gether the neighbourhood values, so as to obtain the jumps values of the first derivatives at the interfaces. With the Schur matrix M already obtained (the columns of which are dispatched on different processors), the correction step is performed parallelly. Finally a SENDRECV command is called to redistribute the correction values to each subdomain. Once f and $\frac{\partial f}{\partial z}$ are continueous across the interfaces, the Helmholtz equation is solved independently for each subdomain.

Chapter 3

2D Channel

3.1 Introduction

In this chapter, we carry out our study in the two-dimensional (2D) framework. We first apply linear stability analysis, and determine the critical Rayleigh number Ra_c and the critical wavenumber k_c for the onset of the first instability. Then the weakly nonlinear analysis is used to derive the Ginzburg-Landau equation, which predicts the perturbation amplitude of first instability in the neighbourhood of the critical Rayleigh number, and predicts the nature (absolute or convective) of the first instability. We then shortly present results of the nonlinear simulations in 2D.

3.2 Base flow

The equations of motion (1.1)- (1.4) admit an analytic steady solution (U, V, W, Θ), the pure conduction state, which depends only on the x direction:

$$\begin{aligned} &U = 0; \qquad V = 0; \\ &W(x) = \frac{1}{6}\sqrt{Ra}\left[(x-\frac{1}{2})^3 - \frac{1}{4}\left(x-\frac{1}{2}\right)\right]; \qquad \Theta(x) = -\left(x-\frac{1}{2}\right) \end{aligned} \tag{3.1}$$

The solution Eq. (3.1) is represented in Figure 3.1. The equations (1.1)- (1.4) admit an $O(2) \times O(2)$ symmetry. One $O(2)$ symmetry corresponds to the translations in the transverse direction y and the reflection $y \to -y$, while the other corresponds to the translations in the vertical direction z and a reflection that combines centrosymmetry and Boussinesq symmetry: $(x, z, T) \to (1-x, -z, -T)$, where T represents the variable U, V, W, or Θ. The base flow

possesses the same symmetry as the equations, since it is one-dimensional and antisymmetric with respect to the mid-plane $x = 0.5$.

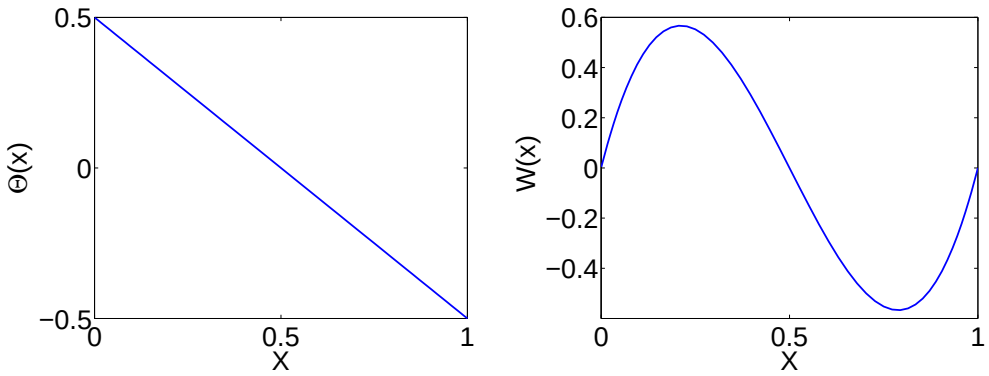

(a) (c)

Figure 3.1: Base flow profiles for (a) temperature $\Theta(x)$ and (b) vertical velocity $W(x)$.

3.3 Linear stability analysis

The base flow Eq. (3.1) is parallel and depends only on the x-direction. The hypotheses of Squire's theorem are verified in this case, so that the most unstable mode is expected to be 2D. Therefore, the 2D approach is adopted for the linear stability analysis as Bergholz [14]. The 2D Navier-Stokes equations read as Eq. (2.1) associated with boundary conditions Eq. (2.2)- (2.3).

We decompose the velocity and temperature into the base flow (U, W, Θ) and perturbations (u, w, θ) as

$$u = U + u' \qquad w = W + w' \qquad \theta = \Theta + \theta' \tag{3.2}$$

Subtracting the equations of base flow, we obtain the equations of perturbations (dropping the

' symbol):

$$\frac{\partial u}{\partial x}+\frac{\partial w}{\partial z}=0 \tag{3.3}$$

$$\frac{\partial u}{\partial t}+u\frac{\partial u}{\partial x}+w\frac{\partial u}{\partial z}+W\frac{\partial u}{\partial z}=-\frac{\partial p}{\partial x}+\frac{Pr}{\sqrt{Ra}}(\frac{\partial^2 u}{\partial^2 x}+\frac{\partial^2 u}{\partial^2 z}) \tag{3.4}$$

$$\frac{\partial w}{\partial t}+u\frac{\partial w}{\partial x}+u\frac{\partial W}{\partial x}+w\frac{\partial w}{\partial z}+W\frac{\partial w}{\partial z}=-\frac{\partial p}{\partial z}+\frac{Pr}{\sqrt{Ra}}(\frac{\partial^2 w}{\partial^2 x}+\frac{\partial^2 w}{\partial^2 z})+Pr\theta \tag{3.5}$$

$$\frac{\partial \theta}{\partial t}+u\frac{\partial \theta}{\partial x}+u\frac{\partial \Theta}{\partial x}+w\frac{\partial \theta}{\partial z}+W\frac{\partial \theta}{\partial z}=\frac{1}{\sqrt{Ra}}(\frac{\partial^2 \theta}{\partial^2 x}+\frac{\partial^2 \theta}{\partial^2 z}) \tag{3.6}$$

Let ψ be the stream function for the perturbations, where $u=-\frac{\partial \psi}{\partial z}$, $w=\frac{\partial \psi}{\partial x}$. We first multiply the operator $\frac{\partial}{\partial z}$ to Eq. (3.4) and $\frac{\partial}{\partial z}$ to Eq. (3.5), respectively, and substracted them from each other by using $\nabla\times\nabla p=0$ to eliminate the pressure terms, we then obtain the perturbation equations as a function of (ψ,θ):

$$\left(\frac{\partial}{\partial t}-\frac{\partial \psi}{\partial z}\frac{\partial}{\partial x}+\frac{\partial \psi}{\partial x}\frac{\partial}{\partial z}\right)\nabla^2\psi=\left(\frac{Pr}{\sqrt{Ra}}\nabla^4-W\frac{\partial}{\partial z}\nabla^2+\frac{\partial^2 W}{\partial x^2}\frac{\partial}{\partial z}\right)\psi+Pr\frac{\partial \theta}{\partial x} \tag{3.7}$$

$$\left(\frac{\partial}{\partial t}-\frac{\partial \psi}{\partial z}\frac{\partial}{\partial x}+\frac{\partial \psi}{\partial x}\frac{\partial}{\partial z}\right)\theta=\frac{\partial \Theta}{\partial x}\frac{\partial \psi}{\partial z}+\left(\frac{1}{\sqrt{Ra}}\nabla^2-W\frac{\partial}{\partial z}\right)\theta \tag{3.8}$$

This can be rewritten as

$$M\frac{\partial \phi}{\partial t}=L\phi+b(\phi,\phi) \tag{3.9}$$

with

$$\phi=\begin{bmatrix}\psi\\ \theta\end{bmatrix};\quad b=\begin{bmatrix}b_\psi\\ b_\theta\end{bmatrix};\quad M=\begin{bmatrix}\nabla^2 & 0\\ 0 & 1\end{bmatrix};$$
$$L=\begin{bmatrix}\frac{Pr}{\sqrt{Ra}}\nabla^4-W\frac{\partial}{\partial z}\nabla^2+\frac{\partial^2 W}{\partial x^2}\frac{\partial}{\partial z} & Pr\frac{\partial}{\partial x}\\ \frac{\partial \Theta}{\partial x}\frac{\partial}{\partial z} & \frac{1}{\sqrt{Ra}}\nabla^2-W\frac{\partial}{\partial z}\end{bmatrix} \tag{3.10}$$

where the nonlinear terms b_ψ and b_θ are bilinear forms and defined as

$$b_\psi(\phi_\alpha, \phi_\beta) = \left(\frac{\partial \psi_\alpha}{\partial z}\frac{\partial}{\partial x} - \frac{\partial \psi_\alpha}{\partial x}\frac{\partial}{\partial z} \right) \nabla^2 \psi_\beta \qquad b_\theta(\phi_\alpha, \phi_\beta) = \left(\frac{\partial \psi_\alpha}{\partial z}\frac{\partial}{\partial x} - \frac{\partial \psi_\alpha}{\partial x}\frac{\partial}{\partial z} \right) \theta_\beta \tag{3.11}$$

The indices α and β will be used to designate the different orders of the solutions obtained in the multiscale analysis in the following subsection 3.4.

The associated boundary conditions are

$$\psi(x=0) = \psi(x=1) = 0 \tag{3.12}$$

$$\psi'(x=0) = \psi'(x=1) = 0 \tag{3.13}$$

$$\theta(x=0) = \theta(x=1) = 0 \tag{3.14}$$

where $'$ denotes differentiation with respect to x.

The linearized system is written as

$$M\frac{\partial \phi}{\partial t} = L\phi \tag{3.15}$$

Seeking a normal-mode solution of the form $\phi = \hat{\phi}(x)e^{st+ikz}$, we obtain a generalized eigenvalue problem $\tilde{\mathcal{L}}\hat{\phi} = s\tilde{\mathcal{M}}\hat{\phi}$. Solving the eigenvalue problem leads to a critical Rayleigh number $Ra_c = 5708$ and a critical wavenumber $k_c = 2.81$, which agrees with the results of Bergholz [14] and Ruth [57]. The critical eigenvalue is purely real, and the modulus of the most unstable mode $|\hat{\phi}(x)|$ at the critical wavenumber k_c and Rayleigh number Ra_c is maximum in the core region, as shown in Figure 3.2.

3.4 Weakly nonlinear analysis

We use a multiscale analysis to derive a Ginzburg-Landau equation for the flow around the first bifurcation.

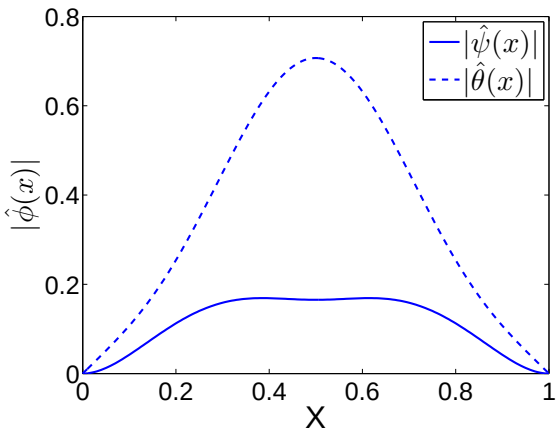

Figure 3.2: Norm of the most unstable mode $|\hat{\phi}(x)|$ ($|\hat{\psi}(x)|$,$|\hat{\theta}(x)|$) at k_c and Ra_c

We introduce the asymptotic expansion of the perturbation to the base flow as

$$\phi = \epsilon\phi_1 + \epsilon^2\phi_2 + \epsilon^3\phi_3 + O(\epsilon^4) \tag{3.16}$$

and choose three time scales $t_0 = t$, $t_1 = \epsilon t$, $t_2 = \epsilon^2 t$ and two spatial scales in z: $z_0 = z$, $z_1 = \epsilon z$. The differential derivation with respect to time is considered as a composed derivation function:

$$\frac{\partial}{\partial t} = \frac{\partial}{\partial t_0} + \epsilon\frac{\partial}{\partial t_1} + \epsilon^2\frac{\partial}{\partial t_2} + O(\epsilon^3) \tag{3.17}$$

Similarly, the spatial derivation with respect to z reads as:

$$\frac{\partial}{\partial z} = \frac{\partial}{\partial z_0} + \epsilon\frac{\partial}{\partial z_1} + O(\epsilon^2) \tag{3.18}$$

The asymptotic analysis is carried out around the threshold of the critical Rayleigh number Ra_c. Thus the Rayleigh number should also be developped as a function of ϵ. By using the Taylor expansion, we obtain two relations which will be used in the development of matrix L with respect to Ra.

$$Ra^{-0.5} = Ra_c^{-0.5} - \frac{1}{2}\epsilon^2 Ra_c^{-1.5} + \frac{3}{8}\epsilon^4 Ra_c^{-2.5} + O(\epsilon^6) \tag{3.19}$$

$$Ra^{0.5} = Ra_c^{0.5} + \frac{1}{2}\epsilon^2 Ra_c^{-0.5} - \frac{1}{4}\epsilon^4 Ra_c^{-1.5} + O(\epsilon^6) \tag{3.20}$$

All the operators in system (3.9) are developped with respect to the new variables

$$M = M_0 + \epsilon M_1 + \epsilon^2 M_2 + \cdots, \tag{3.21}$$

$$L = L_0 + \epsilon L_1 + \epsilon^2 L_2 + \cdots, \tag{3.22}$$

$$b = b_0 + \epsilon b_1 + \epsilon^2 b_2 + \cdots, \tag{3.23}$$

where M_0, M_1, M_2, L_0, L_1, L_2, b_0, b_1 are detailed in the appendix.

The first-order perturbation $\epsilon\phi_1$ can be expressed as

$$\begin{bmatrix} \psi \\ \theta \end{bmatrix} = A(t_1, t_2, z_1) \begin{bmatrix} \hat{\psi}(x) \\ \hat{\theta}(x) \end{bmatrix} e^{st + ik_c z} + C.C. \tag{3.24}$$

where $\hat{\psi}, \hat{\theta}$ are the most unstable modes at the wavenumber k_c given by the linear stability analysis, A is the amplitude of the solution, and $C.C.$ stands for complex conjugate.

Substituting these expansions (3.21)-(3.23) into the original system Eq. (3.9), and collecting the terms at different orders of ϵ, we find the equations:

$$\epsilon : (M_0 \frac{\partial}{\partial t_0} - L_0)\phi_1 = 0 \tag{3.25}$$

$$\epsilon^2 : (M_0 \frac{\partial}{\partial t_0} - L_0)\phi_2 = b_0(\phi_1, \phi_1) + L_1\phi_1 - M_1 \frac{\partial \phi_1}{\partial t_0} - M_0 \frac{\partial \phi_1}{\partial t_1} \tag{3.26}$$

$$\begin{aligned} \epsilon^3 : (M_0 \frac{\partial}{\partial t_0} - L_0)\phi_3 = &-M_0 \frac{\partial \phi_1}{\partial t_2} - M_1 \frac{\partial \phi_1}{\partial t_1} - M_2 \frac{\partial \phi_1}{\partial t_0} - M_0 \frac{\partial \phi_2}{\partial t_1} - M_1 \frac{\partial \phi_2}{\partial t_0} \\ &+ L_1\phi_2 + L_2\phi_1 + b_0(\phi_1, \phi_2) + b_0(\phi_2, \phi_1) + b_1(\phi_1, \phi_1) \end{aligned} \tag{3.27}$$

3.4.1 Equation at order ϵ

The problem at order ϵ simply coincides with the linear stability analysis Eq. (3.15), and provides the linear eigenmodes.

We define the adjoint problem as

$$M^+\frac{\partial\phi^+}{\partial t} = L\phi^+ \tag{3.28}$$

where the adjoint operators are defined by the following relations:

$$\left\langle M\frac{\partial\phi}{\partial t}, \phi^+ \right\rangle = \left\langle \phi, M^+\frac{\partial\phi^+}{\partial t} \right\rangle \tag{3.29}$$

$$\left\langle L\phi, \phi^+ \right\rangle = \left\langle L\phi^+, \phi \right\rangle \tag{3.30}$$

M is self-adjoint, so that $M^+ = M$. Integrating by parts, we find

$$L^+ = \begin{bmatrix} \frac{Pr}{\sqrt{Ra}}\nabla^4 + \frac{\partial}{\partial z}\nabla^2(W\cdot) - \frac{\partial^2 W}{\partial x^2}\frac{\partial}{\partial z} & -\frac{\partial\Theta}{\partial x}\frac{\partial}{\partial z} \\ -Pr\frac{\partial}{\partial x} & \frac{1}{\sqrt{Ra}}\nabla^2 + W\frac{\partial}{\partial z} \end{bmatrix} \tag{3.31}$$

The associated boundary conditions are found to be the same homogeneous conditions (3.12)-(3.14) as for the linear stability problem. The adjoint mode ϕ^+ is the solution of Eq. (3.28), and it will be used to impose the solvability condition at higher order expansions in ϵ of the problem.

3.4.2 Equation at order ϵ^2

The problem at order ϵ^2 is inhomogeneous.

$$(M_0\frac{\partial}{\partial t_0} - L_0)\phi_2 = f_2 \tag{3.32}$$

where

$$f_2 = b_0(\phi_1, \phi_1) + L_1\phi_1 - M_1\frac{\partial\phi_1}{\partial t_0} - M_0\frac{\partial\phi_1}{\partial t_1} \tag{3.33}$$

We need to calculate f_2 explicitly. Once f_2 obtained we solve the inhomogeneous equation $(M_0\frac{\partial}{\partial t_0} - L_0)\phi_2 = f_2$. The solution of this equation is the sum of the solution of the associated homogeneous equation $\phi_2^{(H)}$ and a particular solution $\phi_2^{(P)}$ of the inhomogeneous equation. For

$\phi_2^{(H)}$, the associated homogeneous equation is the same as the linear problem (3.15) at order ϵ^1. $\phi_2^{(H)}$ will be proportional to ϕ_1, i.e. $\phi_2^{(H)} = B(t_1,t_2,z_1)\hat{\phi}_1(x)e^{ik_c z} + C.C.$. At the end of the resolution procedure, by collecting the solutions at different orders, there will be a term of the type $\epsilon(A+\epsilon B)\hat{\phi}_1(x)e^{ik_c z} + C.C.$. Then, we are looking for the particular solution (P) $\phi_2^{(P)}$, by solving the equation $(M_0\frac{\partial}{\partial t_0} - L_0)\phi_2^{(P)} = f_2$. For the resonant forcing (R), a compatibility condition should be imposed, so that we compute the solution $\phi_2^{(PR)}$. Finally, we will obtain a particular solution $\phi_2^{(P)} = \phi_2^{(PNR)} + \phi_2^{(PR)}$.

In Eq. (3.33), $b_0(\phi_1,\phi_1)$ corresponds to nonresonant forcing (NR) $f_2^{(NR)}$ and $L_1\phi_1 - M_0\frac{\partial \phi_1}{\partial t_1}$ corresponds to resonant forcing $f_2^{(R)}$. Details of the calculations are presented as follows:

Calculation of f_2

The solution $\phi_1 = A(t_1,t_2,z_1)\hat{\phi}_1(x)e^{ik_c z} + C.C.$ is calculated in the problem at order ϵ, i.e. $\psi_1 = A(t_1,t_2,z_1)\hat{\psi}_1(x)e^{ik_c z} + C.C.$ for the stream function and $\theta_1 = A(t_1,t_2,z_1)\hat{\theta}_1(x)e^{ik_c z} + C.C.$ for temperature.

For the first term (Eq. 3.33), we find

$$
\begin{aligned}
b_{0,\psi}(\phi_1,\phi_1) &= \left(\frac{\partial \psi_1}{\partial z}\frac{\partial}{\partial x} - \frac{\partial \psi_1}{\partial x}\frac{\partial}{\partial z}\right)\nabla^2\psi_1 \\
&= b_{(\psi,A^2)}A^2e^{2ik_c z} + b_{(\psi,AA^*)}AA^* + b_{(\psi,A^{*2})}A^{*2}e^{-2ik_c z} \qquad (3.34)\\
b_{0,\theta}(\phi_1,\phi_1) &= \left(\frac{\partial \psi_1}{\partial z}\frac{\partial}{\partial x} - \frac{\partial \psi_1}{\partial x}\frac{\partial}{\partial z}\right)\theta_1 \\
&= b_{(\theta,A^2)}A^2e^{2ik_c z} + b_{(\theta,AA^*)}AA^* + b_{(\theta,A^{*2})}A^{*2}e^{-2ik_c z} \qquad (3.35)
\end{aligned}
$$

with

$$b_{(\psi,A^2)} = ik(\psi_1\psi_1^{(3)} - \psi_1'\psi_1'') \tag{3.36}$$

$$b_{(\psi,AA^*)} = ik(\psi_1\psi_1^{*(3)} - \psi_1^*\psi_1^{(3)} + \psi_1'\psi_1''^* - \psi_1'^*\psi_1'') \tag{3.37}$$

$$b_{(\psi,A^{*2})} = -ik(\psi_1^*\psi_1^{*(3)} - \psi_1'^*\psi_1''^*) \tag{3.38}$$

$$b_{(\theta,A^2)} = ik(\psi_1\theta_1' - \psi_1'\theta_1) \tag{3.39}$$

$$b_{(\theta,AA^*)} = ik(\psi_1\theta_1'^* - \psi_1^*\theta_1' + \psi_1'\theta_1^* - \psi_1'^*\theta_1) \tag{3.40}$$

$$b_{(\theta,A^{*2})} = ik(\psi_1^*\theta_1'^* - \psi_1'^*\theta_1^*) \tag{3.41}$$

where A^* represents the complex conjugate of A, and $'$, $''$, (3) denotes the first, second, and third derivatives with respect to x, respectively. These terms are nonresonant, so we note it as

$$f_2^{(NR)} = b_{A^2}A^2e^{2ik_cz} + b_{AA^*}AA^* + b_{A^{*2}}A^{*2}e^{-2ik_cz} \tag{3.42}$$

with

$$b_{A^2} = \begin{bmatrix} b_{(\psi,A^2)} \\ b_{(\theta,A^2)} \end{bmatrix}; \quad b_{AA^*} = \begin{bmatrix} b_{(\psi,AA^*)} \\ b_{(\theta,AA^*)} \end{bmatrix}; \quad b_{A^{*2}} = \begin{bmatrix} b_{(\psi,A^{*2})} \\ b_{(\theta,A^{*2})} \end{bmatrix} \tag{3.43}$$

Solution of $\phi_2^{(PNR)}$

We are solving the inhomogeneous problem to look for $\phi_2^{(PNR)}$ with the same form of nonresonant forcing $\phi_2^{(PNR)} = \phi_{21}+\phi_{22}+\phi_{23} = \hat{\phi}_{21}A^2e^{2ik_cz}+\hat{\phi}_{22}AA^*+\hat{\phi}_{23}A^{*2}e^{-2ik_cz}$. We have three discrete linear systems to solve

$$\tilde{\mathcal{L}}_2\hat{\phi}_{21} = b_{A^2}; \quad \tilde{\mathcal{L}}_0\hat{\phi}_{22} = b_{AA^*}; \quad \tilde{\mathcal{L}}_{-2}\hat{\phi}_{23} = b_{A^{*2}} \tag{3.44}$$

where

$$\tilde{\mathcal{L}}_j = -\begin{bmatrix} \frac{Pr}{\sqrt{Ra}}\left(\frac{\partial^2}{\partial x^2} - (jk_c)^2\right)^2 - Wijk_c\left(\frac{\partial^2}{\partial x^2} - (jk_c)^2\right) + \frac{\partial^2 W}{\partial x^2}ijk_c & Pr\frac{\partial}{\partial x} \\ \frac{\partial\Theta}{\partial x}ijk_c & \frac{1}{\sqrt{Ra}}\nabla^2 - Wijk_c \end{bmatrix} \tag{3.45}$$

Calculation of $f_2^{(R)}$

$$L_1\phi_1 = L_1 \begin{bmatrix} \hat{\psi}_1 \\ \hat{\theta}_1 \end{bmatrix} A(t_1,t_2,z_1)e^{ik_c z} + C.C$$
$$= \begin{bmatrix} d_1 \\ d_2 \end{bmatrix} \frac{\partial A(t_2,t_1,z_1)}{\partial z_1} e^{ik_c z} + C.C. \tag{3.46}$$

where

$$d_1 = \left(-4ik_c^3 \frac{Pr}{\sqrt{Ra}} + 3Wk_c^2 + \frac{\partial^2 W}{\partial x^2}\right)\hat{\psi}_1 + \left(\frac{4Pr}{\sqrt{Ra}} ik_c - W\right)\hat{\psi}_1'' \tag{3.47}$$
$$d_2 = \frac{\partial \Theta}{\partial x}\hat{\psi}_1 + \left(\frac{2}{\sqrt{Ra}} ik_c - W\right)\hat{\theta}_1 \tag{3.48}$$

$$-M_1 \frac{\partial \phi_1}{\partial t_0} = 0 \tag{3.49}$$

since it is evaluated at the linear stability threshold ($s_c = 0$).

The last term is $-M_0 \dfrac{\partial \phi_1}{\partial t_1}$. We have:

$$-M_0 \frac{\partial \phi_1}{\partial t_1} = -\begin{bmatrix} d_3 \\ d_4 \end{bmatrix} \frac{\partial A(t_2,t_1,z_1)}{\partial t_1} e^{ik_c z} + C.C. \tag{3.50}$$

where

$$d_3 = \hat{\psi}_1'' - k_c^2 \hat{\psi}_1 \tag{3.51}$$
$$d_4 = \hat{\theta}_1 \tag{3.52}$$

Therefore, we have

$$f_2^{(R)} = \begin{bmatrix} d_1 \\ d_2 \end{bmatrix} \frac{\partial A(t_2,t_1,z_1)}{\partial z_1} e^{ik_c z} - \begin{bmatrix} d_3 \\ d_4 \end{bmatrix} \frac{\partial A(t_2,t_1,z_1)}{\partial t_1} e^{ik_c z} + C.C. \tag{3.53}$$

Compatibility equation for $f_2^{(R)}$

We look for a particular solution with the same kind of forcing $f_2^{(R)}$, noted as $\phi_2^{(PR)} = \tilde{\phi}_2^{(PR)}(x)$ $e^{ik_c z} + C.C.$. Substituting into the system $\mathcal{L}_0\phi_2^{(PR)} = f_2^{(R)}$ we obtain the system $\tilde{\mathcal{L}}_0\tilde{\phi}_2^{(PR)} = \tilde{f}_2^{(R)}$. We then need to solve the inhomogeneous linear algebriac system in the case that the associated homogeneous algebriac system has non-trivial solutions. Note that we have $det(\tilde{\mathcal{L}}_0) = 0$ where $\tilde{\mathcal{L}}_0$ was already solved in the direct problem (3.15). The Fredholm theorem ensures that a solution for this system exists if and only if the forcing term is orthogonal to the solution ϕ_1^+ of the associated homogeneous adjoint system $\tilde{\mathcal{L}}_0^+\tilde{\phi}_1^+ = 0$ i.e. if

$$\left\langle \tilde{\phi}_1^+, \tilde{f}_2^{(R)} \right\rangle = 0 \tag{3.54}$$

The adjoint operator $\tilde{\mathcal{L}}_0^+$ is given as the complex conjugate matrix in the sense of Hermitian $\tilde{\mathcal{L}}_0$.

Here, we have two resonant terms, on which we should impose a compatibility condition, i.e.

$$\langle L_1\phi_1 - M_0\frac{\partial\phi_1}{\partial t_1}, \phi^+\rangle = 0 \tag{3.55}$$

where $\langle , \rangle$ denotes the inner product, and ϕ^+ the adjoint vector given by the adjoint problem (3.28). This compatibility condition yields an expression for the group velocity C_g, defined as $\frac{\partial A}{\partial t_1} = C_g\frac{\partial A}{\partial z_1}$. Numerical evaluation of $C_g = \frac{\langle d_1, \psi^+\rangle + \langle d_2, \theta^+\rangle}{\langle d_3, \psi^+\rangle + \langle d_4, \theta^+\rangle}$ yields a value of about 10^{-5}, which is close to the expected value of zero corresponding to stationary rolls. The discrepancy is likely to be due to the discretization error.

Finally, in matrix form, we have the resonant forcing which will be used to calculate the particular solution $\phi_2^{(R)}$

$$\begin{aligned} f_2^{(R)} &= \begin{bmatrix} d_1 - C_g d_3 \\ d_2 - C_g d_4 \end{bmatrix} \frac{\partial A(t_1, t_2, z_1)}{\partial z_1} e^{ik_c z} + C.C \\ &= b^{(R)} \frac{\partial A(t_1, t_2, z_1)}{\partial z_1} e^{ik_c z} + C.C. \end{aligned} \tag{3.56}$$

Solution of $\phi_2^{(PR)}$

In order to find the particular solution $\phi_2^{(PR)}$ associated with the resonant term $f_2^{(R)}$, we need to solve the linear discret system

$$\tilde{\mathcal{L}}_0\phi_2^{(PR)} = b^{(R)}\frac{\partial A(t_1,t_2,z_1)}{\partial z_1} \tag{3.57}$$

In conclusion, we obtain the particular solution at order ϵ^2: $\phi_2^{(P)} = \phi_2^{(PNR)} + \phi_2^{(PR)}$, where

$$\phi_2^{(PNR)} = \hat{\phi}_{21}A^2e^{2ik_cz} + \hat{\phi}_{22}AA^* + \hat{\phi}_{23}A^{*2}e^{-2ik_cz} \tag{3.58}$$

$$\phi_2^{(PR)} = \hat{\phi}_{24}\frac{\partial A}{\partial z_1}e^{ik_cz} + C.C. \tag{3.59}$$

$\hat{\phi}_{2n}$ defined as the n-th component of the 2nd order solution. This particular solution $\phi_2^{(P)}$ will be used to calculate f_3 at order ϵ^3.

3.4.3 Equation at order ϵ^3

The problem at order ϵ^3 is also inhomogeneous :

$$(M_0\frac{\partial}{\partial t_0} - L_0)\phi_3 = f_3 \tag{3.60}$$

where

$$\begin{aligned} f_3 = &-M_0\frac{\partial\phi_1}{\partial t_2} - M_1\frac{\partial\phi_1}{\partial t_1} - M_2\frac{\partial\phi_1}{\partial t_0} - M_0\frac{\partial\phi_2}{\partial t_1} - M_1\frac{\partial\phi_2}{\partial t_0} \\ &+L_1\phi_2 + L_2\phi_1 + b_0(\phi_1,\phi_2) + b_0(\phi_2,\phi_1) + b_1(\phi_1,\phi_1) \end{aligned} \tag{3.61}$$

As at order ϵ^2, we should firstly calculate f_3 explicitly. Once f_3 obtained, we can solve the inhomogeneous system $(M_0\frac{\partial}{\partial t_0} - L_0)\phi_3 = f_3$. The solution of this equation will be given as a sum of the solution of associated homogeneous equation $\phi_3^{(H)}$ and the particular solution $\phi_3^{(P)}$ of the inhomogeneous equation. We will see that the particular solution $\phi_3^{(P)}$ is composed with the nonresonant solution $\phi_3^{(PNR)}$ and the resonant solution $\phi_3^{(PR)}$. As we have seen at

order ϵ^2, if we want to calculate $\phi_3^{(PR)}$, we have to impose a compatibility condition on the resonant forcing term $f_3^{(R)}$. This compatibility equation gives us a relation for the perturbation amplitude $A(t_1, t_2, z_1)$ and allows us to calculate the weakly nonlinear solution of our problem (Ginzburg-Landau Model). Therefore, here, we will only need to look for the resonant forcing term $f_3^{(R)}$.

Calculation of $f_3^{(R)}$

The solution at order ϵ^1 is already obtained as: $\phi_1 = A(t_1, t_2, z_1)\hat{\phi}_1(x)e^{ik_c z} + C.C.$ At the order ϵ^2 as well: $\phi_2 = \hat{\phi}_{21}A^2e^{2ik_c z} + \hat{\phi}_{22}AA^* + \hat{\phi}_{23}A^{*2}e^{-2ik_c z} + \hat{\phi}_{24}\frac{\partial A}{\partial z_1}e^{ik_c z} + \hat{\phi}_{24}^*\frac{\partial A^*}{\partial z_1}e^{-ik_c z}$, i.e. $\psi_2 = \hat{\psi}_{21}A^2e^{2ik_c z} + \hat{\psi}_{22}AA^* + \hat{\psi}_{23}A^{*2}e^{-2ik_c z} + \hat{\psi}_{24}\frac{\partial A}{\partial z_1}e^{ik_c z} + \hat{\psi}_{24}^*\frac{\partial A^*}{\partial z_1}e^{-ik_c z}$ for the stream function and $\theta_2 = \hat{\theta}_{21}A^2e^{2ik_c z} + \hat{\theta}_{22}AA^* + \hat{\theta}_{23}A^{*2}e^{-2ik_c z} + \hat{\theta}_{24}\frac{\partial A}{\partial z_1}e^{ik_c z} + \hat{\theta}_{24}^*\frac{\partial A^*}{\partial z_1}e^{-ik_c z}$ for the temperature. Note that we omit the homogeneous solution at order ϵ^2 since it takes the form as ϕ_1.

We have

$$\begin{aligned} f_3 = &-M_0\frac{\partial \phi_1}{\partial t_2} - M_1\frac{\partial \phi_1}{\partial t_1} - M_2\frac{\partial \phi_1}{\partial t_0} - M_0\frac{\partial \phi_2}{\partial t_1} - M_1\frac{\partial \phi_2}{\partial t_0} \\ &+L_1\phi_2 + L_2\phi_1 + b_0(\phi_1, \phi_2) + b_0(\phi_2, \phi_1) + b_1(\phi_1, \phi_1) \end{aligned} \tag{3.62}$$

where

$$-M_0\frac{\partial \phi_1}{\partial t_2} = -\begin{bmatrix} \hat{\psi}_1'' - k_c^2\hat{\psi}_1 \\ \hat{\theta}_1 \end{bmatrix}\frac{\partial A}{\partial t_2}e^{ik_c z} \tag{3.63}$$

$$-M_1\frac{\partial \phi_1}{\partial t_1} = -2C_g\begin{bmatrix} ik_c\hat{\psi}_1 \\ 0 \end{bmatrix}\frac{\partial^2 A}{\partial z_1^2}e^{ik_c z} \tag{3.64}$$

$$-M_1\frac{\partial \phi_2}{\partial t_0} = 0 \tag{3.65}$$

$$-M_2\frac{\partial \phi_1}{\partial t_0} = 0 \tag{3.66}$$

As it is evaluated at the linear stability threshold ($s_c = 0$), then

$$-M_0\frac{\partial\phi_2}{\partial t_1} = -C_g\begin{bmatrix}\hat{\psi}_{24}'' - k_c^2\hat{\psi}_{24}\\ \hat{\theta}_{24}\end{bmatrix}\frac{\partial^2 A}{\partial z_1^2}e^{ik_cz} + NRT \tag{3.67}$$

where NRT is short for "Non Resonant Terms".

Applying the operator L_2 (see appendix Eq (A.4)) to ϕ_1, we obtain

$$\begin{aligned}L_2\phi_1 = &\frac{\partial^2 A}{\partial z_1^2}\begin{bmatrix}\frac{2Pr}{\sqrt{Ra_c}}(\hat{\psi}_1'' - 3k_c^2\hat{\psi}_1) - 3Wik_c\hat{\psi}_1\\ \frac{1}{\sqrt{Ra_c}}\hat{\theta}_1\end{bmatrix}e^{ik_cz}\\ &-\frac{1}{2}Ra_c^{-1.5}\begin{bmatrix}Pr(\hat{\psi}_1^{(4)} - 2k_c^2\hat{\psi}_1'' + k_c^4\hat{\psi}_1)\\ \hat{\theta}_1'' - k_c^2\hat{\theta}_1\end{bmatrix}Ae^{ik_cz}\\ &-\frac{1}{2Ra_c}\begin{bmatrix}W(ik_c\hat{\psi}_1'' - ik_c^3\hat{\psi}_1) - \frac{\partial^2 W}{\partial x^2}ik_c\hat{\psi}_1\\ Wik_c\hat{\theta}_1\end{bmatrix}Ae^{ik_cz} + C.C.\end{aligned} \tag{3.68}$$

which contains resonant terms. These resonant terms can be separated into two parts, one is about the secondary spatial derivation of the amplitude and the other is linear to the amplitude.

For $L_1\phi_2$, L_1 is a linear operator, and ϕ_{21}, ϕ_{22}, ϕ_{23} only contain constant terms about e^{2ik_cz} or e^{-2ik_cz}, so $L_1\phi_{21}$, $L_1\phi_{22}$, $L_1\phi_{23}$ do not contain resonant terms. However, ϕ_{24} has a contribution to the resonant term, as

$$L_1\phi_{24} = \begin{bmatrix}\left(-4ik_c^3\frac{Pr}{\sqrt{Ra}} + 3Wk_c^2 + \frac{\partial^2 W}{\partial x^2}\right)\hat{\psi}_{24} + \left(\frac{4Pr}{\sqrt{Ra}}ik_c - W\right)\hat{\psi}_{24}''\\ \frac{\partial\Theta}{\partial x}\hat{\psi}_{24} + \left(\frac{2}{\sqrt{Ra}}ik_c - W\right)\hat{\theta}_{24}\end{bmatrix}\frac{\partial A^2}{\partial z_1^2}e^{ik_cz} + C.C. \tag{3.69}$$

For quadratic terms, we have

$$
\begin{aligned}
b_{0,\phi}(\pi_1,\phi_2) &= \left(\frac{\partial\psi_1}{\partial z}\frac{\partial}{\partial x}-\frac{\partial\psi_1}{\partial x}\frac{\partial}{\partial z}\right)\nabla^2\psi_2 \\
&= (ik\hat{\psi}_1\hat{\psi}_{22}^{(3)}+4ik^3\hat{\psi}_1^*\hat{\psi}_{21}'-ik\hat{\psi}_1^*\hat{\psi}_{21}^{(3)}-2ik\hat{\psi}_1'^*\hat{\psi}_{21}''+8ik^3\hat{\psi}_1'^*\hat{\psi}_{21})A^2A^*e^{ik_cz} \\
&+ (ik\hat{\psi}_1\hat{\psi}_{23}^{(3)}-4ik^3\hat{\psi}_1\hat{\psi}_{23}'+2ik\hat{\psi}_1'\hat{\psi}_{23}''-ik\hat{\psi}_1^*\hat{\psi}_{22}^{(3)}-8ik^3\hat{\psi}_1'\hat{\psi}_{23})AA^{*2}e^{-ik_cz} \\
&+ NRT \\
b_{0,\theta}(\phi_1,\phi_2) &= \left(\frac{\partial\psi_1}{\partial z}\frac{\partial}{\partial x}-\frac{\partial\psi_1}{\partial x}\frac{\partial}{\partial z}\right)\theta_2 \\
&= (ik\hat{\psi}_1\hat{\theta}_{22}'-ik\hat{\psi}_1^*\hat{\theta}_{21}'-2ik\hat{\psi}_1'^*\hat{\theta}_{21})A^2A^*e^{ik_cz} \\
&+ (ik\hat{\psi}_1\hat{\theta}_{23}'-ik\hat{\psi}_1^*\hat{\theta}_{22}'+2ik\hat{\psi}_1'\hat{\theta}_{23})AA^{*2}e^{-ik_cz} \\
&+ NRT
\end{aligned}
\tag{3.70}
$$

$$
\begin{aligned}
b_{0,\psi}(\phi_2,\phi_1) &= \left(\frac{\partial\psi_2}{\partial z}\frac{\partial}{\partial x}-\frac{\partial\psi_2}{\partial x}\frac{\partial}{\partial z}\right)\nabla^2\psi_1 \\
&= (2ik\hat{\psi}_1^{*(3)}\hat{\psi}_{21}-2ik^3\hat{\psi}_1'^*\hat{\psi}_{21}+ik\hat{\psi}_1''^*\hat{\psi}_{21}'-ik^3\hat{\psi}_1^*\hat{\psi}_{21}'-ik\hat{\psi}_1''\hat{\psi}_{22}'+ik^3\hat{\psi}_{22}'\hat{\psi}_1)A^2A^*e^{ik_cz} \\
&+ (-2ik\hat{\psi}_1^{(3)}\hat{\psi}_{23}+2ik^3\hat{\psi}_1'\hat{\psi}_{23}+ik\hat{\psi}_1''^*\hat{\psi}_{22}'-ik^3\hat{\psi}_1^*\hat{\psi}_{22}'-ik\hat{\psi}_1''\hat{\psi}_{23}'+ik^3\hat{\psi}_{23}'\hat{\psi}_1)AA^{*2}e^{-ik_cz} \\
&+ NRT \\
b_{0,\theta}(\phi_2,\phi_1) &= \left(\frac{\partial\psi_2}{\partial z}\frac{\partial}{\partial x}-\frac{\partial\psi_2}{\partial x}\frac{\partial}{\partial z}\right)\theta_1 \\
&= (2ik\hat{\psi}_{21}\hat{\theta}_1'^*-ik\hat{\psi}_{22}'\hat{\theta}_1+ik\hat{\psi}_{21}'\hat{\theta}_1^*)A^2A^*e^{ik_cz} \\
&+ (-2ik\hat{\psi}_{23}\hat{\theta}_1'-ik\hat{\psi}_{23}'\hat{\theta}_1+ik\hat{\psi}_{22}'\hat{\theta}_1^*)AA^{*2}e^{-ik_cz} \\
&+ NRT
\end{aligned}
\tag{3.71}
$$

The nonlinear term $b_1(\phi_1,\phi_1)$ does not contain any resonant term.

Collecting all the resonant terms, we obtain

$$f_3^{(R)} = \left(c_1 \frac{\partial A}{\partial t_2} + c_2 A + c_3 A^2 A^* + c_4 \frac{\partial^2 A}{\partial z_1^2} \right) e^{ik_c z} + C.C. \tag{3.72}$$

where c_1, c_2, c_3, c_4 are x-dependent functions defined in the Appendix.

Solvability condition for $f_3^{(R)}$

Once f_3 is calculated, we should be able to solve the inhomogeneous equation $(M_0 \frac{\partial}{\partial t_0} - L_0)\phi_3 = f_3$. The solution of this equation will be given as the sum of the solution of associated homogeneous equation $\phi_3^{(H)}$ and the particular solution $\phi_3^{(P)}$ given by the inhomogeneous equation. The particular solution $\phi_3^{(P)}$ is composed of the nonresonant solution $\phi_3^{(PNR)}$ and the resonant solution $\phi_3^{(PR)}$. As we have seen at order ϵ^2, if we want to calculate $\phi_3^{(PR)}$, we need to impose a solvability condition on the resonant forcing $f_3^{(R)}$.

The enforcement of the solvability condition $\langle f_3^R, \phi^+ \rangle = 0$ leads to a Ginzburg-Landau equation [58] for the amplitude A:

$$\frac{\partial A}{\partial t} = \sigma A + \gamma \frac{\partial^2 A}{\partial z^2} - l A^2 A^* \tag{3.73}$$

As the amplitude around the threshold is proportional to ϵA, we redefine the new amplitude $\overline{A} = \epsilon A$, which is independent of the scale ϵ. Then the Ginzburg-Landau equation in the primitive variables reads as:

$$\frac{\partial \overline{A}}{\partial t} = \sigma(Ra - Ra_c)\overline{A} + \gamma \frac{\partial^2 \overline{A}}{\partial z^2} - l \overline{A}^2 \overline{A}^* \tag{3.74}$$

where

$$\sigma = -\frac{\langle c_2, \phi^+ \rangle}{\langle c_1, \phi^+ \rangle} \qquad \gamma = -\frac{\langle c_4, \phi^+ \rangle}{\langle c_1, \phi^+ \rangle} \qquad l = -\frac{\langle c_3, \phi^+ \rangle}{\langle c_1, \phi^+ \rangle} \tag{3.75}$$

Numerical evaluation of the coefficients σ, γ, l for the critical wavenumber $k_c = 2.81$ gives $\sigma = 7.67 \times 10^{-5}$, $\gamma = 0.112$, $l = 20.45$. The sign of l indicates that the bifurcation is supercritical.

The amplitude of perturbations predicted by this Ginzburg-Landau equation will be compared with the DNS results discussed in the next section 3.5.1.

3.4.4 Absolute instability

The analysis of absolute/convective instability can be applied to the Ginzburg-Landau equation in our system. First of all, we introduce the notion of absolute/convective instability by following Huerre [59], and then apply the standard analysis procedure to our Ginzburg-Landau equation.

Convective/absolute instability

We consider a partial differential equation solely involving the streamwise variable x and time t. Let $G(x,t)$ be the Green function or impulse response defined by

$$D[-i\frac{\partial}{\partial x}, i\frac{\partial}{\partial t}; R]G(x,t) = \delta(x)\delta(t) \tag{3.76}$$

where $i = \sqrt{-1}$, δ denotes the Dirac delta function, and D is the dispersion relation, R is the control parameter. The fundamental solution G contains all the information regarding the spatio-temporal dynamics of the perturbation field. Several types of impulse response behavior are possible depending on the value of R, as sketched in Figure 3.3. One may first distinguish between stable and unstable flows:

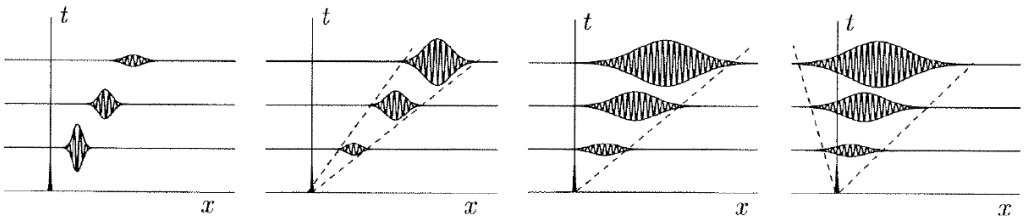

Figure 3.3: Linear impulse response $G(x,t)$. (a) Linear stable flow; (b) linearly convective unstable flow; (c) marginally convectively/absolutely unstable flow; (d) absolutely unstable flow. From P. Huerre, Perspectives in fluid dynamics, 2000 [59].

A flow is linearly stable if

$$\lim_{t\to\infty} G(x,t) = 0 \quad \text{along all rays} \quad \frac{x}{t} = const.$$

The impulse response then consists of a decaying wavepacket (Figure 3.3 (a)).

Otherwise, the flow is linearly unstable if

$$\lim_{t\to\infty} G(x,t) = \infty \quad \text{along at least one ray} \quad \frac{x}{t} = const.$$

The impulse response typically consists of an unstable wavepacket confined within a wedge or several wedges in the (x,t)-plane (Figure 3.3 (b)-(d)). In the later case, we can further distinguish between absolute instability and the convective instability.

An unstable flow is said to be linearly convectively unstable if

$$\lim_{t\to\infty} G(x,t) = 0 \quad \text{along the ray} \quad \frac{x}{t} = 0$$

The impulse response is advected away to leave the source ultimately undisturbed (Figure 3.3 (b)).

An unstable flow is said to be linearly absolutely unstable if

$$\lim_{t\to\infty} G(x,t) = \infty \quad \text{along the ray} \quad \frac{x}{t} = 0$$

In this case, the unstable wavepacket is amplified at the source and gradually contaminates the entire medium (Figure 3.3 (d)).

Application to our system

The standard procedure of absolute/convective instability is applied to our system in the following way. The linearized Ginzburg-Landau equation takes the form

$$\frac{\partial \overline{A}}{\partial t} = \sigma(Ra - Ra_c)\overline{A} + \gamma \frac{\partial^2 \overline{A}}{\partial z^2} \tag{3.77}$$

The introduction of a particular solution in the form of normal modes $\overline{A} = \hat{A}e^{i(\beta z - \omega t)}$ into Eq.(3.77) results in the dispersion relation:

$$D(\omega, \beta, Ra) = \sigma(Ra - Ra_c) + i\omega - \gamma\beta^2 = 0 \tag{3.78}$$

It can be written in the form of a single temporal mode $\omega(\beta, \sigma, Ra) = i[\sigma(Ra - Ra_c) - \gamma\beta^2]$, which has an equilibrium (β_0, ω_0), satisfying the conditions $\omega_0 = \omega(\beta_0)$ and $\frac{\partial\omega}{\partial\beta}(\beta_0) = 0$. The latter condition yields $\frac{\partial\omega}{\partial\beta}(\beta_0) = -2i\gamma\beta_0 = 0$. So, $\beta_0 = 0$ and $\omega_0 = i\sigma(Ra - Ra_c)$. As the amplication rate $\omega_{0,i} = \sigma(Ra - Ra_c) > 0$, the disturbance grows with time at any fixed station in the laboratory frame, which corresponds to the absolute instability, in agreement with Tao and Zhuang [15]'s results.

3.5 2D DNS simulations $A_z = 10$

We use a 2D simulation to study the development of instabilities in the flow between two vertical plates maintained at different temperatures. 40 Chebyshev modes are used for the spatial discretization in x-direction, while 160 Fourier modes are used for the z-direction. Convergence for the spatial discretization was established [23]. Results are summarized in Table 3.1.

3.5.1 First bifurcation

As predicted by the linear stability analysis, the base flow bifurcates to 4 steady corotating rolls at $Ra_c \sim 5708$. Although vertical invariance is broken, the solution still displays the symmetry D_4, consisting of translation by the height $A_z/4$ of each of the rolls and the Boussinesq centrosymmetry. Invariance of the equations under z-translations ensures that there exists a whole circle of solutions, corresponding to an arbitrary vertical translation of the rolls: the bifurcation is a circle pitchfork bifurcation.

The time evolution of the temperature measured at the point ($x = 0.0381$, $z = 5$), located in the hot boundary layer, is plotted in Figure 3.4 (a). An enlargement of the same signal for the times $1400 < t < 2000$ is represented in logarithmic scale in Figure 3.4 (b). The temperature

disturbance grows exponentially for $1400 < t < 1750$, which corresponds to the linear growth of the most unstable eigenmode, then increases at a slower rate for $t > 1750$ before the amplitude of the solution saturates. As was pointed out by Henderson and Barkley [60], this evolution shows that the coefficient of the cubic term in the normal form of the circle pitchfork bifurcation is negative, and therefore the bifurcation is supercritical in agreement with the prediction of the Ginzburg-Landau model (GLM).

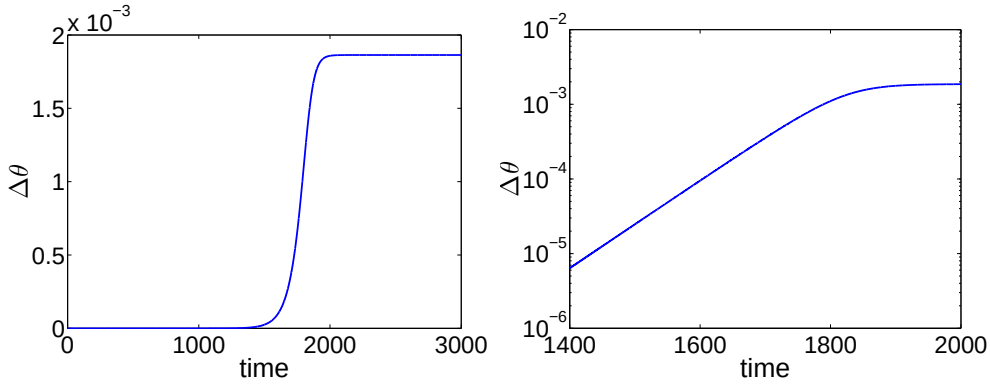

(a) (b)

Figure 3.4: (a): Time series of temperature perturbation $\Delta\theta$ with respect to the base flow at point (0.0381, 5) in the boundary layer near the hot wall at $Ra = 6000$. (b): An enlargement of (a) for $1400 < t < 2000$ on a logarithmic scale, $A_z = 10$.

Comparaison of perturbation amplitude between DNS and GLM

The steady amplitude A computed from the Ginzburg-Landau equation is compared with the amplitude of the velocity and temperature perturbations observed in the DNS, for a domain which is as close as possible to the critical wavelength $\lambda_c = 2.236$. The periodic height of the DNS was adjusted to $A_z = 9$, so that it featured a wavelength of $\lambda = 2.25$ close to λ_c. Figures 3.5 (a) and (b) show that the agreement between the Ginzburg-Landau model and the DNS is very good for both the temperature and velocity up to $Ra \sim 6300$ (about 10% larger than Ra_c). Beyond that, the Ginzburg-Landau model is no longer valid to represent the flow at higher Rayleigh numbers.

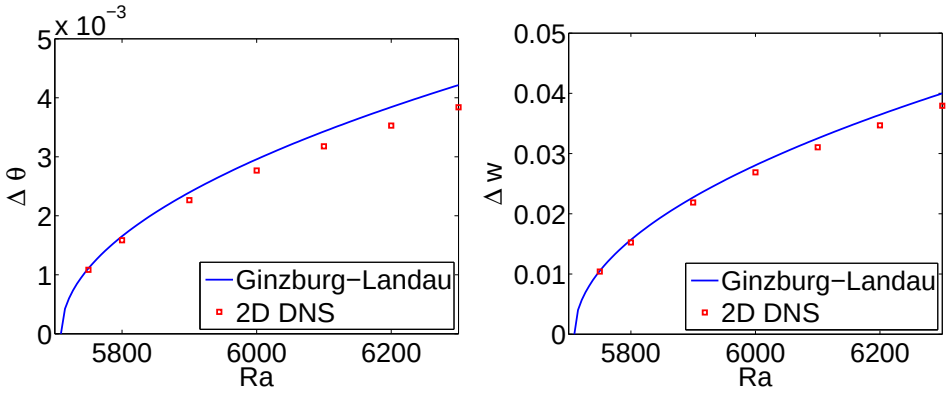

(a) (b)

Figure 3.5: Comparison of the maximum amplitudes of perturbation with respect to the base flow observed in the DNS at $x = 0.0381$ with the Ginzburg-Landau equation prediction: (a) temperature, (b) vertical velocity, $A_z = 9$.

3.5.2 Subsequent bifurcations

Figure 3.6 shows how the spatial organization of the flow varies with increasing Ra. Just above the critical Rayleigh number, the flow is characterized by four steady structures, as shown in Figure 3.6 (a) at $Ra = 6000$. As Ra is increased past the value of $Ra = 13500$, the four steady rolls merge into three rolls which oscillate in time, as shown in Figure 3.6 (b) and (c). At still higher Rayleigh numbers $Ra \geq 18000$, only two rolls of unequal size are observed, as is shown in Figure 3.6 (d).

The temporal spectrum of the vertical velocity at the point ($x = 0.0381$, $z = 0.683$) is shown in Figure 3.7 (a) for $Ra = 15000$, and is characterized by a main frequency (with harmonics) of $f_1 = 0.032$. When $15000 \leq Ra \leq 16000$, the flow still consists of 3 oscillatory rolls, but the temporal evolution of the flow becomes more complex. When Ra is increased to $Ra = 15500$, the flow becomes quasi-periodic with the appearance of a second, much lower frequency $f_2 = 0.0031$ (Figure 3.7 (b)). When $Ra = 16000$, the peaks around the main frequency f_1 and f_2 broaden, (see Figure 3.7 (c)), corresponding to a seemingly chaotic behavior. The chaotic behavior subsides beyond $Ra = 18000$, as the flow spatial pattern is modified: there seems to be a competition between the onset of purely temporal chaos in a specific flow pattern and the development of spatial instabilities at shorter wavenumbers. Up to $Ra = 21000$, which was the

highest Rayleigh number considered, the flow remains steady with a robust 2-roll pattern.

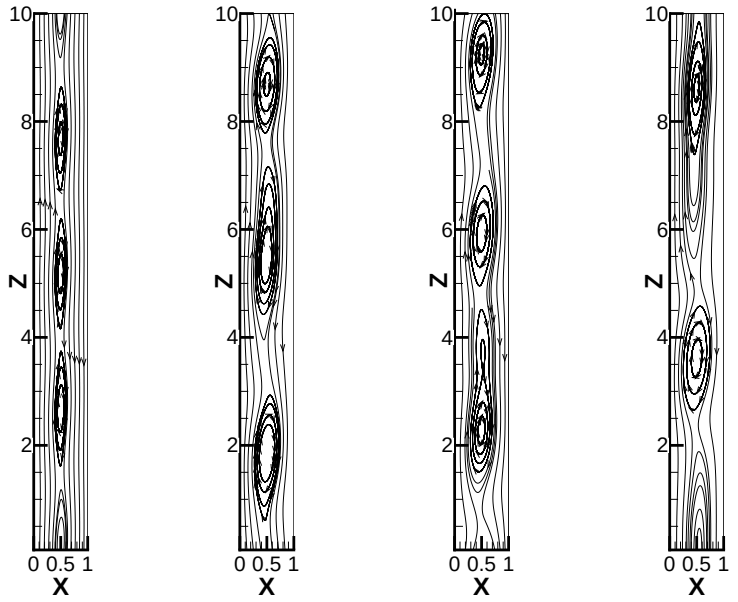

(a) Ra=6000 (b) Ra=13 500 (c) Ra=15 000 (d) Ra=18 000

Figure 3.6: 2D flow streamlines at different Ra. (a) four steady corotating rolls; (b) (c) three oscillating rolls; (d) two steady rolls, $A_z = 10$.

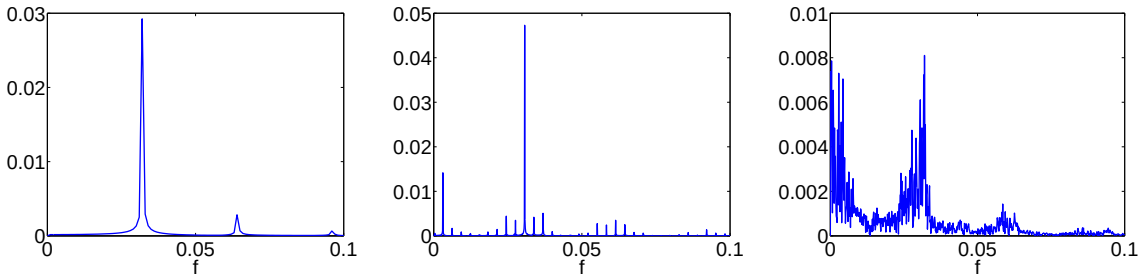

(a) $Ra = 15\,000$ (b) $Ra = 15\,500$ (c) $Ra = 16\,000$

Figure 3.7: Temporal Fourier spectrum of the vertical velocity at the point (0.0381, 0.683) in the boundary layer near the hot wall in 2D simulations for different Rayleigh numbers, $A_z = 10$.

3.6 Conclusion

Due to the Squire's theorem, the linear stability needs to be carried out in the 2D configuration, which predicts the first instability at $Ra_c = 5708$ with the wavenumber of the most unstable mode $k_c = 2.81$. A weakly nonlinear analysis results in the derivation of a Ginzburg-Landau

Table 3.1: Summary of bifurcations and associated flow structures and symmetries for the 2D simulations, $A_z = 10$.

Ra	Nature of Bifurcation	Spatial Features Number of Structures	Spatial Symmetry Temporal Symmetry
$Ra < Ra_c = 5708$		1D base flow	$O(2)$ steady
$Ra_c \leq Ra \leq 13000$	supercritical circle pitchfork	corotating rolls $n = 4$	D_4 steady
$13500 \leq Ra \leq 15300$	supercritical Hopf	corotating rolls $n = 3$	no symmetry periodic
$15400 \leq Ra \leq 15600$	unknown	corotating rolls $n = 3$	no symmetry quasi-periodic
$15700 \leq Ra \leq 17000$	unknown	corotating rolls $n = 3$	no symmetry "chaotic"
$18000 \leq Ra \leq 21000$	unknown	corotating rolls $n = 2$	no symmetry steady

equation which is able to predict correctly the amplitude of the 2D rolls for Rayleigh numbers within a limited range (10%) of Ra_c.

In 2D simulations, the first instability occurs at $Ra_c = 5708$, through which the parallel base flow turns into steady co-rotating rolls. A second bifurcation occurs at $Ra = 13500$. The flow becomes oscillatory, and the steady four-roll pattern turns into a periodic three-roll one with a characteristic frequency $f = 0.032$. When Ra is increased, the temporal evolution of the three unsteady rolls becomes quasiperiodic, then apparently chaotic, while the characteristic frequency f remains dominant. As Ra is further increased to $Ra = 18000$, the flow becomes steady again, and the three oscillatory rolls give way to two steady rolls. This suggests that the occurrence of pure temporal chaos is limited by the development of a vertical instability, which leads to a long-wavelength modulation of the spatial pattern. The two steady rolls remain stable over a range of Rayleigh numbers, as no chaotic behavior is observed up to $Ra = 21000$. All the results are summarized in Table 3.1.

Chapter 4

3D Channel of small transverse extent $A_z = 10$ & $A_y = 1$

4.1 Introduction

As we have seen in the previous chapter about asymptotic analysis, the approach of Ginzburg-Landau equation is only valid for a limited range of Rayleigh number to represent the flow around the threshold of the first instability. In the 2D DNS simulations, the temporally chaotic regime occurs within a limited range of Rayleigh number, after a few bifurcations. To determine whether these results hold in three dimensional configuration, we examine a 3D channel of small transverse direction $A_y = 1$. The vertical extent remains the same as in the 2D configuration $A_z = 10$. The simulation is divided into 4 subdomains along the z-direction. 40 Chebyshev modes are used for the spatial discretization of x-direction, 30 Fourier modes are used for the transverse direction y, and 40 Chebyshev modes are used in the z-direction for each subdomain.

4.2 First bifurcation

We first check that the base flow remains stable with respect to any perturbation when $Ra < Ra_c$. As expected, the first bifurcation observed in the DNS occurs at Ra_c around 5800, and is characterized by the appearance of four 2D steady corotating rolls which are represented in Figure 4.1. As mentioned in section (3.5.1), the vertical translation invariance is replaced with a D_4 symmetry, and the centro-Boussinesq symmetry is conserved.

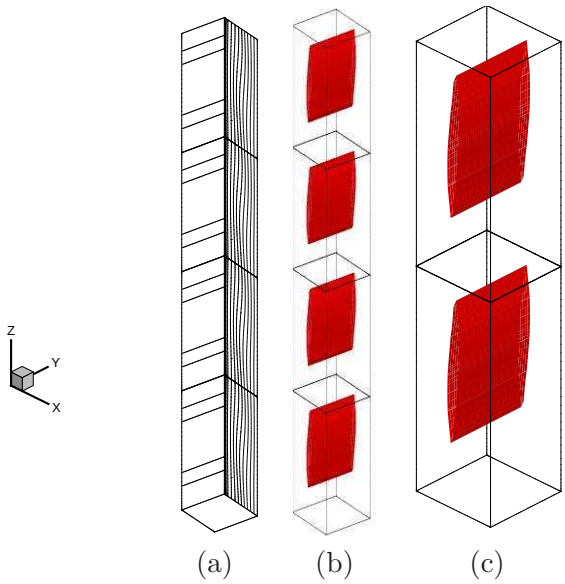

Figure 4.1: Flow structure at $Ra = 6000$: (a) isocontours of the temperature on the two selected vertical plates $x = 0.0245$ and $y = 0.9677$; (b) isosurface of transverse vorticity $\Omega_y = 3.1$; (c) enlargement of the upper half of the domain in (b)

4.3 Second bifurcation : 3D steady structures

When $Ra > Ra_{c2}$, the four-roll solution becomes unstable in the transverse direction, and a steady 3D pattern, shown in Figure 4.2, appears through a second bifurcation, as was also found by Nagata and Busse [31] and Clever and Busse [33]. Although the transition breaks the y-translation invariance, the invariance of the Navier-Stokes equations (Eq. 1.1-1.4) under y-translations ensures that there exists a whole circle of solutions, corresponding to an arbitrary y-translation of the pattern. Thus, this bifurcation is also a circle pitchfork bifurcation. The time evolution of the temperature measured at the point ($x = 0.0381$, $y = 0.097$, $z = 5$), located in the hot boundary layer, is plotted in Figure 4.3 (a). An enlargement of the same signal for the times $1000 < t < 1200$ is represented in logarithmic scale in Figure 4.3 (b). The temperature disturbance grows exponentially for $1000 < t < 1070$, which corresponds to the linear growth rate of the most unstable eigenmode, then increases at a lower rate for $t > 1070$ before the amplitude of perturbation satures. By using the same argument [60] as that used in the previous chapter, this evolution shows that the coefficient of the cubic term in the normal form of the circle pitchfork bifurcation is negative, therefore this bifurcation is supercritical.

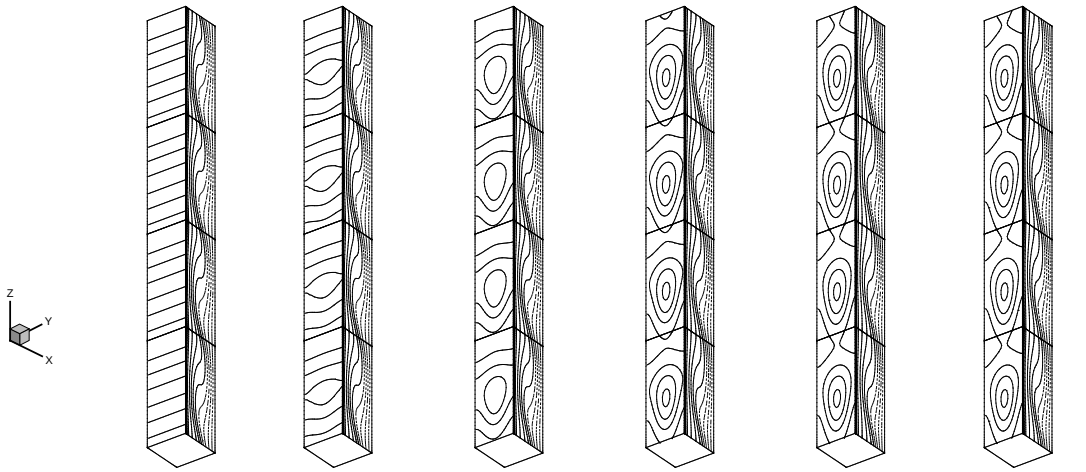

(a) t=500 (b) t=1040 (c) t=1090 (d) t=1120 (e) t=1170 (f) t=2000

Figure 4.2: Flow structure at $Ra = 11000$: (a)-(f): temperature isocontours on the two planes $x = 0.0245$ (next to the hot wall) and $y = 0.9677$ (perpendicular to side-walls) at times as indicated.

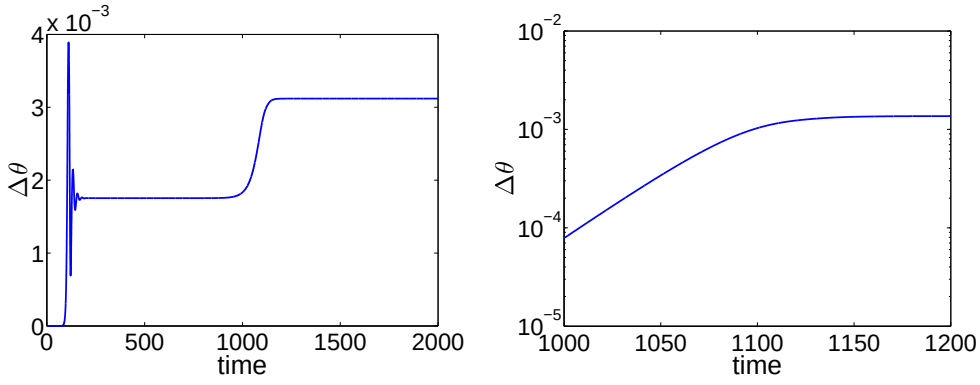

(a) (b)

Figure 4.3: (a): Time series of temperature perturbation $\Delta\theta$ with respect to the base flow at the point (0.0381, 0.097, 5) in the boundary layer near the hot wall at $Ra = 11000$; (b): An enlargement of (a) for $1000 < t < 2000$ on logarithmic scale.

The threshold Ra_{c2} can be obtained by linearizing the equations of motion around the 2D steady solution and integrating a small perturbation in time for different values of Ra. The growth rate of these perturbations, which is equal to the most unstable eigenvalue, is plotted in Figure 4.4 and is found to increase quasi-linearly with Ra. The critical Rayleigh number Ra_{c2} obtained by linear extrapolation of the plot is around 9980.

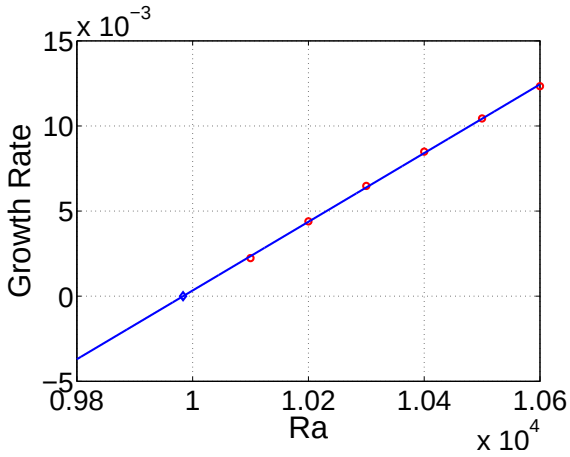

Figure 4.4: Perturbation growth rate as a function of Ra. By linear extrapolation, the Ra_{c2} is estimated around 9980.

The steady 3D solution retains some of the symmetries of the 2D solutions, namely the reflection in y and translation by $A_z/4$ in z, but the translation symmetry in y and the centro-Boussinesq symmetry are replaced with the single discrete symmetry

$$(x, y, z, T) \to (1 - x, y + 0.5, A_z - z, -T) \tag{4.1}$$

The 2D solution, which was $O(2) \times D_4$ symmetric, has bifurcated to a 3D solution with $D_1 \times D_4$ symmetry.

This can be seen in Figure 4.5, which shows temperature contours and streamlines on three planes parallel to the plates. The field obeys the symmetry (Eq. 4.1), as can be seen by comparing Figure 4.5 (a) with (c) or else Figure 4.5 (d) with (f). The upwind motion on the plane $x = 0.0381$ along the hot wall (Figure 4.5 (d)) and the downwind motion on the plane $x = 0.9619$ along the cold wall (Figure 4.5 (f)) are symmetrical. On the mid-plane, the streamline plot of Figure 4.5 (e) shows two large and two small secondary counter-rotating

vortices.

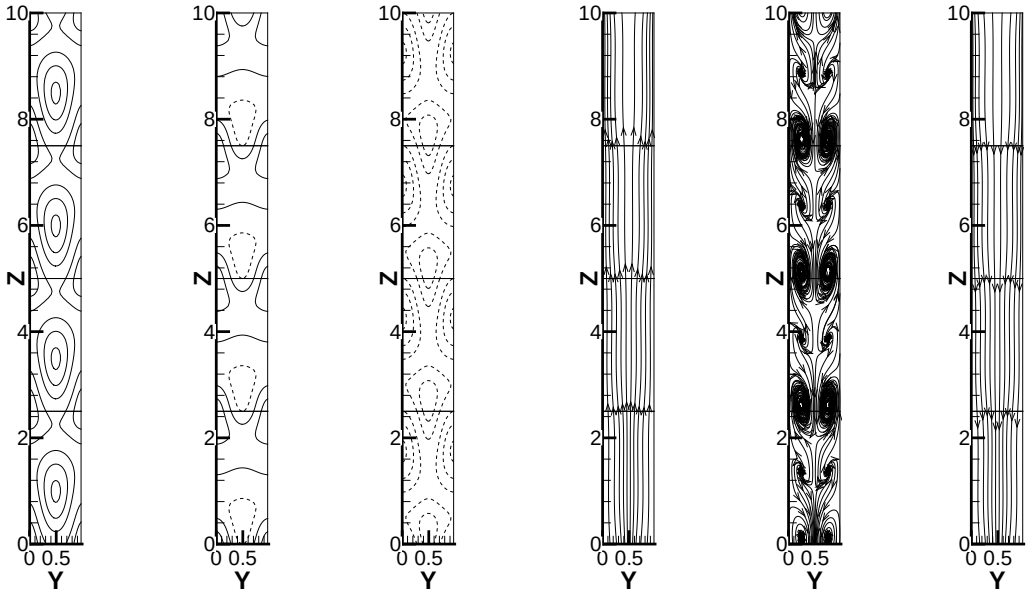

(a) $x = 0.038$ (b) $x = 0.5$ (c) $x = 0.962$ (d) $x = 0.038$ (e) $x = 0.5$ (f) $x = 0.962$

Figure 4.5: (a-c) Temperature isocontours on the vertical mid-plane $x = 0.5$ and on other two planes which are symmetric with respect to the plane ($x = 0.5$); (c) Streamlines on the same three vertical planes at $Ra = 11000$.

Since the flow is invariant under translation by $A_z/4$, we restrict our analysis to the upper half of the domain in the rest of this section.

Figure 4.6 shows isosurfaces of the vorticity components Ω_y, Ω_x, Ω_z along with the Q-criterion [61]. The Q-criterion is defined as

$$Q = \frac{1}{2}(\Omega_i\Omega_i - E_{ij}E_{ij})$$

where E_{ij} is the rate of strain tensor $\frac{1}{2}(\frac{\partial u_i}{\partial x_j} + \frac{\partial u_j}{\partial x_i})$. Therefore it provides a measure of the vortices. Comparison of Figures 4.6 (a) and (d) shows that most of the vorticity is transverse and is organized into the corotating convection rolls corresponding to the most linearly unstable mode.

Examination of the horizontal vorticity (Ω_x) plots in Figure 4.6 (b) confirms that the flow is characterized by two counter-rotating vortices, which are inclined 45 degrees with respect to both the horizontal and the vertical planes. As shown in Figure 4.6 (d), these secondary

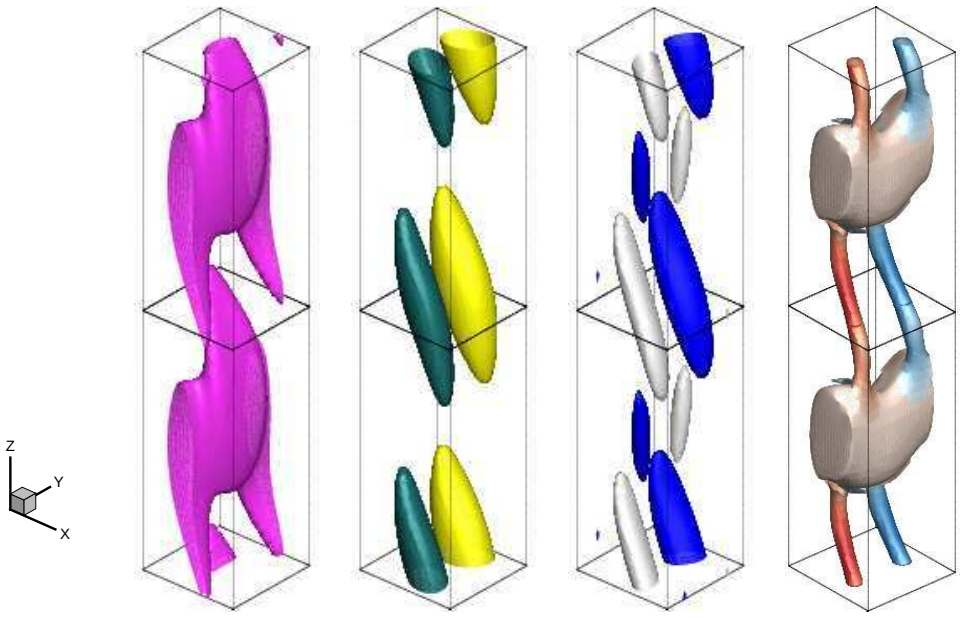

(a) $\Omega_y = 3$ (b) $\Omega_x = \pm 1$ (c) $\Omega_z = \pm 0.5$ (d) $Q = 0.12$

Figure 4.6: Vorticity isosurfaces at $Ra = 11000$.

circulations link the primary rolls and are to some extent reminiscent of the three-dimensional braids connecting the primary vortices observed in shear layers before vortex pairings [62]. In addition, Figure 4.6 (c) shows the presence of additional counter-rotating vortices within the primary convection rolls. These vortices are about half the height of the larger secondary vortices, and their orientation is opposite to that of the larger secondary vortices. They are predominantly aligned with the vertical direction z.

In summary, the flow structure for the 3D pattern consists of: (1) primary transverse corotating rolls predominantly aligned in the direction y, (2) large secondary counter-rotating vortices or braids linking up the primary rolls, which are inclined about 45 degrees with respect to both the horizontal and the vertical planes, (3) two vertical, short counter-rotating vortices located within each primary rolls.

4.4 Third Bifurcation: 3D Time-Periodic Flow

The 3D pattern remains stable up to a value of $Ra < Ra_{c3} = 11270$. For $Ra_{c3} < Ra < 12000$, the 3D pattern becomes time-dependent.

4.4.1 Local analysis

The time series of the temperature at a point located in the hot boundary layer is plotted in Figure 4.7 (a). Figure 4.7 (b) shows that it corresponds to a periodic signal of frequency $f_1 = 0.036$, very close to the basic frequency $f_1^{2D} = 0.032$ found in the 2D simulations at a slightly higher Rayleigh number.

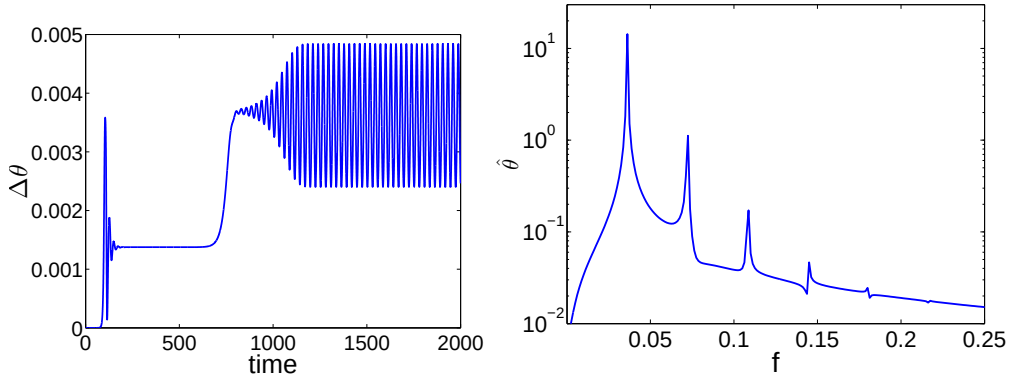

(a) (b)

Figure 4.7: (a): Time series of temperature at the point (0.0381, 0.097, 5) in the boundary layer near the hot wall, $Ra = 11500$ (b): Temporal Fourier spectrum of the periodic portion $t \in [1200, 2000]$ of the signal (a).

During this periodic regime, we observe that the oscillation frequency f_1 is nearly constant as the Rayleigh number increases above its bifurcation value, while the square of the oscillation amplitude increases linearly with Ra as shown in Figure 4.8. This is consistent with a Hopf bifurcation. The critical Rayleigh number Ra_{c3} evaluated by the linear extrapolation of the oscillation amplitude as a function of Ra is around $Ra_{c3} = 11270$.

4.4.2 Global enstrophy budgets

Some insight into the dynamics of the flow can be given by enstrophy, which gives a measure of rotational effects in the flow. The total contribution to the enstrophy of each vorticity component $[\int_V \Omega_j^2 dV]^{1/2}$ was computed, where $j = x, y, z$ and Ω_j is the j-th component of the vorticity vector. As we can see from Figure 4.9, most of the enstrophy is contained in the transverse contribution $[\int_V \Omega_y^2 dV]^{\frac{1}{2}}$. Both the horizontal and vertical contributions oscillate

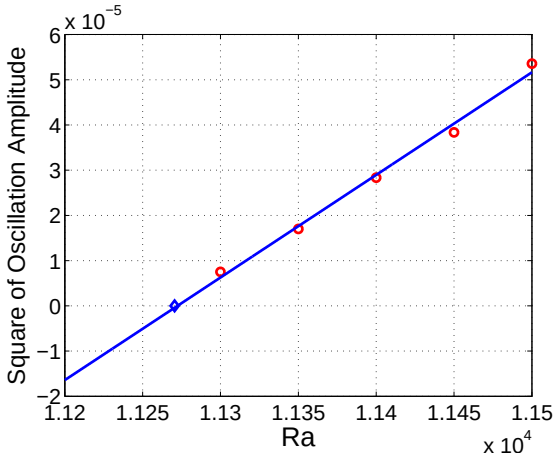

Figure 4.8: Square of temperature oscillation amplitude at the point (0.0381, 0.097, 5) in the boundary layer near the hot wall as a function of Ra. By linear extrapolation, Ra_{3c} is estimated as around 11270.

essentially in phase opposition with the transverse contribution.

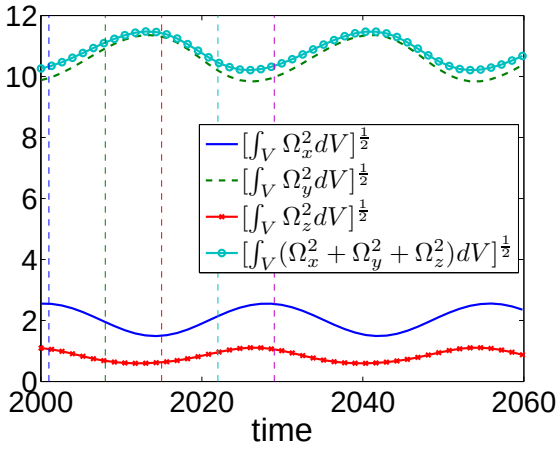

Figure 4.9: Temporal evolution of horizontal vorticity intensity $[\int_V \Omega_x^2 dV]^{\frac{1}{2}}$, transverse vorticity intensity $[\int_V \Omega_y^2 dV]^{\frac{1}{2}}$, and vertical vorticity intensity $[\int_V \Omega_z^2 dV]^{\frac{1}{2}}$ at $Ra = 11500$.

A physical interpretation of this plot is given in Figure 4.10. The flow structures are similar to the steady ones observed in the previous regime, (and therefore retain the same spatial symmetry), but they now pulse periodically. When the primary rolls are strongest, the secondary vortices disappear. At this moment, the flow is mostly two-dimensional (Figure 4.10 (c)). In contrast, when the secondary vortices reach their maximum intensities, the primary rolls bend in the transverse direction: the strongly 3D flow can be seen in Figure 4.10 (a) and (e).

We note that the frequency f of the oscillation is very close to the natural frequency of

the mixing layer $f_n \sim 0.032$ [62], when it is nondimensionalized with the distance between the plates and the maximum velocity difference observed in the base flow.

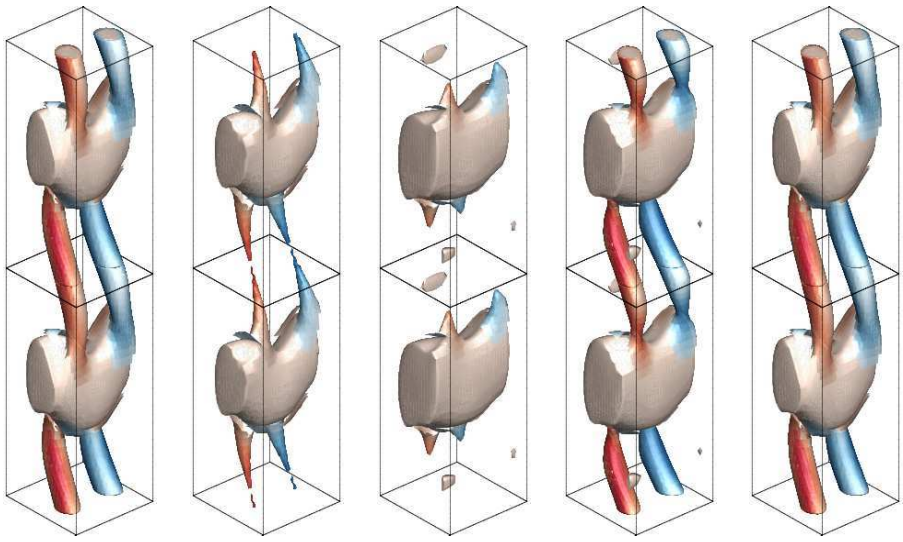

(a) $t = 2001$ (b) $t = 2008$ (c) $t = 2015$ (d) $t = 2022$ (e) $t = 2029$

Figure 4.10: Q-criterion isosurface $Q = 0.12$ at selected times (corresponding vertical lines in Figure 4.9) spanning one temporal oscillation, $Ra = 11500$. Isosurfaces are colored by Ω_z.

To better understand the origin of the oscillations, we consider the vorticity equation:

$$\frac{\partial \Omega_i}{\partial t} + u_j \frac{\partial \Omega_i}{\partial x_j} - \Omega_j \frac{\partial u_i}{\partial x_j} = \frac{Pr}{\sqrt{Ra}} \frac{\partial^2 \Omega_i}{\partial x_j \partial x_j} - Pr \varepsilon_{ijk} \frac{\partial \theta \delta_{j3}}{\partial x_k} \tag{4.2}$$

If we multiply equation (4.2) by $2\Omega_i$, we obtain

$$\frac{\partial \Omega_i^2}{\partial t} + u_j \frac{\partial \Omega_i^2}{\partial x_j} = 2\Omega_i \Omega_j \frac{\partial u_i}{\partial x_j} + 2\frac{Pr}{\sqrt{Ra}} \Omega_i \frac{\partial^2 \Omega_i}{\partial x_j \partial x_j} - 2\Omega_i Pr \varepsilon_{ijk} \frac{\partial \theta \delta_{j3}}{\partial x_k}. \tag{4.3}$$

(We sum over j and k, but not over i, ε is the permutation symbol and δ is the Kronecker symbol). The terms on the right-hand side of the equations correspond to the production - or destruction - of Ω_i^2 through three different mechanisms: (i) vortex stretching, which is tilting and stretching of vorticity components by the velocity field (ii) friction, i.e the action of viscosity (which we will also refer to as diffusion) and (iii) buoyancy. Summing over i (i.e using the tensor notation for i) yields the enstrophy equation. We choose instead to integrate the equation corresponding to each component over the whole domain. One can check that

the transport term (second term on the left-hand side) disappears, so that we are left with the following equations for each vorticity component:

$$\begin{bmatrix} \int_V \frac{\partial \Omega_x^2}{\partial t} dV \\ \int_V \frac{\partial \Omega_y^2}{\partial t} dV \\ \int_V \frac{\partial \Omega_z^2}{\partial t} dV \end{bmatrix} = \begin{bmatrix} \int_V (2\Omega_x (\overrightarrow{\Omega} \cdot \nabla u) + 2\frac{Pr}{\sqrt{Ra}} \Omega_x \nabla^2 \Omega_x + 2Pr\Omega_x \frac{\partial \theta}{\partial y}) dV \\ \int_V (2\Omega_y (\overrightarrow{\Omega} \cdot \nabla v) + 2\frac{Pr}{\sqrt{Ra}} \Omega_y \nabla^2 \Omega_y - 2Pr\Omega_y \frac{\partial \theta}{\partial x}) dV \\ \int_V (2\Omega_z (\overrightarrow{\Omega} \cdot \nabla w) + 2\frac{Pr}{\sqrt{Ra}} \Omega_z \nabla^2 \Omega_z) dV \end{bmatrix} \tag{4.4}$$

Figures 4.11 to 4.16 present the global evolution and spatial distribution of the three terms on the right-hand side of equation (39) for each vorticity component. The balance in the horizontal direction x can be seen in Figure 4.11. The vortex stretching term and the buoyancy term are both source terms and oscillate with a small phase shift, while the friction term is negative and oscillates in phase opposition with the other two contributions. As the intensity of the friction is not quite compensated by the effect of vortex stretching and buoyancy, this results in limited oscillations of the horizontal vorticity r.m.s $[\int_V \Omega_x^2 dV]^{\frac{1}{2}}$. The spatial distribution of the contributions due to vortex stretching, viscous effects, and buoyancy is represented in Figure 4.12 (a)-(c) on a plane orthogonal to the plates. The plane was chosen in order to provide a relevant cross-section of one of the vorticity braids, i.e. the secondary counter-rotating vortices. The vortex stretching and buoyancy terms are both positive everywhere (Figure 4.12 (a) and (c)), while the friction term is negative (Figure 4.12 (b)). All terms reach their maximum over the portion of space occupied by the counter-rotating vortices.

Figure 4.13 represents the different contributions to equation (4.4) for the transverse component. All three terms oscillate essentially in phase (with phase shifts of about 1/8 and 1/12 of the time period), which is responsible for the strong oscillation observed in the principal rolls. The vortex stretching term is always positive, as can be expected. Perhaps a more surprising result is that friction is now a source term for the transverse vorticity, while buoyancy constitutes a sink for it. Since the temperature gradient is always negative and the principal rolls are associated with positive transverse vorticity Ω_y, one would expect a positive value for $-2Pr\Omega_y \frac{\partial \theta}{\partial x}$. To understand this discrepancy, we examined the spatial distribution of the different contributions, which can be seen in Figure 4.14 (a)-(c) for the symmetry plane $y = 0.5$.

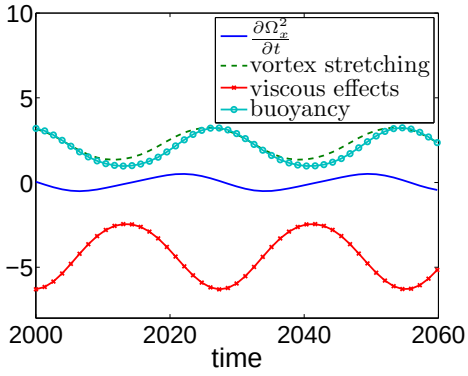

Figure 4.11: Temporal evolution of the different terms in equation (4.4) for x-component: time-derivative of the horizontal vorticity $\int_V \frac{\partial \Omega_x^2}{\partial t} dV$, vortex-stretching contribution $\int_V 2\Omega_x(\overrightarrow{\Omega} \cdot \nabla u)dV$, friction effects $\int_V 2\frac{Pr}{\sqrt{Ra}}\Omega_x \nabla^2 \Omega_x dV$ and buoyancy contribution $\int_V 2Pr\Omega_x \frac{\partial \theta}{\partial y} dV$, $Ra = 11500$.

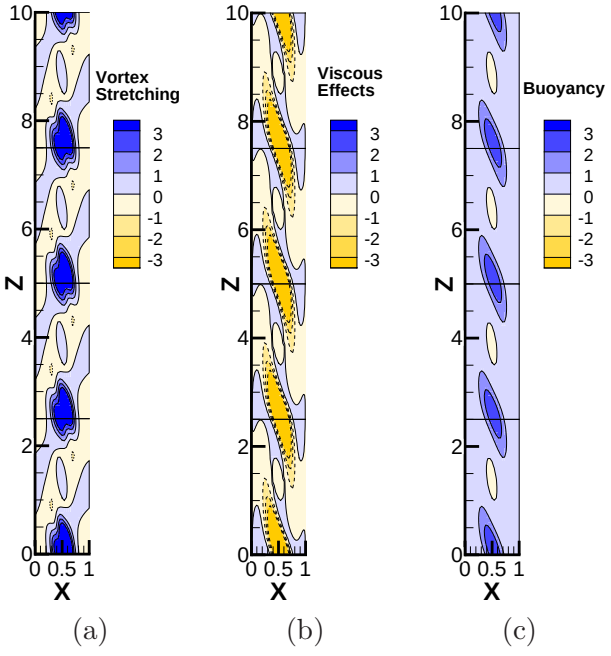

Figure 4.12: Spatial distribution of (a) the vortex stretching contribution $2\Omega_x(\overrightarrow{\Omega} \cdot \nabla u)$, (b) the friction contribution $\frac{Pr}{\sqrt{Ra}}\Omega_x \nabla^2 \Omega_x$, and (c) the buoyancy contribution $2Pr\Omega_x \frac{\partial \theta}{\partial y}$ on the vertical plane $y = 0.2903$ at $t = 2000$, $Ra = 11500$.

The effect of vortex stretching was essentially positive, as could be expected (Figure 4.14 (a)). Over the portion of space covered by the principal vortices, the contribution of the buoyancy was also found to be positive (Figure 4.14 (c)), but strongly negative values were observed very close to the wall in the boundary layer, which is where the temperature gradient is significant. The situation was reversed for friction effects: strongly positive values were found very close to the walls. This reflects the fact that transverse vorticity is indeed generated at the walls through friction, while buoyancy works against the velocity gradient in the wall layer.

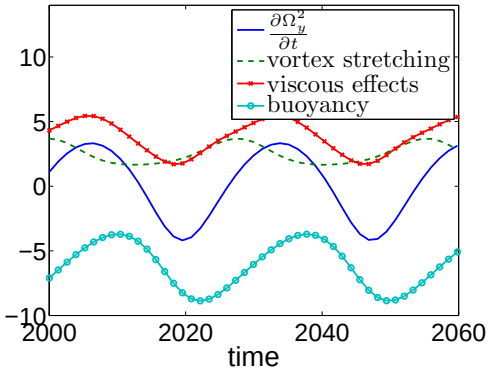

Figure 4.13: Temporal evolution of the different terms in equation (4.4) for y-component: time-derivative of the transverse vorticity $\int_V \frac{\partial \Omega_y^2}{\partial t} dV$, vortex-stretching contribution $\int_V 2\Omega_y(\overrightarrow{\Omega} \cdot \nabla v) dV$, friction effects $\int_V 2\frac{Pr}{\sqrt{Ra}}\Omega_y \nabla^2 \Omega_y dV$ and buoyancy contribution $\int_V -2Pr\Omega_y \frac{\partial \theta}{\partial x} dV$, $Ra = 11500$.

Figure 4.15 represents the relative contributions of vortex stretching and friction to the oscillations of the vertical component of the enstrophy. These oscillations are limited, since the positive effect of vortex stretching is almost exactly compensated by frictional effects (buoyancy does not appear in the equations). As can be seen in Figure 4.16 (a) and (b), both friction and vortex stretching contributions are maximal at the location of the counter-rotating vortices.

4.5 3D Subsequent bifurcations

4.5.1 Period-doubling bifurcations

When $12100 \leq Ra \leq 12200$, the temporal evolution of the 3D pattern becomes more complex. At $Ra = 12200$, the time series of the temperature at a point located in the boundary layer

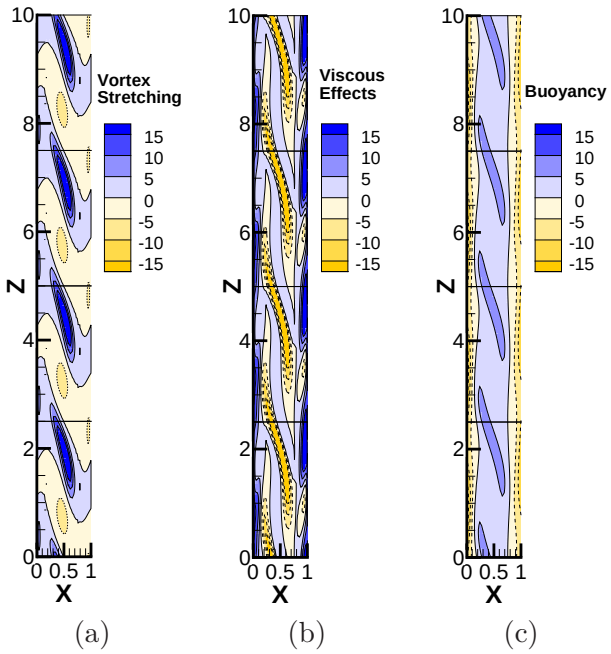

Figure 4.14: Spatial distribution of (a) the vortex stretching contribution $2\Omega_y(\overrightarrow{\Omega}\cdot\nabla v)$, (b) the friction effects $\frac{Pr}{\sqrt{Ra}}\Omega_y\nabla^2\Omega_y$, and (c) the buoyancy contribution $-2Pr\Omega_y\frac{\partial\theta}{\partial x}$ on the vertical plane $y = 0.5$ at $t = 2000$, $Ra = 11500$.

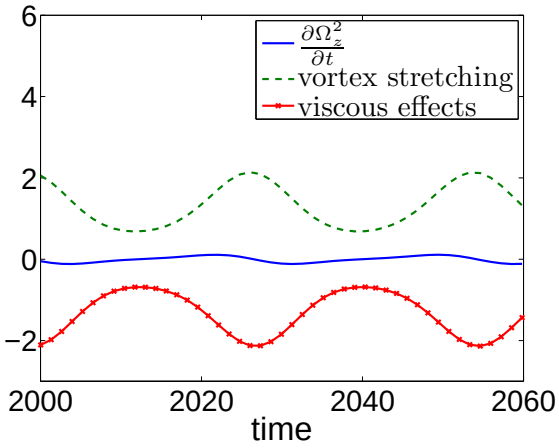

Figure 4.15: Temporal evolution of the different terms in equation (4.4) for z-component: time-derivative of the vertical vorticity $\int_V \frac{\partial\Omega_z^2}{\partial t}dV$, vortex-stretching contribution $\int_V 2\Omega_z(\overrightarrow{\Omega}\cdot\nabla w)dV$, friction effects $\int_V 2\frac{Pr}{\sqrt{Ra}}\Omega_z\nabla^2\Omega_z dV$, $Ra = 11500$.

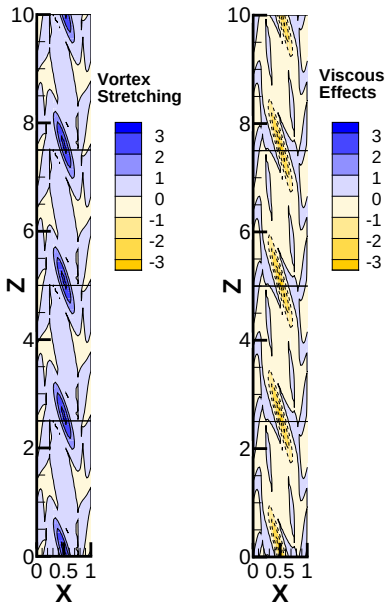

Figure 4.16: Spatial distributions of (a) the vortex stretching contribution $2\Omega_z(\overrightarrow{\Omega} \cdot \nabla w)$, (b) the friction contribution $\frac{Pr}{\sqrt{Ra}}\Omega_z \nabla^2 \Omega_z$, at the vertical plane $y = 0.2903$ (same as in Figure 4.12) at $t = 2000$, $Ra = 11500$.

presents subharmonic oscillations for $t \in [800, 2200]$ before becoming quite irregular, as shown in Figure 4.17(a). The Fourier spectrum of the temperature (Figure 4.17(b)) shows that the largest amplitude is located at the frequency $f_1 = 0.035$, which is close to the frequency identified in the previous periodic regime at a slightly lower Rayleigh number (see section 4.4.1), while the second largest amplitude corresponds to the frequency $f_{1/2} = 0.0175 = f_1/2$.

The topology of the flow consists of four 3D structures which are similar to those found in the monoperiodic regime at $Ra = 11500$ (section 4.4.1). The intensities of the transverse rolls and that of the braids oscillate out of phase, with a temporal modulation equal to twice the basic period.

As Ra increases, we observe for $A_z = 10$ a succession of period-doubling bifurcations illustrated by phase portraits in Figure 4.18. At $Ra = 11500$, the singly periodic regime is characterized by one cycle in the phase portrait (Figure 4.18(a)). For $Ra \in [12100, 12200]$, a period-2 cycle is observed (Figure 4.18(b)). At $Ra = 12300$, we observe a 4-cycle in the phase portraits and then at $Ra = 12310$ an 8-cycle, at $Ra = 12315$ a 16-cycle (Figures 4.18(c,d,e)),

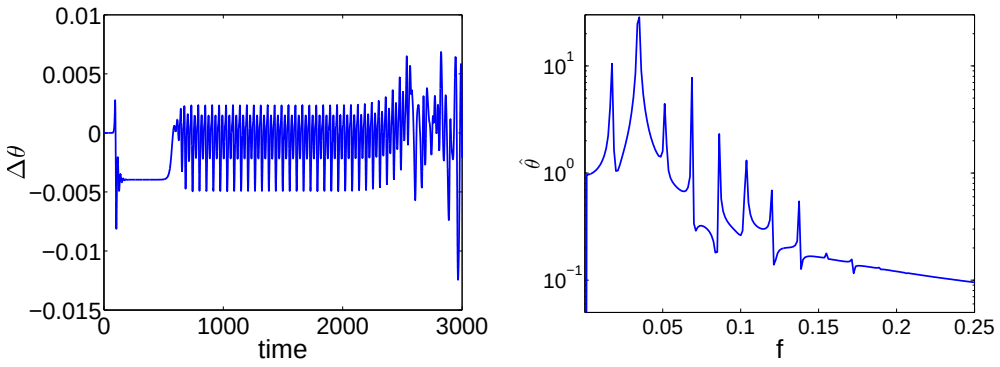

(a) (b)

Figure 4.17: (a): Time series of temperature at the point (0.0381, 0.097, 5) in the boundary layer near the hot wall, $Ra = 12200$, $A_z = 10$. (b): Temporal Fourier spectrum of the subharmonic portion in the time interval $t \in [1200, 2000]$.

etc. Similar sequences of period-doubling bifurcations have been observed in the experimental transition to chaos in Rayleigh-Bénard convection. Maurer and Libchaber [37] observed the appearance of a first frequency f_1', followed by a second frequency f_2'. For higher values of the Rayleigh number, phase locking between the frequencies was observed. The transition to turbulence was then triggered by the generation of the frequencies $f_2'/2$, $f_2'/4$, and so forth. A similar scenario was found in the experiments of Giglio, Musazzi and Perini [38], where a reproducible sequence of period-doubling bifurcations up to $f_1'/16$ was observed.

4.5.2 Development of a spatial instability

For $Ra \geq 12200$, we observed irregular oscillations in Figure 4.17 for large times $t > 2200$. This corresponds to a drastic change in the spatial organization of the flow, as shown in Figure 4.19. One of the structures is weakened, then disappears so that at large times $t > 2200$, the pattern observed typically consists of three structures, as can be seen in Figures 4.19(b,c,f). However four structures can still be found intermittently (Figures 4.19(a,d,e)).

$\hat{\theta}(i_x, i_z)$ represents the 2D Fourier spectrum of the temperature distribution on the vertical plane $y = 0.5$. The spatial organization of the flow can be described by the mode $\hat{T}(0, i_z)$, where 0 represents the mode 0 (mean value) in the x-direction. The temporal evolution of the spectral coefficients $|\hat{\theta}(0, i_z)|^2$ for the modes $i_z = 3, 4$ is shown in Figure 4.20 (a,b). The mode $i_z = 4$

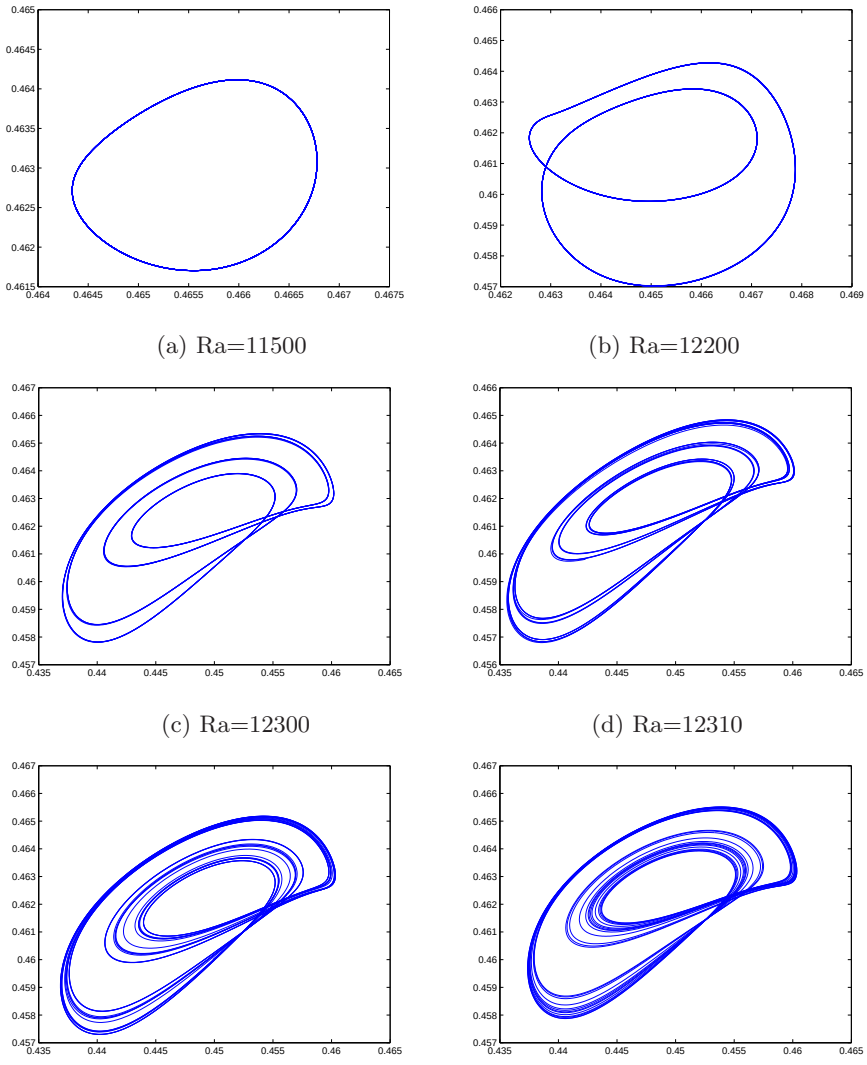

(a) Ra=11500 (b) Ra=12200

(c) Ra=12300 (d) Ra=12310

(e) Ra=12315 (f) Ra=12320

Figure 4.18: Phase portraits at different Ra, $A_z = 10$. Abscissa: temperature measured at the point (0.038, 0.097, 6.98); ordinate: temperature measured at the point (0.038, 0.903, 6.54).

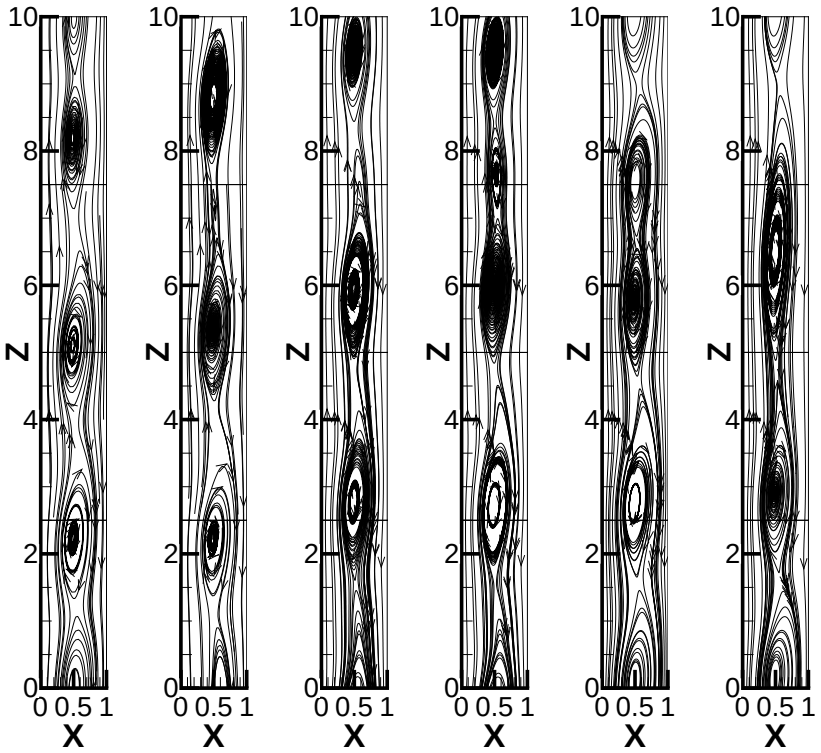

Figure 4.19: Flow streamlines on the plane $y = 0$ at $Ra = 12200$ for different times: (a) $t = 2905$; (b) $t = 2920$; (c) $t = 5900$; (d) $t = 5910$; (e) $t = 5960$; (f) $t = 5970$.

dominates when $700 < t < 2000$, then for $t \in [4000, 6000]$ the mode $i_z = 3$ dominates for most of the time, except around the times $t \sim 5040$ and $t \sim 5950$, where the mode $i_z = 4$ becomes dominant again. Due to the long integration times, we were not able to determine whether the spatial intermittency was a transient or a persistent feature of the flow.

A simulation was performed at $Ra = 12000$ from an initial condition consisting of an instantaneous field at $Ra = 12200$ characterized by a three-structure pattern. The flow settled down to a periodic pulsation of three structures. The presence of hysteresis confirms that the spatial wavenumber modulation instability is subcritical, and supports the conjecture that the wavenumber competition between the mode 4 and mode 3 is similar to a subcritical Eckhaus instability.

Beyond $Ra = 13000$, for $A_z = 10$, it is no longer possible to identify a discrete set of frequencies, and the flow rapidly becomes temporally chaotic. When Ra is increased to $Ra = 15000$, the whole domain is still dominated by three structures, but patterns of two or four structures can also be observed, as evidenced in Figure 4.20 (c,d) by the evolution of the temperature spectral density $|\hat{\theta}(0, i_z)|^2$ for different wavenumbers.

4.6 Influence of flow structures on global heat transfer

A measure of the global heat transfer is given by the Nusselt number, which is defined as the ratio between the total and diffusive heat transfer. In our simulations, the Nusselt number is calculated as $Nu = \iint -\dfrac{\partial \langle \tilde{\theta} \rangle}{\partial x} dydz|_{wall}$, since the velocity of the flow at the walls is zero, where $\langle \cdot \rangle$ denotes the time-averaging of a variable. Its dependence with respect to the Rayleigh number Ra is plotted in Figure 4.21.

In the 2D steady regime, we find that $Nu \sim 0.0867 Ra^{0.25}$ which is consistent with the convective (boundary layer) regime. This estimate actually holds slightly beyond the second supercritical pitchfork bifurcation, where the 2D rolls become more intense and distorted in the transversal direction (this stage is labeled as "quasi-2D structures" in Figure 4.21). However, at $Ra = 10500$, the flow becomes three-dimensional through the creation of secondary vortices, and the Nusselt number experiences a small decrease, which is in agreement with the results of

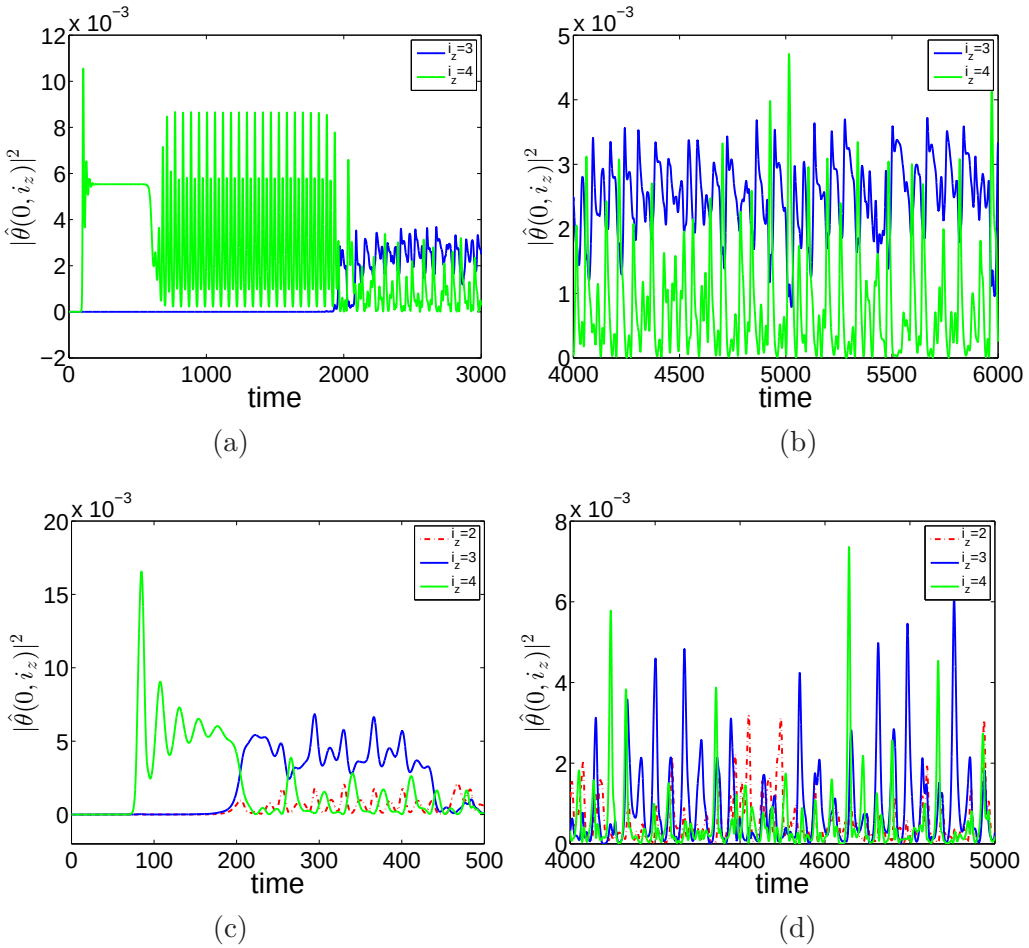

Figure 4.20: Temporal evolution of the spectral coefficients $|\hat{\theta}(0,i_z)|^2$ on the mid-plane $y = 0.5$ for selected modes k: (a) (b) $Ra = 12300$, modes $i_z = 3, 4$ (a) $t \in [0, 3000]$ (b) $t \in [4000, 6000]$. (c) (d) $Ra = 15000$, modes $i_z = 2, 3, 4$ (c) $t \in [0, 500]$ (d) $t \in [4000, 5000]$.

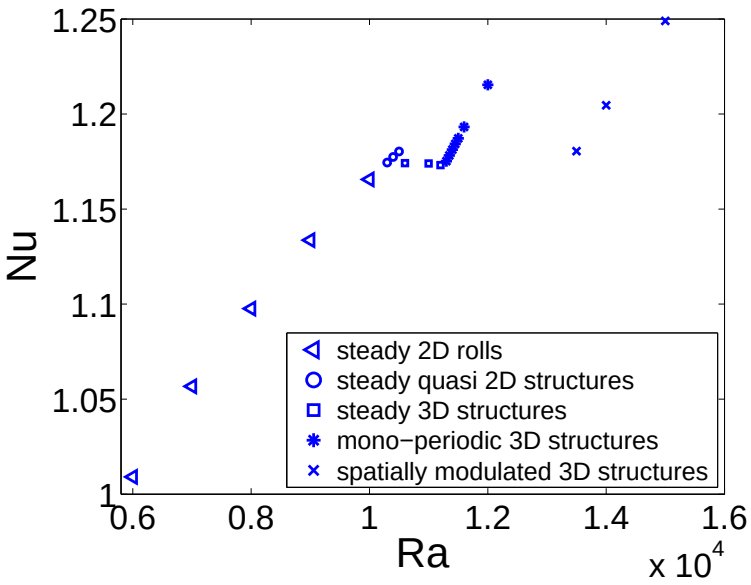

Figure 4.21: The Nusselt number Nu (averaged over vertical planes and time) as a function of Ra for $A_z = 10$

Clever and Busse [33]. It then remains approximately constant over the 3D steady regime from $Ra = 10500$ and $Ra = 10600$. At the onset of the oscillatory regimes, the Nusselt number begins to increase and continues doing so over the sequence of period-doubling bifurcations. After a sharp decrease observed at the onset of the Eckhaus-like instability, the Nusselt number starts increasing again. The maximum heat transfer increases over the range of Rayleigh numbers $Ra < 15000$ is about 20%, which agrees with Wright *et al.* [30]'s results.

4.7 Comparaison with high aspect ratio cavities

We note that the spatial characteristics of Wright *et al.*'s [30] "secondary cells" match those of what we call primary rolls. Furthermore, their general description of the route to turbulence seems to agree loosely with ours, as their flow becomes three-dimensional and then chaotic at a Rayleigh number of 13600, which is close to our observations. However, two discrepancies are observed: (i) unlike our stationary rolls, their cells appear to drift in the vertical direction from the onset of the first instability, which could be due to (horizontal) end effects of the cavity; (ii) as the Rayleigh number increases, the motion of the cells is intensified, and merging between

the cells occurred, whereas no vortex pairing was observed in our simulation. This difference could be the consequence of the relatively small dimensions of our numerical domain.

3D DNS were also carried in our group [63], in the configuration of high aspect ratio cavity with small transverse dimension $A_y = 1$ and $A_z = 20$. Adiabatic condition is imposed for the horizontal walls at the top and the bottom of the cavity, and periodic condition is kept in the transverse direction y. The base flow first bifurcates to steady 2D rolls and then to a steady 3D state, where the 3D structures identified as the primary rolls connected with counter-rotating vortices/braids are still present, but only in the center of high aspect ratio cavity. The flow becomes time-dependent at $Ra = 15000$ and eventually enters the temporally chaotic regime, when Ra is further increased. However, no period-doubling bifurcation was observed. The number of localized 3D structures decreases as Ra increases. Instead of staying at the same location, the oscillatory 3D structures drift vertically and invade occasionally the top and bottom of the cavity at $Ra = 25000$.

4.8 Conclusion

In 3D simulations, the first instability is a supercritical pitchfork bifurcation at $Ra_c = 5708$, through which the co-rotating rolls are formed. The second bifurcation is observed at a Rayleigh number of $Ra_{c2} \sim 9980$. The 2D rolls become unstable through another supercritical pitchfork bifurcation to a steady 3D pattern, characterized by secondary counter-rotating vortices connecting the principal convection rolls. When the Rayleigh number is further increased to $Ra_{c3} \sim 11270$, the steady 3D pattern becomes oscillatory through a Hopf bifurcation, as the intensities of the transverse rolls and the counter-rotating vortices oscillate in phase opposition. A sequence of period-doubling bifurcations is then observed at higher Rayleigh numbers. In the case $A_z = 10$, the sequence of period-doubling bifurcations is only a transient feature. The multiply-periodic flow gives way to complex spatio-temporal dynamics when $Ra \geq 12100$ and a competition between different vertical wavelengths is rapidly apparent in the flow pattern. The global behavior of heat transfer is established up to $Ra = 15000$, where Nu generally increases with Ra by 25% at most, with discontinuities as the flow goes through various bifurcations.

Table 4.1: Summary of bifurcations and associated flow structures and symmetries for 3D simulations, $A_y = 1$, $A_z = 10$, $T = 1/f_1$.

Ra	Nature of Bifurcation	Flow Structures Number of Structures	Spatial Symmetry Temporal Symmetry
$Ra < Ra_c = 5708$		1D base flow	$O(2) \times O(2)$ steady
$Ra_c < Ra < 9980$	supercritical circle pitchfork	2D corotating rolls $n = 4$	$O(2) \times D_4$ steady
$9980 < Ra < 11270$	supercritical circle pitchfork	3D structures $n = 4$	$D_1 \times D_4$ steady
$11270 < Ra \leq 12000$	supercritical Hopf	3D structures $n = 4$	$D_1 \times D_4$ T-periodic
$Ra \geq 12100$	period-doubling	3D structures $n = 4$	$D_1 \times D_4$ 2^nT-periodic
	subcritical Eckhaus--like instability	3D structures $n = 3$	no symmetry

The results about the sequence of bifurcations and associated symmetries are summarized in Table 4.1.

Comparison of 2D and 3D results confirms that transverse effects are essential for the development of instabilities and the onset of chaos. This result is of interest, as in many situations involving thermal convection, the first step towards making a problem tractable is to reduce it to a two-dimensional geometry. An important point is that the competition between vertical and transverse pattern modulations is expected to be altered as the dimensions of the plate vary.

In the next chapter, we study a domain limited to one vertical wavelength, where the competition between vertical patterns is suppressed and chaos arises through the sequence of period-doubling bifurcations.

Chapter 5

3D Minimal Flow Unit $A_z = 2.5$ & $A_y = 1$

5.1 Introduction

In this chapter, we study the transition to chaos of the flow in the configuration of Minimal Flow Unit (MFU). The concept of the Minimal Flow Unit was first introduced in turbulence [64] and recently used to study the transition to chaos of plane Couette flow [65]. The MFU configuration contains only one roll in the vertical direction and its transverse dimension is constrained as well.

In the previous chapter, it has been observed that through the first instability, the flow becomes 2D and consists of 2D transverse steady rolls. Then the flow becomes 3D through a second supercritical pitchfork bifurcation. The flow structures observed consist of (i) primary rolls which are deformed in the transverse direction, (ii) counter-rotating vortices or "braids" linking the primary rolls and (iii) small counter-rotating vortices inside the primary rolls. Through a supercritical Hopf bifurcation, the 3D flow becomes oscillatory. The oscillation corresponds to an exchange of vorticity between rolls and braids which in turn inflate and deflate, but does not correspond to a vertical or a lateral motion of the structures. As Ra is further increased, a sequence of period-doubling bifurcations is observed for a limited range of time, but is rapidly superseded by a spatial modulation instability in the vertical direction. In this chapter we consider a restricted simulation domain which accomodates only one roll in the vertical direction. Then we can determine whether the multiply periodic regime becomes a persistent feature. In the present simulation domain, the vertical dimension is equal to $A_z = 2.5$, which is close to

the critical wavelength $\lambda_{zc} = 2.513$, and the transverse dimension is set to $A_y = 1$ as in the previous chapter. We first review the essential concepts of chaos theory. In particular, we focus on the largest Lyapunov exponent, which is an indicator of chaos. We then present nonlinear simulation results in this minimal flow unit.

5.2 Introduction to chaos

Although the exact definition of chaos is not yet well determined, chaotic behavior has been studied since the 1980s [66, 67]. It is widely accepted that chaotic behavior is characterized by the sensibility of nonlinear dynamical systems to the initial conditions: two trajectories whose initial conditions are quite close will eventually diverge after some finite time (Figure 5.1). The largest Lyapunov exponent, which measures the mean rate of divergence between the initially nearby trajectories, is considered as one of the most widely used measures of chaos. A positive value of the largest Lyapunov exponent is taken to be an indicator of chaos. A few scenarios have been proposed [36, 68] to describe the transition to chaos. These include period-doubling, quasi-periodicity, crisis, and intermittency. In this section, we will focus on the period-doubling scenario and the attractor merging crisis, which are actually observed in our simulations. We will then give the definition of the leading Lyapunov exponent and describe the numerical method to calculate it.

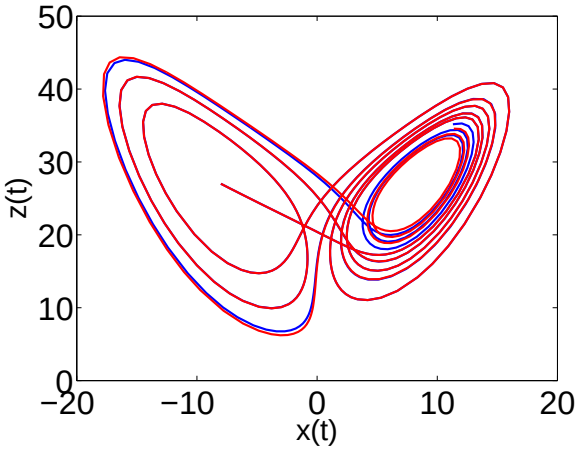

Figure 5.1: Two trajectories with nearby initial conditions diverge as time evolves in the Lorenz model.

5.2.1 Period-doubling scenario

The period-doubling scenario constitutes a feature of many nonlinear dynamical systems with one parameter. These range from one-dimensional maps, such as the logistic map [69], to ordinary differential equations representing dynamical systems of finite dimension, such as the Lorenz model [70], and partial differential systems, such as the Navier-Stokes equations, which is an infinite-dimensional dissipative nonlinear dynamical system [36]. Here, we consider two examples:

Example 1: Logistic map

The simplest system that exhibits period-doubling behavior is the logistic map:

$$x_{n+1} = r x_n (1 - x_n) \tag{5.1}$$

For $0 < r < 4$, if $x_n \in [0, 1]$, then $x_{n+1} \in [0, 1]$ as well, and the orbit remains in $[0, 1]$ for all subsequent times. For $r \neq 0$, the system has two fixed points $x = 0$ and $x = 1 - \frac{1}{r}$. For $0 < r < 1$, the fixed point $x = 0$ is stable, and $x = 1 - \frac{1}{r}$ is unstable. For $1 < r < 3$, $x = 0$ becomes unstable and $x = 1 - \frac{1}{r}$ is stable. For $3 < r < r_\infty$, a cascade of period-doubling bifurcations is observed: $r_1 = 3$ *period-2*; $r_2 = 3.449...$ *period-4*; $r_3 = 3.54409...$ *period-8*; ...; $r_\infty = 3.569946...$ *period-*∞, where r_i denotes the local critical parameter at which the i-th bifurcation occurs. It can be shown that the ratio

$$\delta = \lim_{n \to \infty} \frac{r_n - r_{n-1}}{r_{n+1} - r_n} \tag{5.2}$$

converges towards to a universal constant $\delta = 4.66920161...$, which is called the Feigenbaum number. It characterizes the route of successive period-doublings to chaos [69]. For $r_\infty < r < 4$, a mixture of chaos and order is observed. As can be seen in the bifurcation diagram (Figure 5.2), several periodic windows exist in this range of r. One example is the largest window beginning near $r = 3.83$, which contains a *period-3* cycle.

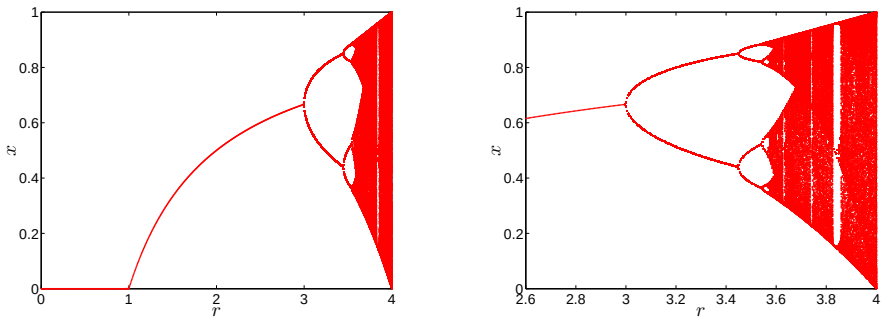

(a) $0 < r < 4$ (b) $2.6 < r < 4$

Figure 5.2: (a) Bifurcation diagram of logistic map; (b) zoom of (a) for $2.6 < r < 4$

Example 2: Lorenz equations

The Lorenz system was derived by Ed Lorenz [70] in the 1960s, when he was studying convection rolls in the atmosphere. He expanded the solution of the Navier-Stokes equations in the Boussinesq approximation using Fourier series. A drastic truncation of the solution leads to the following model consisting of only three ordinary differential equations:

$$\begin{aligned} \frac{dx}{dt} &= \sigma(y - x) \\ \frac{dy}{dt} &= rx - y - xz \\ \frac{dz}{dt} &= xy - bz \end{aligned} \tag{5.3}$$

He discovered that for certain values of the parameters, this deterministic system (5.3) could have erratic dynamics, which would today be labelled as chaotic. When $\sigma = 10$, $r = 8/3$, $b = 28$, the trajectories oscillate irregularly, although they always remain in a bounded region of phase space. The trajectories of the solutions plotted in three dimensions settle onto a complicated set, called a strange attractor, which is shown in Figure 5.1. Unlike fixed points and limit cycles, the strange attractor is not a point or a curve or a surface - it is fractal (i.e its dimension is not an integer). The fractal dimension of the Lorenz attractor is between 2 and 3. The chaotic system still exhibits some 'regularity': one example is the Lorenz map (Figure 5.3), which shows that all the local maxima of the chaotic time series $z(t)$ fall neatly on a single curve.

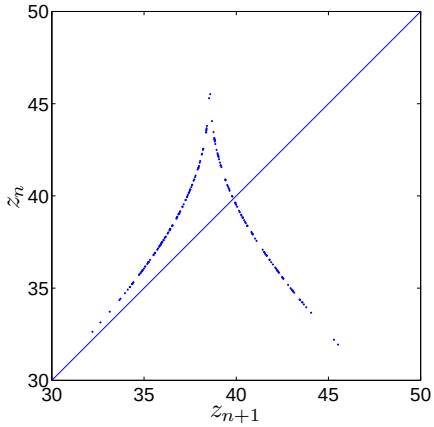

Figure 5.3: Lorenz map: z_{n+1} vs z_n

The Lorenz system has been studied extensively for several decades [67, 66, 71]. For the parameter $\sigma = 10$ and $b = \frac{8}{3}$, different dynamical behaviors are observed for different ranges of r. For example, for $r = 10$, solutions converge to a stable fixed point. For $r = 22$, a limit cycle is observed. For the interval $145 < r < 166$, the system exhibits a cascade of period-doubling bifurcations, and $r = 166.3$ it shows some intermittent chaos.

5.2.2 Attractor merging crisis and crisis-induced intermittency

Sudden changes of the chaotic attractors when control parameters are varied are called 'crises', and were first extensively studied by Grebogi *et al.* [72, 73, 68]. These crises are caused by the collision of the chaotic attractor with an unstable periodic orbit, or, equivalently, its stable manifold, or other chaotic attractors. The crises can be classified into three types [68, 67]:

- *boundary crisis*, which is characterized by the sudden destruction of a chaotic attactor, when the attractor collides the boundary of its basin or a periodic orbit.
- *interior crisis*, which is caused by the collision of the attractors with the periodic orbit in the interior of its basin. A sudden enlargement of the attractor can be observed for this kind of crisis.
- *attractor merging crisis*, when two or more attractors collide simultaneously with a periodic orbit or orbits on the basin boundary which separated them.

Suppose an attractor merging crisis of two attractors occurs when the control parameter p is varied through the critical parameter p_c. Before the crisis occuring ($p < p_c$), each of these two attractors exists, having its own basin with a basin boundary separating them. At $p = p_c$, the two attractors both simultaneously collide with this boundary. For p slightly above p_c, a trajectory typically spends a long time wandering chaotically in the region of one of the original attractors, then abruptly switches to the region of the other attractor. The times between these random switches from one region to another have a long-time exponential distribution with average $< \tau >$ which approaches infinity when p approaches p_c from above.

This crisis-induced intermittency and the Pomeau-Manneville intermittency can be schematically contrasted in the following way [68]:

- Pomeau-Manneville intermittency:

  (chaos) $\rightarrow$ (approximately periodic) $\rightarrow$ (chaos) $\rightarrow$ (approximately periodic) $\rightarrow$ ...

- Crisis-induced intermittency:

  $(\text{chaos})_1 \rightarrow (\text{chaos})_2 \rightarrow (\text{chaos})_1 \rightarrow (\text{chaos})_2 \rightarrow$ ...

For a large class of dynamical systems which exhibit crises, a power law can be found between the scaling of the characteristic transient time $< \tau >$ and the departure of the control parameter from the critical parameter $p - p_c$:

$$< \tau >= (p - p_c)^{-\gamma} \tag{5.4}$$

The quantity γ is called the critical exponent of the crises. $\gamma = \frac{1}{2}$ is a general result for crisis of one-dimensional maps with quadratic extrema, and $\gamma > \frac{1}{2}$ for higher-dimensional systems. A quantitative theory for determining the critical exponent γ of two-dimensional maps was proposed by Grebogi *et al.* [68]. The crisis is due to a tangency of the stable manifold of a periodic orbit on the basin boundary with the unstable manifold on the attractor. These types of crises appear to be very common in dissipative systems. Examples include the forced damped pendulum, the Henon map, and forced Duffing equation, etc. For such systems, the crisis occurs in one of the following two ways: *heteroclinic tangency crisis* or *homoclinic tangency crisis*.

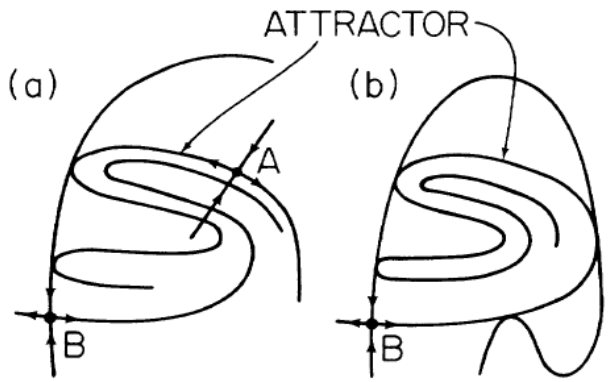

Figure 5.4: (a) Schematic illustration of heteroclinic tangencies of the stable manifold of the unstable periodic orbit B and the unstable manifold of the unstable periodic orbit A. (For simplicity the periods of A and B are taken to be 1.) (b) Schematic illustration of homoclinic tangencies of the stable and unstable manifold of the unstable periodic orbit B. Grebogi *et al.* Phys. Rev. A. 1987 [68].

In the case of a heteroclinic crisis of two-dimensional maps, we have

$$\gamma = \frac{1}{2} + \frac{ln|\alpha_1|}{|ln|\alpha_2||} \tag{5.5}$$

where α_1 and α_2 are the expanding and contracting eigenvalues of the periodic orbit.

In the case of a homoclinic crisis, we have

$$\gamma = \frac{ln|\beta_2|}{ln|\beta_1\beta_2|^2} \tag{5.6}$$

where β_1 and β_2 are the expanding and contracting eigenvalues of the periodic orbit.

In the limit of strong contraction, $\alpha_2 \to 0$ and $\beta_2 \to 0$, so that $\gamma \to \frac{1}{2}$, which is the result for a map with a quadratic maximum.

5.2.3 Lyapunov exponent

Definition

The divergence rate of nearby trajectories is a good measure of the complexity of the attractor, or its chaotic nature. This leads to the definition of the largest Lyapunov exponent. Considering a mapping $\mathbf{X} \to \mathbf{F}(\mathbf{X})$, where $\mathbf{X}$ is a vector of dimension d. After one iteration, the distance be-

tween two nearby trajectories initially separated by $\delta\mathbf{X}_0$ becomes $\delta\mathbf{X}_1 = \mathbf{J}_0(\mathbf{X}_0)\delta\mathbf{X}_0$, where $\mathbf{J}_0$ denotes the Jacobian of $\mathbf{F}$ evaluated at $\mathbf{X}_0$. With k iterations, the two trajectories diverge to a distance $\delta\mathbf{X}_k = \prod_{i=0}^{k-1}\mathbf{J}_i\delta\mathbf{X}_0$. As the Jacobian contains the contribution of relative rotation between the trajectories, the norm is instead more suitable for correctly measuring the divergence rate of two nearby trajectories. Since $|\delta\mathbf{X}_n|^2 = \delta\mathbf{X}_n^t \cdot \delta\mathbf{X}_n = \delta\mathbf{X}_0^t\mathbf{J}_0^t\cdots\mathbf{J}_{n-1}^t\mathbf{J}_{n-1}\cdots\mathbf{J}_0\delta\mathbf{X}_0$, the divergence rate η defined by $|\delta\mathbf{X}_n|^2 = \eta^{2n}|\delta\mathbf{X}_0|^2$ can be calculated as

$$\eta = \lim_{n\to\infty}\left(\frac{\delta\mathbf{X}_0^t\mathbf{J}_0^t\cdots\mathbf{J}_{n-1}^t\mathbf{J}_{n-1}\cdots\mathbf{J}_0\delta\mathbf{X}_0}{\delta\mathbf{X}_0^t\cdot\delta\mathbf{X}_0}\right)^{\frac{1}{2n}} \tag{5.7}$$

$\lambda_1 = log(\eta)$ is defined to be the largest Lyapunov exponent.

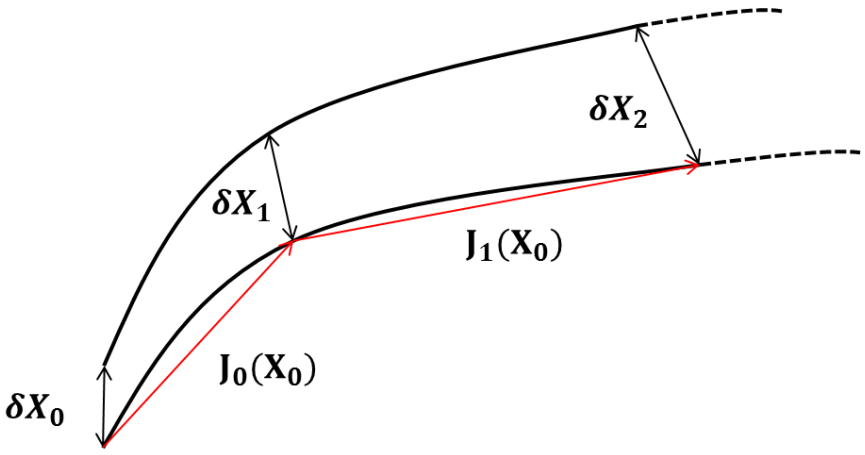

Figure 5.5: Evolution of two initially close trajectories, where $\delta\mathbf{X}_0$ and $\mathbf{J}_i$ are used for the calculation of the largest Lyapunov exponent in Eq. (5.7).

Numerical computation of largest Lyapunov exponent

A positive largest Lyapunov exponent is a widely accepted criterion of chaos. The numerical method proposed by Benettin *et al.* [74] consists in computing the expanding rate of the direction of maximum expansion and taking its logarithmic average over the orbit. The procedure is independent of the numerical method used to solve the Navier-Stokes equations. We define $\mathbf{X}(t) = [\mathbf{u}, \theta]$ as the $(4 \times N)$-dimensional array describing the state of N fluid elements as a function of time and $\delta\mathbf{X}(t) = [\delta\mathbf{u}, \delta\theta]$ is the perturbation. We evaluate the expansion rate of

the two nearby trajectories $\mathbf{X}(t)$ and $\mathbf{X}(t)+\delta\mathbf{X}(t)$, by tracking the evolution of the perturbation $\delta\mathbf{X}(t) = f(\delta\mathbf{X}(0))$. The leading Lyapunov exponent λ_1 is defined as

$$\lambda_1 = \frac{d}{dt}\lim_{t\to\infty} \ln\left(\frac{\parallel \delta\mathbf{X}(t) \parallel}{\parallel \delta\mathbf{X}(0) \parallel}\right) \tag{5.8}$$

where the norm is choosen as $\delta\mathbf{X}(t) = \sqrt{\int_V [\delta\mathbf{u}(t)^2 + \delta\theta(t)^2] dV}$. Note that the result for λ_1 is independent of the choice of the norm since (5.8) is a ratio of lengths at different times [75].

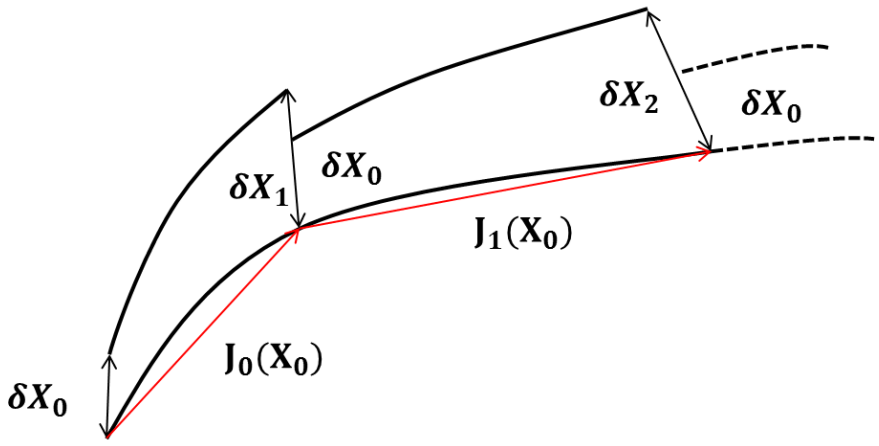

Figure 5.6: Procedure of renormalisation for the numerical calculation of largest Lyapunov exponent in Eq (5.7)

In practice, the initial perturbation $\delta\mathbf{X}(0)$ is chosen to be proportional to the full flow field, so that the incompressibility of the flow is automatically verified. The norm of the perturbation is chosen to be 1000 times smaller than that of the full flow field. We integrated the Navier-Stokes equation for two different initial conditions $\mathbf{X}(0)$ and $\mathbf{X}(0)+\delta\mathbf{X}(0)$ in time. The time of integration should be long enough so that trajectories could diverge, yet remain small enough so that the linearization concept still applies. A good compromise was found to be 50 nondimensional time units (5000 time-steps). After integrating over this length of time, a renormalisation of the perturbation is applied as $\delta\mathbf{X}(t)_{new} = \frac{\|\delta\mathbf{X}(0)\|}{\|\delta\mathbf{X}(t)\|}\delta\mathbf{X}(t)$. The two new initial conditions for the following 5000 time-steps integration become $\mathbf{X}(t)$ and $\mathbf{X}(t) + \delta\mathbf{X}(t)_{new}$. This crucial step aims at keeping the orbits close while allowing the difference between the two solutions to relax towards the most unstable eigenvector of the linearized operator. Iterating this procedure

and measuring successive expansion rates $\frac{\|\delta\mathbf{X}(t)\|}{\|\delta\mathbf{X}(0)\|}$ provides us with an asymptotic estimate for leading Lyapunov exponent λ_1 defined in Eq (5.8). This technique was tested with the Lorenz model (Eq. (5.3) with $\sigma = 28$, $r = 8/3$, $b = 28$), where we found the largest Lyapunov exponent is $\lambda_1 = 0.892446...$, which is consistent with the value $\lambda_1^* = 0.91 \pm 0.01$ given in the book of Sprott [66]. The method was then implented in our DNS code, using the nonlinear equations instead of the linearized equations [76] to advance the system in time.

5.3 Results $A_z = 2.5$ & $A_y = 1$

5.3.1 Period-doubling cascade

Local analysis

As reported in Chapter 4, after having experienced two supercritical pitchfork bifurcations at $Ra = 5708$ and $Ra = 9980$ through which the flow becomes 2D steady then 3D steady, a supercritical Hopf bifurcation occurs at $Ra = 11270$, as the flow enters a temporally mono-periodic oscillation regime. As the Rayleigh number increases, a sequence of period-doubling bifurcations is observed, which leads the flow to a temporally chaotic regime [77]. An illustration of this period-doubling cascade is given by phase portraits obtained from the temperature timeseries at two points in the flow as in Figure 5.7 (a)-(e).

A bifurcation diagram of Figure 5.8 is constructed from local maxima θ_n of the temperature timeseries at the point (0.038 0.097 0.983), which is located in the boundary layer near the hot wall.

Since each of the period-doubling bifurcations corresponds to a pitchfork bifurcation in the Poincaré section [36], the square of the difference between the variables of the two bifurcated branches increases quasi-linearly with the Rayleigh number in the neighbourhood of the local critical Rayleigh numbers $Ra_{2^i \to 2^{i+1}}$ $(i = 0, 1, 2, 3, ...)$ after each bifurcation. Therefore, linear extrapolation can be used to estimate the local critical Rayleigh number $Ra_{2^i \to 2^{i+1}}$ of each period-doubling bifurcation. An example for the bifurcation from 4 periods to 8 periods is represented in Figure 5.9, where $Ra_{4 \to 8}$ is found to be 12305.76 by linear extrapolation.

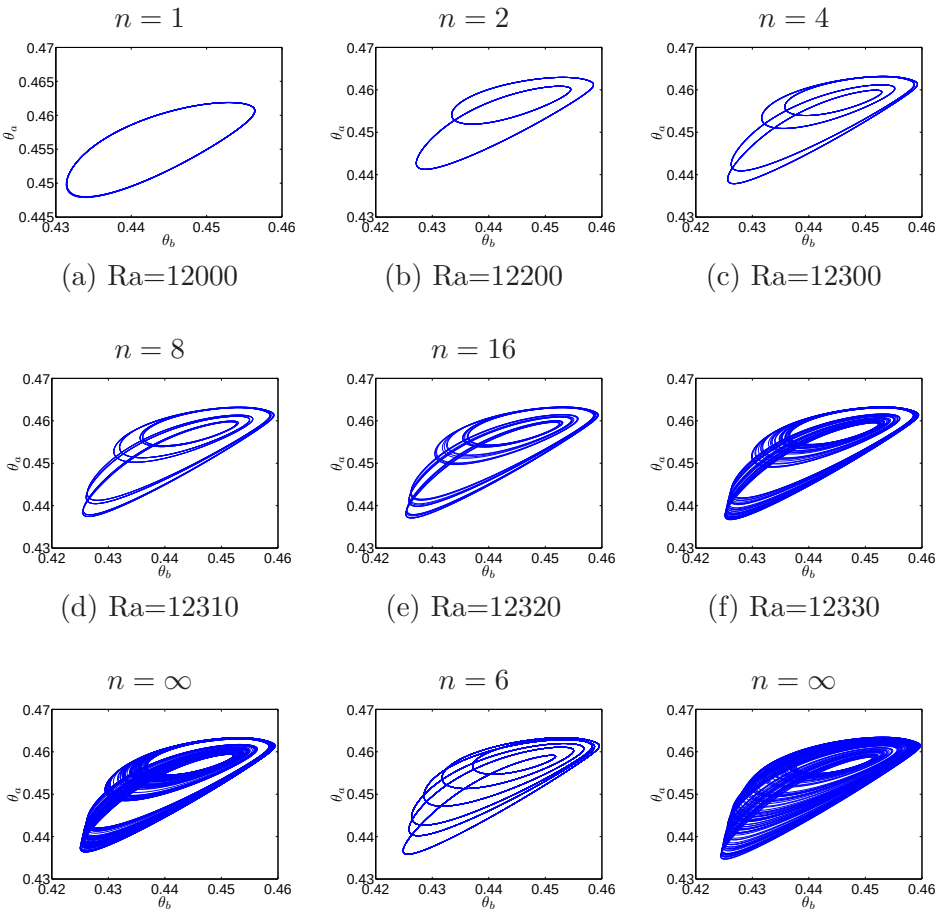

(a) Ra=12000 (b) Ra=12200 (c) Ra=12300

(d) Ra=12310 (e) Ra=12320 (f) Ra=12330

(e) Ra=12338 (f) Ra=12350 (g) Ra=12380

Figure 5.7: Phase portraits at different Ra, $A_z = 2.5$. Abscissa: Temperature measured at the point (0.038, 0.097, 0.983); ordinate: Temperature measured at the point (0.038, 0.903, 0.983).

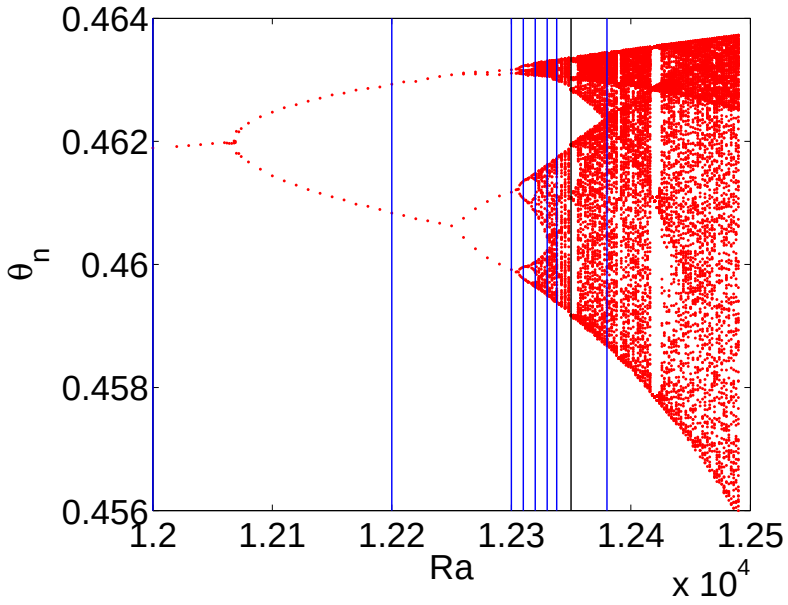

Figure 5.8: Bifurcation diagram obtained by using the local maxima θ_n of the temperature timeseries at the point (0.038 0.097 0.983). Vertical lines in the figure correspond to the different Rayleigh numbers, at which the phase portraits are drawn in Figure 5.7.

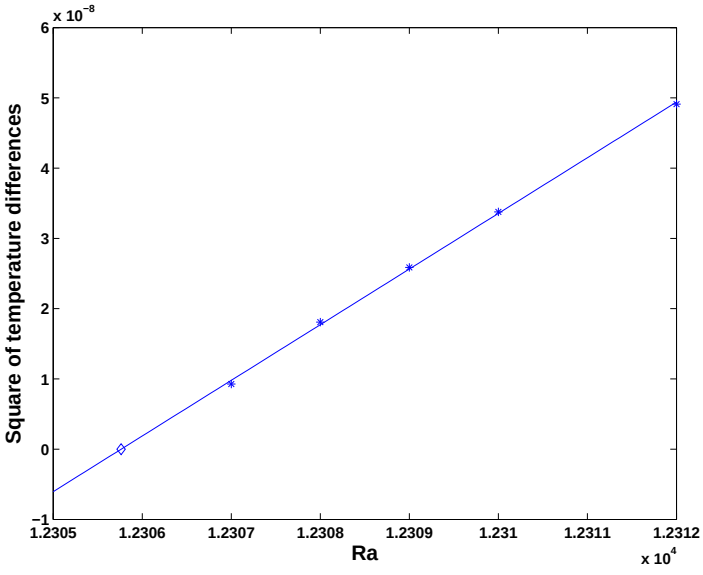

Figure 5.9: Square of the temperature difference between two bifurcated branches increases almost linearly as a function of Ra. By linear extrapolation, the local critical Rayleigh numbers Ra_{4-8} is evaluted to be around 12305.76.

Table 5.1: Summary of period-doubling bifurcations

Bifurcations $2^i \rightarrow 2^{i+1}$	Local critical $Ra_{2^i \rightarrow 2^{i+1}}$	Estimated Feigenbaum constant $\tilde{\delta}$
0-1	11270	
1-2	12068.09	
2-4	12258.42	4.193
4-8	12305.76	4.020
8-16	12316.72	4.321

Table 5.2: Windows observed in the bifurcation diagram

Rayleigh number	number of periods
12335	12
12340	10
12350	6
12390	5
12420	5

From these estimates, approximations for the Feigenbaum constant are calculated and listed in Table 5.1. Some agreement with the theoretical value $\delta = 4.66920161....$ is observed [69]. The discrepancy is likely due to two effects: (i) the Feigenbaum number is an asymptotic constant while our estimates are based on the first few bifurcations, (ii) linear extrapolation cannot be accurate when local critical Rayleigh numbers become very close to each other. Using the theoretical Feigenbaum number, the chaotic regime is estimated to be reached around $Ra \sim 12320$. For higher Rayleigh numbers, the chaos continues to develop as shown in the bifurcation diagram (Figure 5.8). Several periodic windows are observed, and their numbers of cycles are listed in Table 5.2. For example, a large '*period-6* windows' (2 *period-3* windows in each band) is observed at $Ra = 12350$ in the bifurcation diagram. It corresponds to two 3-cycles orbit (totally 6 periods) in the phase portrait 5.7 (f). It then undergoes a period doubling cascade in which orbits of period 3×2^m are successively produced. This cascade once again leads to chaotic behavior. For still higher Rayleigh numbers, the attractor abruptly widens into two large bands similar in size to these observed at $Ra < 12350$. The two large bands merge at around $Ra = 12380$ and form a single large chaotic band.

Spatio-temporal organization of the flow

As opposed to Chapter 4, the simulation domain (MFU) accommodates only one flow structure, so that A_z is set to 2.5. Consistent with the previous results in Chapter 4, the flow structure in the chaotic regime is 3D, and consists of a primary roll which is deformed in its transverse direction, with two counter-rotating braids of oblique vorticity originating from the rolls [77] as shown in Figure 5.10.

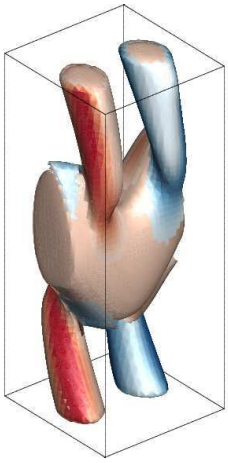

Figure 5.10: Q-criterion visualization of flow structure at $Ra = 12380$, $Q = 0.25$

The chaotic oscillation of the structures can be visualized by streamline plots on two selected vertical planes in Figure 5.11. The primary roll is severely squeezed (Figure 5.11 (a) top) by the secondary counter-rotating vortices, whose size is quite large (Figure 5.11 (a) middle). Then at $t = 7010$, the size of the primary roll increases. Inside this roll smaller counter-rotating vortices become visible (Figure 5.11 (b) middle), while the connecting vorticity braids shrink (Figure 5.11 (b) middle). At $t = 7020$, the size of the primary roll starts to decrease (Figure 5.11 (c) top), while both braids and small vortices inside the primary roll reach a relative large size (Figure 5.11 (c) middle).

Fourier analysis can provide a useful description of the flow. The Fourier modes $\hat{w}(i_y, i_z)$ $(i_y, i_z = 0, 1)$ of the vertical velocity on a vertical plane at $x = 0.381$ are represented in Figure 5.12. The mode $(0, 0)$ experiences strong fluctuations. The mode $(0, 1)$ corresponds to the primary roll, and carries most of the energy of the fluctuations. Its phase oscillates around

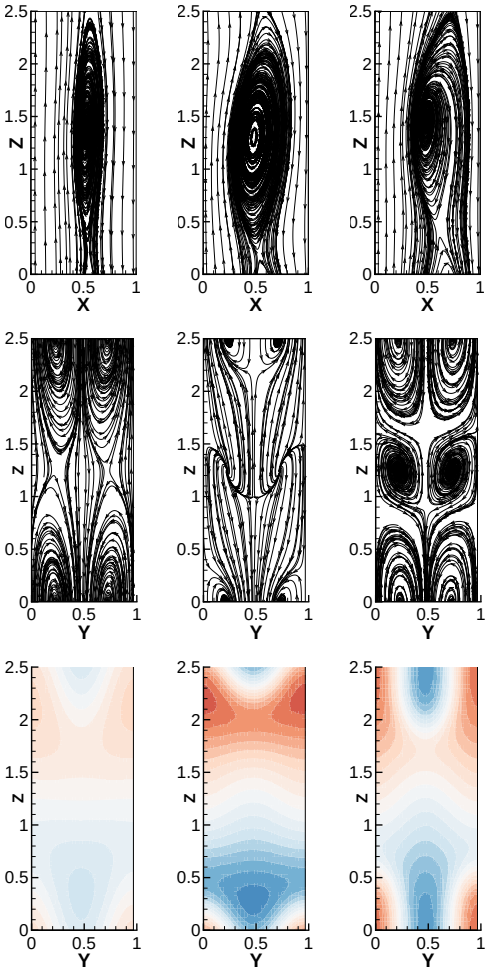

(a) t=7001 (b) t=7010 (c) t=7020

Figure 5.11: Flow streamlines and temperature isocontours at three instants at $Ra = 12380$ on two vertical planes ($y = 0.5$ and $x = 0.5$)

a mean value, meaning that the position of flow structures oscillates vertically around a fixed location. Modes $(1,0)$ and $(1,1)$ also contain substantial energy. The phase of mode $(1,0)$ is constant, which reflects that the motion of the flow is highly constrained in the transverse direction y.

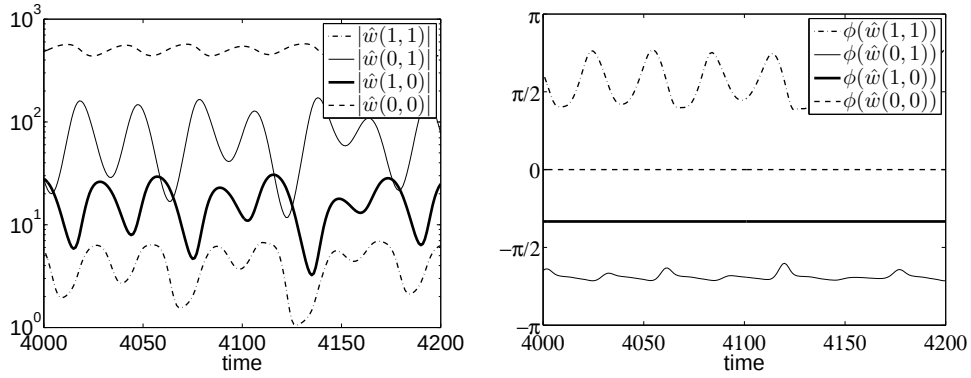

Figure 5.12: Temporal evolutions of Fourier modes $\hat{w}(i_y, i_z)$ $(i_y, i_z = 0, 1)$ obtained by the Fourier transform of the vertical velocity w distribution on an arbitrarily chosen vertical plane at $x = 0.381$, $Ra = 12380$: (a) modulus, (b) phase.

From the analysis above, we see that the Fourier mode $(0,1)$ can be considered as a good indicator of the global flow behavior. For simplicity, we focus on the Fourier mode $\hat{\theta}(i_y = 0, i_z = 1)$ of the vertical velocity distribution on a vertical plane $x = 0.381$. The first return map based on the timeseries of Fourier mode $\hat{\theta}(i_y = 0, i_z = 1)$ is represented in Figure 5.13. As can be seen, all the points neatly fell on one single curve, which is similar to the case of the Lorenz map [70]. The curve is found to be quite similar to that of quadratic one-dimensional maps [69]. It can be shown that 1-D maps with a quadratic maximum are expected to follow a Feigenbaum scenario [36]. The right part of the curve consists of two branches, which are very close to each other and almost indistinguishable. As Ra increases, the curve becomes thicker, and several folds can be seen in Figure 5.13 (b). The folds of the right branch can be seen as the projected image of the higher dimensional attractor on the 2D maps, since we can unfold this first return map in a 3D plot, in which all the points fall neatly on a curve. This shows that the fractal dimension of our system is higher than 1.

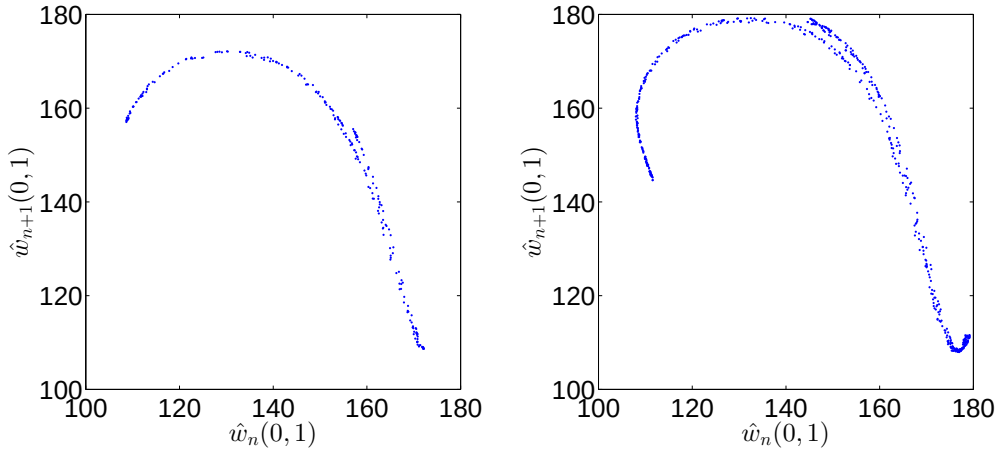

(a) $Ra = 12380$ (b) $Ra = 12490$

Figure 5.13: First return maps ploting $\hat{w}_n(i_y = 0, i_z = 1)$ vs $\hat{w}_{n+1}(i_y = 0, i_z = 1)$. $\hat{w}_n(i_y = 0, i_z = 1)$ is the local maxima of Fourier timeseries $\hat{w}(i_y = 0, i_z = 1)$ calculated from the vertical velocity w distribution on the vertical plane $x = 0.0381$.

5.3.2 Crisis-induced intermittency

Local analysis

The bifurcation diagram for the range $Ra \in [12400, 12600]$ is represented in Figure 5.14. At $Ra \sim 12490$, $Ra \sim 12510$, $Ra \sim 12540$, several abrupt enlargements of the band are observed, which correspond to interior crises. During these crises the basin of the chaotic attractor is extended, which means that the oscillation of the flow structures around a fixed location increases in amplitude. At $Ra = 12546$, a new set of local maxima abruptly appears on the top-right corner of the Figure 5.14, which is the sign of another type of crisis [68]. The spatio-temporal behavior of the flow is then significantly modified.

Above the Rayleigh number $Ra = 12546$, intermittent behavior is observed, as is indicated in Figure 5.15, which represents the temporal evolution of the first Fourier mode $\hat{w}(i_y = 0, i_z = 1)$ for $Ra = 12600$. This evolution is characterized by random switches between positive and negative states.

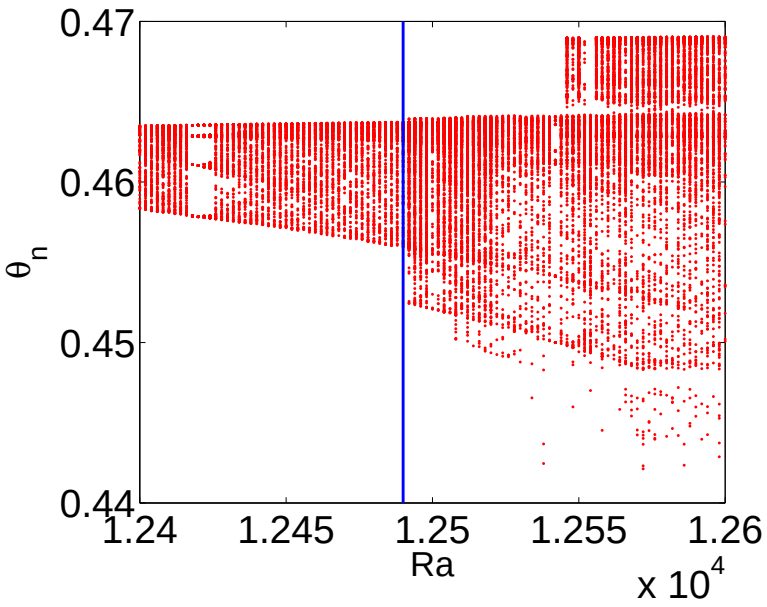

Figure 5.14: Bifurcation diagram obtained by using the local peaks θ_n of the timeseries at the point (0.038 0.097 0.983).

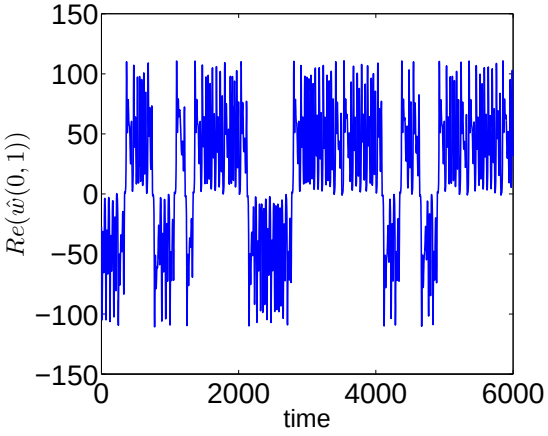

Figure 5.15: Real part of the temporal evolution of the Fourier mode $\hat{w}(i_y = 0, i_z = 1)$ calculated on the vertical plane $x = 0.0381$, $Ra = 12600$.

Spatio-temporal organization of the flow

A description of the flow structure is given by streamline plots and temperature isocontours in Figure 5.16. As can be seen, the primary roll is located in the center of the domain (Figure 5.16 (a) top), and the braids and small secondary vortices inside the primary roll are also visible (Figure 5.16 (a) middle row). The temperature isocontour on the plane $x = 0.5$ is strongly 3D (Figure 5.16 (a) bottom). Then at $t \sim 8525$, the primary roll is completely squeezed (Figure 5.16 (b) top), and the flow becomes quasi-invariant in the vertical direction z (Figure 5.16 (b) middle and bottom). At $t \sim 8530$ a new primary roll identical in shape to the previous one forms at a different location, which is separated from the original location by half a wavelength $\Delta z = \frac{A_z}{2} = 1.25$ (Figure 5.16 (c) top). Later on, at $t \sim 8540$ the secondary structures disappear (Figure 5.16 (d) middle and bottom), and the flow is almost invariant in the transverse direction y. At $t = 8575$ (Figure 5.16 (e)), the 3D flow structure is recovered, and presents identical features to that of Figure 5.16 (a) within a translation.

Dynamics of the corresponding chaotic system

The switch of flow structures between two locations of separated by half of the wavelength $A_z = 2.5$ suggests the existence of a heteroclinic connection between two chaotic attractors, which are located on the $O(2) \times O(2)$ invariant torus of chaotic solutions. This symmetry can be clearly identified by comparing the phase portraits of the cases before and after the crisis. The phase portraits use the temporal evolutions of the Fourier modes $\hat{w}(i_y = 0, i_z = 1)$, $\hat{w}(i_y = 1, i_z = 0)$ as in Figure 5.17 (a) and (b). Structurally stable heteroclinic connections between fixed points or periodic solutions have been shown to exist in the systems with $O(2)$ symmetry [78, 79]. However, we are not aware of equivalent theoretical results for heteroclinic connections between two strange attractors. Similar observations in a simplified dynamical model displaying random reversal of the magnetic field have been reported, which are due to a crisis-induced intermittency caused by the collision of two identical strange attractors [80]. Other similar reversals are also reported for the large scale field generated over a turbulent background [81, 52].

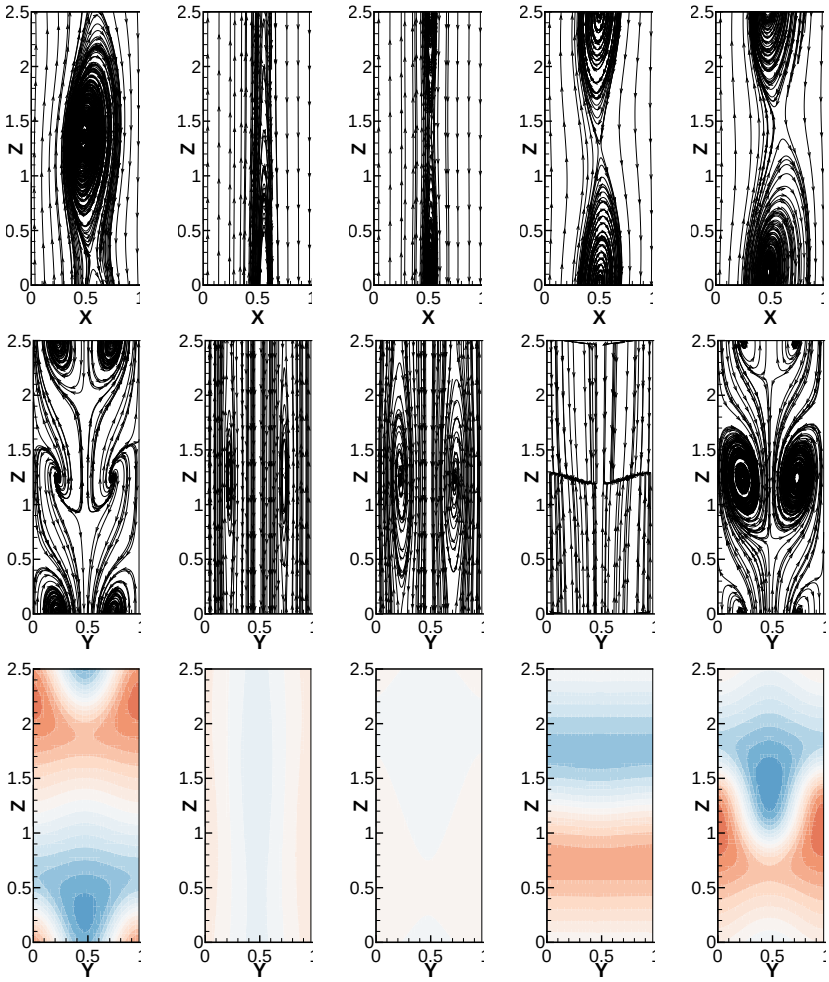

(a) t=8505 (b) t=8525 (c) t=8530 (d) t=8540 (e) t=8575

Figure 5.16: Temporal evolution of flow structures at $Ra = 12600$. Upper row: flow streamlines at different instants on the plane $y = 0.5$; Middle row: flow streamlines at different instants on the plane $x = 0.5$; Bottom row: temperature isocontours on the plane $x = 0.5$

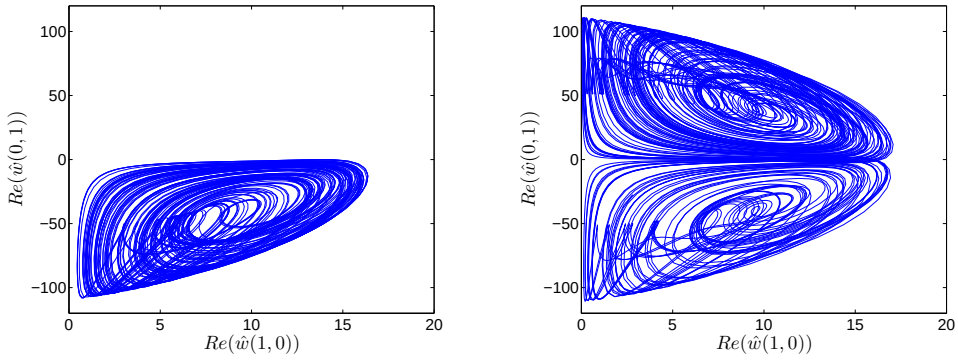

Figure 5.17: Phase portraits. Abscissa: real part of the temporal evolution of the Fourier mode $\hat{w}(i_y = 0, i_z = 1)$ calculated on vertical plane $x = 0.0381$; ordinate: real part of the temporal evolution of the Fourier mode $\hat{w}(i_y = 1, i_z = 0)$. (a) $Ra = 12500$ (b) $Ra = 12600$

The largest Lyapunov exponent gives a measure of the complexity of the system and is shown in Figure 5.18. Tests carried out for two different integration lengths in the chaotic regime led to similar results. A large gap can be observed between the chaotic and intermittent regimes, where the contribution is mainly due to the trajectory divergence caused by the shift of the flow structures by half a wavelength $A_z/2$. We are aware that the temporal integration of our simulation may be not long enough, which leads to the discrepancy of results in the intermittent regimes.

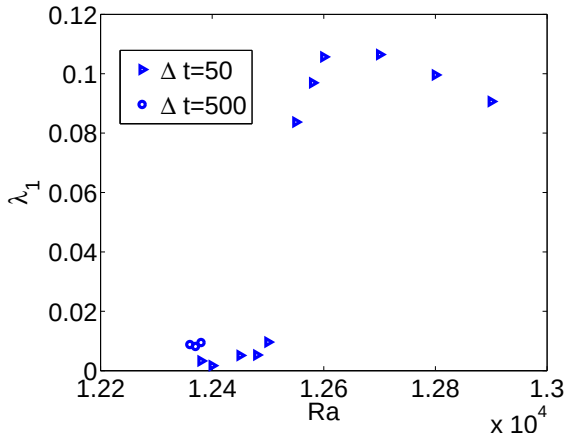

Figure 5.18: The largest Lyapunov exponent at different Rayleigh numbers

As Ra is further increased beyond about $Ra = 13000$, a new periodic regime is observed. The Fourier mode $\hat{w}(i_y = 0, i_z = 1)$ evolution and the phase portraits of the Fourier modes

($\hat{w}(i_y = 0, i_z = 1)$ and $\hat{w}(i_y = 1, i_z = 0)$) are presented in Figure 5.19. The symmetry of the attractor is the same as before.

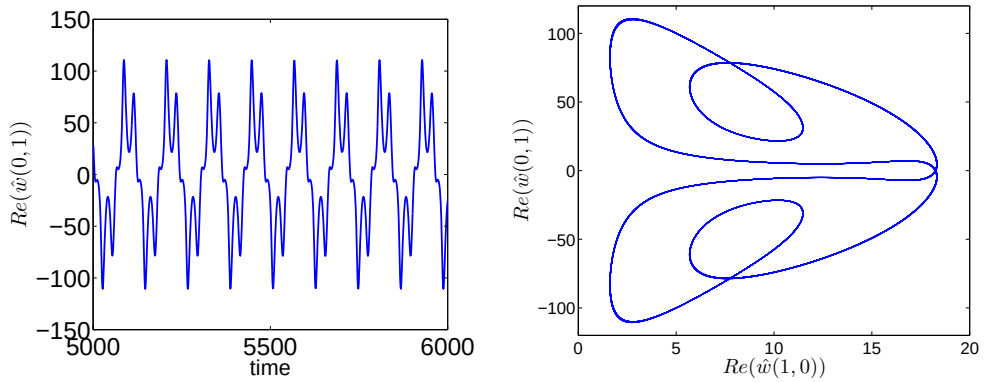

(a) (b)

Figure 5.19: (a) Real part of the temporal evolution of the Fourier mode $\hat{w}(i_y = 0, i_z = 1)$ calculated on the vertical plane $x = 0.0381$; (b) phase portraits. Abscissa: real part of the temporal evolution of the Fourier mode $\hat{w}(i_y = 0, i_z = 1)$; ordinate: real part of the temporal evolution of the Fourier mode $\hat{w}(i_y = 1, i_z = 0)$. $Ra = 13000$

The periodic behavior observed at $Ra = 13000$ corresponds to a "periodic windows" regime extended between $Ra = 13000$ and $Ra = 13100$ in the bifurcation diagram. When Ra is increased to $Ra = 13200$, the temporal behavior of the flow becomes chaotic again. As shown by the temporal evolution of Fourier mode $\hat{w}(i_y = 0, i_z = 1)$ in Figure 5.20 (a), it recovers a new intermittent regime which is characterized by the random switches between two physical positions of the transverse rolls. The characteristic time of the oscillations around one of the equilibrium positions decreases as Ra increases. At $Ra = 14000$, the system remains around each position for a relatively short time (about 1 or 2 basic pulsation periods), compared to the case at $Ra = 13200$ with about 4 to 5 basic pulsation periods. The Fourier spectrum calculated from the temperature timeseries at one point is represented in in Figure 5.20 (b) and shows an almost continuous spectrum, which indicates that the flow is temporally chaotic. At higher Rayleigh numbers $Ra = 14200$ and $Ra = 14500$, a new periodic regime are observed. The characteristics time is smalle than that of the periodic regime observed at $Ra = 13000$. This new periodic regime also corresponds to the "periodic windows" regime.

The time scale τ characterizing the switches between the two chaotic states obeys the logarithmic law $\tau \sim (Ra - Ra_{ci})^{-\gamma}$ with a value of $\gamma \sim 0.784$ (see Figure 5.21). As pointed out

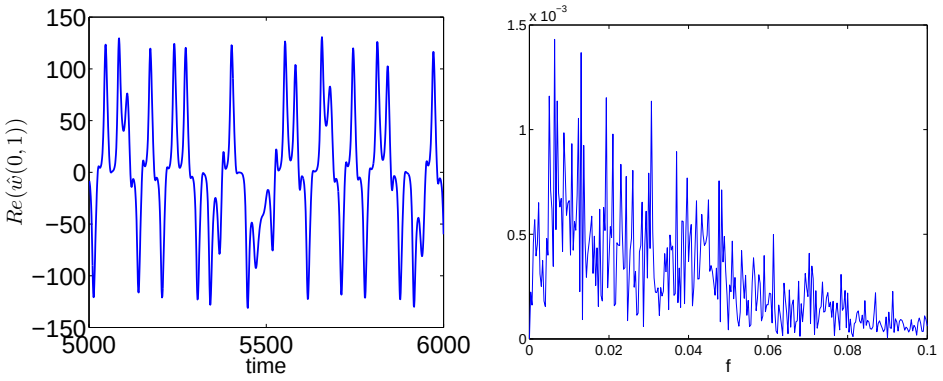

(a) (b)

Figure 5.20: (a) Real part of the temporal evolution of the Fourier mode $\hat{w}(i_y = 0, i_z = 1)$ calculated on the vertical plane $x = 0.0381$. (b) Fourier spectrum of the temperature timeseries at the point (0.038 0.097 0.98) $Ra = 14000$

[68, 82], for one-dimensional maps with generic quadratic maxima, the critical exponent of crisis γ is strictly equal to $\frac{1}{2}$, while for higher-dimensional maps, γ is larger than $\frac{1}{2}$. Our result is therefore consistent with the analysis of Figure 5.13 that our system has a fractal dimension larger than 1. From Figure 5.21 shows that the characteristic time of switches follow the same power law outside periodic windows at $Ra \in [13000, 13100]$ and $Ra \in [14200, 14500]$. The characteristic time associated with periodic windows also appear to follow a similar scaling law, but are slightly shorter then their chaotic counterparts, which can be expected as the system does no longer hover from one unstable orbit to another.

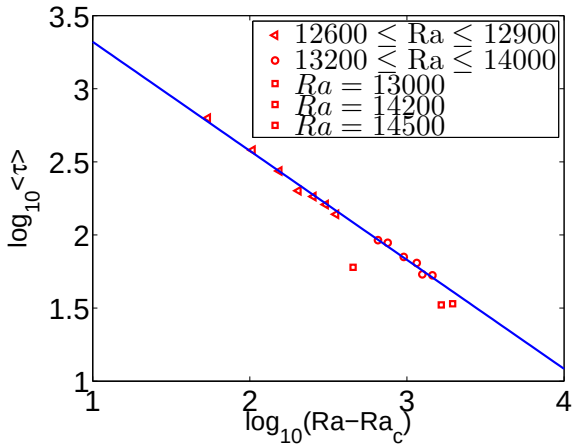

Figure 5.21: $log_{10}\langle\tau\rangle$ vs $log_{10}(\mathrm{Ra} - \mathrm{Ra}_c)$. The slope of the straight line gives $\gamma \approx 0.784$.

5.4 Conclusion

The dynamics of the natural convection between two vertical plates maintained at different temperatures have been studied in a domain of small periodic dimensions. Temporal chaos occurs through a sequence of period-doubling bifurcations. In physical space, it corresponds to the modulated pulsation of a three-dimensional spatially localized structure, which consists of a distorted transverse roll connected by secondary vortices or braids. Estimates of the Feigenbaum constant from the first few bifurcations are reasonably close to the expected theoretical value. A bifurcation diagram as Ra is increased was constructed from the temperature evolution of a point in the flow. Several features common to the characteristics of one-dimensional maps were identified, such as periodic windows and interior crises leading to successive period-doubling bifurcations. When Ra was further increased, a crisis-induced intermittency was observed, as the flow structures were shifted back and forth vertically by half a wavelength. A periodic window occurs for higher Rayleigh numbers, which then gives way to intermittent, chaotic behavior again. The intermittent behavior observed suggests that heteroclinic connections could be occuring between strange attractors, which is a fairly generic feature of systems with $O(2)$ symmetry. To the best of our knowledge, the crisis-induced intermittency has not been reported for natural convection in the absence of other mechanisms (vibrations, radiation). Our analysis shows that crisis-induced intermittency can also be a possible route to chaos for natural convection in addition to the classic Pomeau-Manneville type intermittency scenario.

Chapter 6

3D Channel of large extent

6.1 Introduction

As mentioned in Chapter 1, several studies have investigated the sequence of instabilities of the flow between two differentially heated walls in the 3D configuration. We will focus on the results of three studies [31, 32, 33].

Nagata and Busse [31]

A significant study was that of Nagata and Busse [31]. They investigated the sequence of instabilities in a shear layer between two differentially heated side-walls in the limit of $Pr = 0$. The primary instability consisted of 2D transverse rolls and the stability of these rolls was examined. Three secondary instability mechanisms were identified: the Eckhaus instability in the vertical direction, a monotone instability, and an oscillatory instability. The monotone instability (denoted A for consistency with Chait and Korpela's notation) occurs at around $Gr = 8200$ ($Ra = 5822$ for $Pr = 0.71$), and transformed the 2D flow into a steady 3D pattern corresponding to "a vortex-pairing instability with alternating pairing in the spanwise direction" [31] or pinched rolls as shown in Figure 6.1 (a). This 3D pattern becomes unstable when $Gr > 11060$ ($Ra > 7852$) and gives way to an oscillatory 3D pattern, which corresponds to structures shifted back and forth periodically in time in the transverse direction. The spanwise wavelength of the structures is twice that of the steady pattern associated with the monotone instability A .

Chait and Korpela [32]

Chait and Korpela [32] also studied the stability of 2D rolls for air ($Pr = 0.71$) convection between two vertical differentially heated plates. The stability map they obtained for the 2D rolls is shown in Figure 6.2. Besides the three instabilities found by Nagata and Busse [31], they

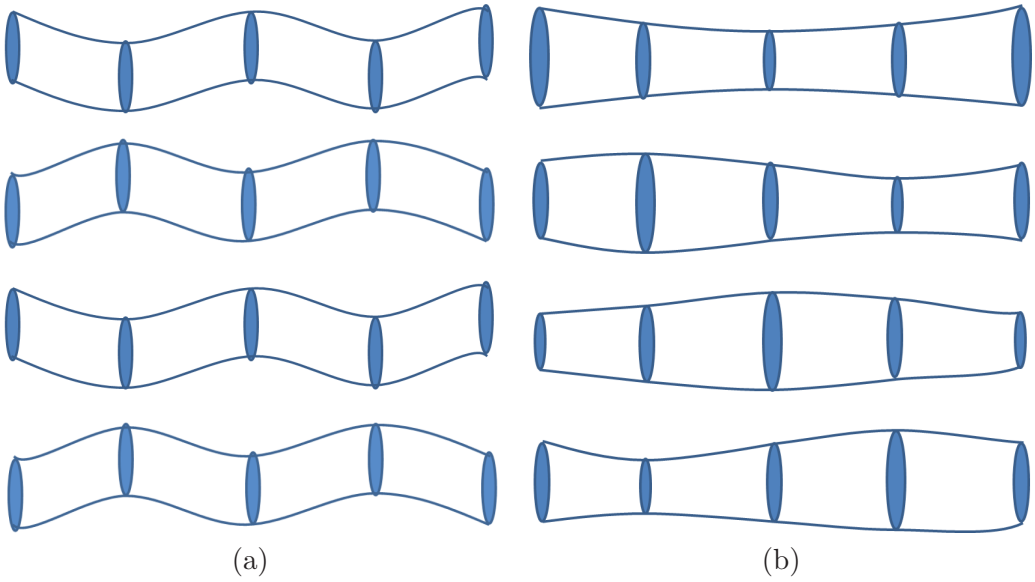

Figure 6.1: Flow patterns corresponding to monotone instability A (a) and monotone instability B (b).

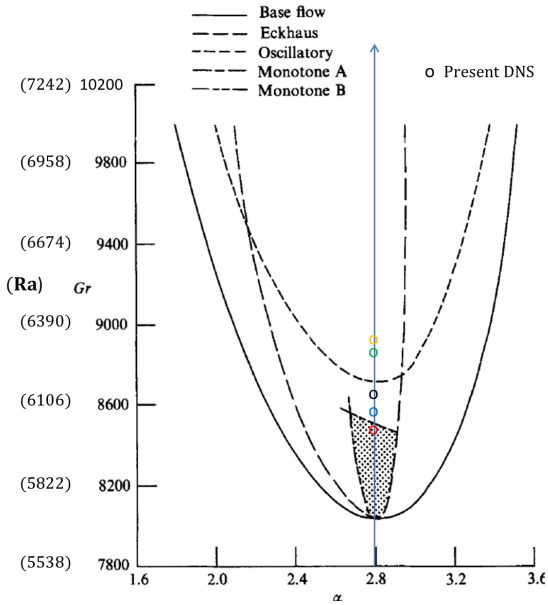

Figure 6.2: DNS results superimposed on stability diagram of the multicellular flow for air ($Pr = 0.71$) found by Chait and Korpela [32]. The shaded aera represents the domain of stable secondary rolls. Our DNS runs: red circle, $Ra = 6050$; blue circle, $Ra = 6100$; black circle, $Ra = 6150$; green cirle, $Ra = 6250$; orange circle, $Ra = 6300$. Note that wavenumber α in this figure corresponds to k_z in our notation.

identified a second monotone instability, which is denoted B in their article. Since Pr is not zero, the stability map is somewhat different from Nagata and Busse's [31]: (i) the curve of Eckhaus instability is no longer symmetric with respect to the vertical line $k_z = k_c$; (ii) the threshold of the primary instability and the monotone instability A are slightly increased. The stability limit for the A mechanism constrains the domain of stable rolls from above and the critical Rayleigh number for it occurs at around $Gr = 8400$ ($Ra = 5964$). The stability limit associated with the B mechanism originates in the vicinity of the critical point. To the left of it, i.e. for lower wavenumbers, the primary rolls are always unstable. The pattern associated with instability B consists of periodic thickening and thinning secondary rolls in the transverse direction y as shown in Figure 6.1 (b), which resembles the skewed varicose instability in Rayleigh-Bénard convection.

Clever and Busse [33]

Clever and Busse [33] computed equilibria and traveling wave solutions for air convection between two vertical differentially heated plates. They obtained a flow pattern as shown in Figure 1.7 (a) in Chapter 1, which is associated with the monotone instability A at $Gr = 9859$ ($Ra = 7000$) and is in agreement with Nagata and Busse [31], as well as Chait and Korpela [32]. Using symmetry considerations, they charted other possible solutions at $Gr = 9859$, $Gr = 12676$, $Gr = 16901$ ($Ra = 7000$, $Ra = 9000$, $Ra = 12000$). This flow consists of a traveling wave of 3D invariant shape moving downward, which is different from the oscillatory flow pattern found by Nagata and Busse [31]. Both the instability A flow pattern and the traveling wave flow were found to exist at $Gr = 9859$ ($Ra = 7000$). This is not completely in agreement with Wright *et al.*'s experiment [30], who observed apparently 2D rolls at $Ra = 6800$ moving slowly downwards. 2D rolls moving slowly downwards were also identified in the experimental results and the 2-D numerical simulation of Lartigue *et al.* [29].

Although common 3D instability mechanisms were identified in the three studies, the sequence of bifurcations is not entirely clear. Moreover, it is not known which possible solutions are actually found in the flow. Before using nonlinear simulations to answer these questions, we need to determine if and how the onset of these instabilities depends on the dimensions of

the plates.

6.2 Linear stability analysis of the secondary 2D flow

The stability map of 2D rolls at $Pr = 0.71$ has been already obtained by Chait and Korpela [32]. They showed that the secondary instability of the flow appears for an increase in Rayleigh number less than 10% of the critical Rayleigh number $Ra_c = 5708$. However their paper does not show how the critical spanwise wavenumber k_y depends on the height of the plate. Our first step is therefore to determine the critical spanwise wavenumber associated with a given periodic height of the plate. We use for this an Arnoldi method, which will be detailed in the next section.

6.2.1 Numerical Methods

We firstly use a 2D DNS code to obtain the base flow, which consists of steady co-rotating rolls. A linearized version of the DNS code is used to study the stability of the base flow. The Arnoldi method has been used in several studies to study hydrodynamic instability, as for instance for natural convection in a rectangular cavity [83] or spherical Couette flow [84]. The details of the DNS codes used here can be found in [83, 85]. Here we briefly present the numerical methods.

Base flow

In Chapter 4, the first instability is found to be 2D and steady. It corresponds to a supercritical pitchfork bifurcation. The secondary flow consists of steady 2D co-rotating rolls when Ra is above the critical Rayleigh number $Ra_c = 5708$. Therefore, we can use a 2D DNS code to construct the base flow (U,$V = 0$,W,Θ) by solving the unsteady Navier-Stokes equations under the Boussinesq approximation Eq. (2.1) with boundary conditions Eq. (2.2) - (2.3).

The code we used is a spectral DNS code [83, 85]. The Chebyshev-Fourier collocation method is used for the spatial discretization. Incompressibility is enforced by the projection-correction method. The equations are integrated in time with a second-order mixed explicit-implicit scheme.

Linearized unsteady Navier-Stokes equations

The stability of the base flow ($U(x,z)$,$V=0$,$W(x,z)$,$\Theta(x,z)$) with respect to a 3D perturbation ($u(x,y,z)$,$v(x,y,z)$,$w(x,y,z)$,$\theta(x,y,z)$) can be tested by integrating the linearized 3D unsteady Navier-Stokes equations, which take the following form:

$$\begin{aligned}
&\frac{\partial u}{\partial x}+\frac{\partial v}{\partial y}+\frac{\partial w}{\partial z}=0\\
&\frac{\partial u}{\partial t}+U\frac{\partial u}{\partial x}+W\frac{\partial u}{\partial z}+u\frac{\partial U}{\partial x}+w\frac{\partial U}{\partial z}=-\frac{\partial p}{\partial x}+\frac{Pr}{\sqrt{Ra}}\left(\frac{\partial^2 u}{\partial x^2}+\frac{\partial^2 u}{\partial y^2}+\frac{\partial^2 u}{\partial z^2}\right)\\
&\frac{\partial v}{\partial t}+U\frac{\partial v}{\partial x}+W\frac{\partial v}{\partial z}=-\frac{\partial p}{\partial y}+\frac{Pr}{\sqrt{Ra}}\left(\frac{\partial^2 v}{\partial x^2}+\frac{\partial^2 v}{\partial y^2}+\frac{\partial^2 v}{\partial z^2}\right)\\
&\frac{\partial w}{\partial t}+U\frac{\partial w}{\partial x}+W\frac{\partial w}{\partial z}+u\frac{\partial W}{\partial x}+w\frac{\partial W}{\partial z}=-\frac{\partial p}{\partial z}+\frac{Pr}{\sqrt{Ra}}\left(\frac{\partial^2 w}{\partial x^2}+\frac{\partial^2 w}{\partial y^2}+\frac{\partial^2 w}{\partial z^2}\right)+Pr\theta\\
&\frac{\partial \theta}{\partial t}+U\frac{\partial \theta}{\partial x}+W\frac{\partial \theta}{\partial z}+u\frac{\partial \Theta}{\partial x}+w\frac{\partial \Theta}{\partial z}=\frac{1}{\sqrt{Ra}}\left(\frac{\partial^2 \theta}{\partial x^2}+\frac{\partial^2 \theta}{\partial y^2}+\frac{\partial^2 \theta}{\partial z^2}\right)
\end{aligned} \tag{6.1}$$

In our configuration, the periodic condition is imposed in the direction y. Thus, we can suppose that the 3D perturbation takes a periodic form as $[u(x,z,t)cos(k_y y)$, $v(x,z,t)sin(k_y y)$, $w(x,z,t)cos(k_y y)$, $\theta(x,z,t)cos(k_y y)]$, where k_y is the wavenumber in y direction. With this assumption of periodicity for the perturbations, the Eq (6.1) becomes

$$\begin{aligned}
&\frac{\partial u}{\partial x}+k_y y+\frac{\partial w}{\partial z}=0\\
&\frac{\partial u}{\partial t}+U\frac{\partial u}{\partial x}+W\frac{\partial u}{\partial z}+u\frac{\partial U}{\partial x}+w\frac{\partial U}{\partial z}=-\frac{\partial p}{\partial x}+\frac{Pr}{\sqrt{Ra}}\left(\frac{\partial^2 u}{\partial x^2}+\frac{\partial^2 u}{\partial z^2}-k_y^2 u\right)\\
&\frac{\partial v}{\partial t}+U\frac{\partial v}{\partial x}+W\frac{\partial v}{\partial z}=-\frac{\partial p}{\partial y}+\frac{Pr}{\sqrt{Ra}}\left(\frac{\partial^2 v}{\partial x^2}+\frac{\partial^2 v}{\partial z^2}-k_y^2 v\right)\\
&\frac{\partial w}{\partial t}+U\frac{\partial w}{\partial x}+W\frac{\partial w}{\partial z}+u\frac{\partial W}{\partial x}+w\frac{\partial W}{\partial z}=-\frac{\partial p}{\partial z}+\frac{Pr}{\sqrt{Ra}}\left(\frac{\partial^2 w}{\partial x^2}+\frac{\partial^2 w}{\partial z^2}-k_y^2 w\right)+Pr\theta\\
&\frac{\partial \theta}{\partial t}+U\frac{\partial \theta}{\partial x}+W\frac{\partial \theta}{\partial z}+u\frac{\partial \Theta}{\partial x}+w\frac{\partial \Theta}{\partial z}=\frac{1}{\sqrt{Ra}}\left(\frac{\partial^2 \theta}{\partial x^2}+\frac{\partial^2 \theta}{\partial z^2}-k_y^2\theta\right)
\end{aligned} \tag{6.2}$$

Boundary conditions for Eq. (6.1) (6.2) are of Dirichlet type and homogeneous.

Suppose now (U,0,W) and (u,v,w) verifying the incompressibility condition, with the following notations: $\mathbf{X}=(U,0,W,\Theta)$, $\mathbf{x}=(u,v,w,\theta)$, L represents the 2D Laplace operator, N

represents the advection terms and the linear buoyancy term, and $N_{\mathbf{x}}$ is the Fréchet derivative of N on $\mathbf{X}$. We can recast Eq (6.2) into the following compact form:

$$\frac{\partial \mathbf{x}}{\partial t} = \left[\frac{C}{\sqrt{Ra}}(L - k^2 I) + N_{\mathbf{x}}\right]\mathbf{x} = J_{\mathbf{x}}\mathbf{x} \tag{6.3}$$

where $J_{\mathbf{x}}$ is the Jacobian and constant C is equal to 1 for θ and equal to Pr for velocities.

Arnoldi method

To detemine whether the perturbation $\mathbf{x}$ in Eq. (6.3) grows or decreases with respect to time t, we need to compute the eigenvalues of the Jacobian $J_{\mathbf{X}}$. However, the dimension of the discretized Navier-Stokes equation system is so large that we cannot compute these eigenvalues exactly, due to the available computing ressources. Therefore, we used the Arnoldi method, which provides approximates for them. The Arnoldi iteration relies on the orthogonalization of a Krylov subspace to provide a series of Hessenberg matrices which approximate $J_{\mathbf{X}}$. The eigenvalues of these Hessenberg matrices constitute the Ritz eigenvalues. In most circumstances the eigenvalues converge to some of the eigenvalues of $J_{\mathbf{X}}$ (typically the leading ones). The rate of convergence of the procedure is not fully understood yet in the general case.

After applying a mixed implicit-explicit scheme to Eq. (6.3) and some algebric calculations [83, 85, 84], we can show that if the time step Δt is sufficiently small, then

$$\mathbf{x}^{n+1} \approx \exp(\Delta t J_{\mathbf{X}})\mathbf{x}^n \tag{6.4}$$

Therefore, we can compute the iterative action of $J_{\mathbf{X}}$ on a given vector (an initial flow state) to form the Krylov subspace by successive time-stepping of the linearized Navier-Stokes system (6.2).

If Δt stays small enough, we can extend Eq (6.4) to $\mathbf{x}^{n+K} = \exp(\Delta t J_{\mathbf{x}})\mathbf{x}^{n+K-1} = ... = \exp(K\Delta t J_{\mathbf{X}})\mathbf{x}^n$. Therefore, the series $\mathbf{x}^{n+K}, \mathbf{x}^{n+2K}, ..., \mathbf{x}^{n+lK}$ is an approximation of a series $\exp(K\Delta t J_{\mathbf{X}})\mathbf{x}^n$, $\exp(2K\Delta t J_{\mathbf{X}})\mathbf{x}^n$,..., $\exp((l-1)K\Delta t J_{\mathbf{X}})\mathbf{x}^n$, which forms a Krylov subspace.

We can obtain a general relation as following:

$$(\mathbf{x}^{n+K}, \mathbf{x}^{n+2K}, ..., \mathbf{x}^{n+lK}) \approx \exp(K\Delta t J_{\mathbf{X}})(\mathbf{x}^{n}, \mathbf{x}^{n+K}, \mathbf{x}^{n+2K}, ..., \mathbf{x}^{n+(l-1)K}) \tag{6.5}$$

This relation shows that $(\mathbf{x}^{n+K}, \mathbf{x}^{n+2K}, ..., \mathbf{x}^{n+lK})$ can be considered as a multiplication of operator $\exp(K\Delta t J_{\mathbf{X}})$ on the Krylov subspace ($\mathbf{x}^{n}$, $\mathbf{x}^{n+K}$, $\mathbf{x}^{n+2K}$, ..., $\mathbf{x}^{n+(l-1)K}$).

Suppose that $q^{\underline{0}}$,$q^{\underline{1}}$,$q^{\underline{2}}$,...,$q^{\underline{l-1}}$ and $q^{\underline{l}}$ is the orthonormal basis of the Krylov subspace spanned by $\mathbf{x}^{n}$, $\mathbf{x}^{n+K}$, $\mathbf{x}^{n+2K}$, ..., $\mathbf{x}^{n+(l-1)K}$ and $\mathbf{x}^{n+lK}$, the Gram-Schmidt orthonormalisation procedure can give us not only a orthonormal basis $q^{\underline{0}}, q^{\underline{1}}, q^{\underline{2}}, ..., q^{\underline{l-1}}$ and $q^{\underline{l}}$, but also QR factorization of the Krylov subspace spanned by $\mathbf{x}^{n}$, $\mathbf{x}^{n+K}$, $\mathbf{x}^{n+2K}$, ..., $\mathbf{x}^{n+(l-1)K}$ and $\mathbf{x}^{n+lK}$. Therefore, we have

$$(\mathbf{x}^{n}, \mathbf{x}^{n+K}, \mathbf{x}^{n+2K}, ..., \mathbf{x}^{n+(l-1)K}, \mathbf{x}^{n+lK}) = (q^{\underline{0}}, q^{\underline{1}}, q^{\underline{2}}, ..., q^{\underline{l-1}}, q^{\underline{l}})R = QR \tag{6.6}$$

and

$$(\mathbf{x}^{n}, \mathbf{x}^{n+K}, \mathbf{x}^{n+2K}, ..., \mathbf{x}^{n+(l-1)K}) = (q^{\underline{0}}, q^{\underline{1}}, q^{\underline{2}}, ..., q^{\underline{l-1}})\tilde{R} = \tilde{Q}\tilde{R} \tag{6.7}$$

where $\tilde{Q}$ contains the first l columns of Q and $\tilde{R}$ is a l-order submatrix of R. Compared to (6.7), (6.6) has one more column and one more line. If we drop the first column of Eq (6.6) and use the relation Eq. (6.5), we get

$$\exp(K\Delta t J_{\mathbf{X}})(\mathbf{x}^{n}, \mathbf{x}^{n+K}, \mathbf{x}^{n+2K}, ..., \mathbf{x}^{n+(l-1)K}) = (q^{\underline{0}}, q^{\underline{1}}, q^{\underline{2}}, ..., q^{\underline{l-1}}, q^{\underline{l}})\overline{R} = Q\overline{R} \tag{6.8}$$

$\overline{R}$ is the submatrix of R with its first column omitted, which has dimension $(l+1) \times l$. As the last line of $\overline{R}$ has only one nonzero term, the diagonal one, denoted $r_{l,l}$, we can recast the relation (6.8) as following:

$$\begin{aligned} &\exp(K\Delta t J_{\mathbf{X}})(\mathbf{x}^{n}, \mathbf{x}^{n+K}, \mathbf{x}^{n+2K}, ..., \mathbf{x}^{n+(l-1)K}) \\ &= (q^{\underline{0}}, q^{\underline{1}}, q^{\underline{2}}, ..., q^{\underline{l-1}})\tilde{\mathbf{H}} + r_{l,l}q^{\underline{l}} = \tilde{Q}\tilde{\mathbf{H}} + \overline{c}q^{\underline{l}} \end{aligned} \tag{6.9}$$

Here the Hessenberg matrix $\tilde{H}$ represents the first l lines of $\overline{R}$. If $\overline{c}$ is small enough, we have

$$\exp(K\Delta t J_{\mathbf{X}})\tilde{Q}\tilde{R} = \tilde{Q}\tilde{H} \tag{6.10}$$

which can be recast as $\exp(K\Delta t J_{\mathbf{X}})\tilde{Q} = \tilde{Q}\tilde{H}\tilde{R}^{-1}$. As $\tilde{R}$ and $\tilde{R}^{-1}$ are upper triangular matrix, $\tilde{H}\tilde{R}^{-1}$ is still a Hessenberg matrix, which is noted as $\mathbf{H}$. So we get the following relation

$$\exp(K\Delta t J_{\mathbf{X}})(q^{\underline{0}}, q^{\underline{1}}, q^{\underline{2}}, ..., q^{\underline{l-1}}) = (q^{\underline{0}}, q^{\underline{1}}, q^{\underline{2}}, ..., q^{\underline{l-1}})\mathbf{H} \tag{6.11}$$

or simply $\exp(K\Delta t J_{\mathbf{X}})\tilde{Q} = \tilde{Q}\mathbf{H}$

If $\mathbf{H}$ is diagonalisable, then $\mathbf{H} = S\Lambda S^{-1}$, where Λ is the diagonal matrix containing the spectrum of $\mathbf{H}$ and S is the matrix formed by the eigenvectors of $\mathbf{H}$. So we have $\exp(K\Delta t J_{\mathbf{X}})\tilde{Q} = \tilde{Q}S\Lambda S^{-1}$, then

$$\exp(K\Delta t J_{\mathbf{X}})\tilde{Q}S = \tilde{Q}S\Lambda \tag{6.12}$$

which shows that Λ, the spectrum of $\mathbf{H}$, corresponds to the spectrum of the matrix $\exp(K\Delta t J_{\mathbf{X}})$, and $\tilde{Q}S$ corresponds to the eigenvectors of $\exp(K\Delta t J_{\mathbf{X}})$. Therefore, the leading eigenvalues of $\mathbf{H}$ can give us those of $\exp(K\Delta t J_{\mathbf{X}})$, which can be easily done by calling the library Lapack.

We use the Arnoldi iteration to compute approximate eigenvalues of the Jacobian matrix $J_{\mathbf{X}}$ using successive time-stepping of the linearized Navier-Stokes equations (6.2). In practice, the linearized unsteady Navier-Stokes equations (6.2) are integrated for a few dozens of time-steps in order to generate a Krylov subspace. Then the Gram-Schmidt orthonormalisation method is applied to construct the Hessenberg matrix $\mathbf{H}$. Once $\mathbf{H}$ obtained, its leading eigenvalues can be calculated by calling the library Lapack. This procedure should be repeated in a time-loop to determine the appropriate dimension of the Krylov subspace and the moment to stop the time-integration. The monotonic decrease of the residual $\overline{c}$, which appears as the last term in Eq. (6.9), serves as a criterion to stop the time-integration.

6.2.2 Results

By using the Arnoldi method, we look for the critical Rayleigh number Ra_{c2} at which the onset of secondary instability in the transverse direction y occurs. In order to allow sufficient interaction between the structures, we choose a domain corresponding to four vertical rolls. 40 Chebyshev modes are used for the spatial discretization in the x-direction, and 160 Fourier modes are used for the vertical direction z as for the 2D DNS in Chapter 3. Convergence test was carried out with another mesh. No significant difference was observed.

The onset of the secondary instability leads the 2D flow to a 3D steady state as stated in the literature [31, 32, 33]. We wish to determine the critical Rayleigh number Ra_{c2} at which the secondary instability occurs and the corresponding critical wavenumber k_{yc} associated with the steady 3D structure beyond Ra_{c2}. As mentioned before, once the base flow is obtained, the Arnoldi method is applied to compute the stability of the base flow. At a given wavenumber k_{yi}, the code is run for different Ra_j. Each run yields several leading eigenvalues. The real part of the first leading eigenvalue σ_{ij} detemines the stability of the mode k_{yi} at Ra_j. As σ_{ij} increases almost linearly with Ra_j, linear extrapolation can be used to find the critical Rayleigh number Ra_{c2i}. Then the procedure is repeated for a range of k_{yi} to calculate the corresponding Ra_{c2i}. The neutral curve can be obtained by plotting Ra_{c2i} as a function of k_{yi} as shown in Figures 6.3 and 6.4. Results are presented here for two configurations: $A_z = 9$ and $A_z = 10$.

Case $A_z = 9$ ($k_z = 2.79$)

For the case $A_z = 9$, the wavenumber associated with the primary instability (2D rolls) is $k_z = 2.79$, which is very close to the critical wavenumber $k_{zc} = 2.81$. Ra_{c2} is found to be 6056, and $k_{yc} = 1.6$ (see figure 6.3), and σ is real so the most unstable mode is stationary. This agrees well with previous results [31, 32]. The value of k_{yc} appears to correspond to that associated with monotone instability A.

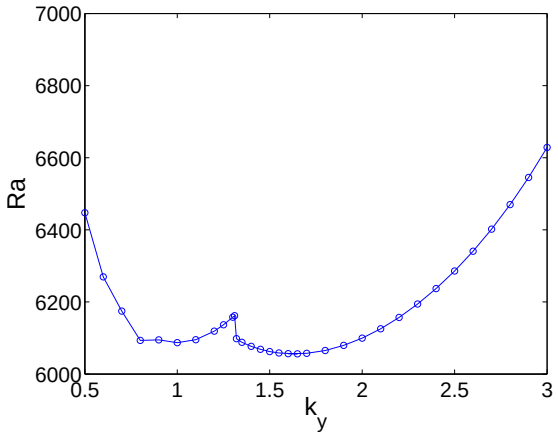

Figure 6.3: Neutral curve, $\sigma(Ra_{c2i}) = 0$ as a function of the wavenumber k_y, $A_z = 9$

Case $A_z = 10$ ($k_z = 2.51$)

For the case $A_z = 10$, we have $k_z = 2.51$. The neutral curve is shown in Figure 6.4. The critical Rayleigh number is found to be $Ra_{c2} = 6033$, and the critical spanwise wavenumber k_{yc} is equal to 0.78. This also corresponds to a stationary mode, and the value of the wavenumber is more consistent with the monotone instability B of Chait and Korpela [32].

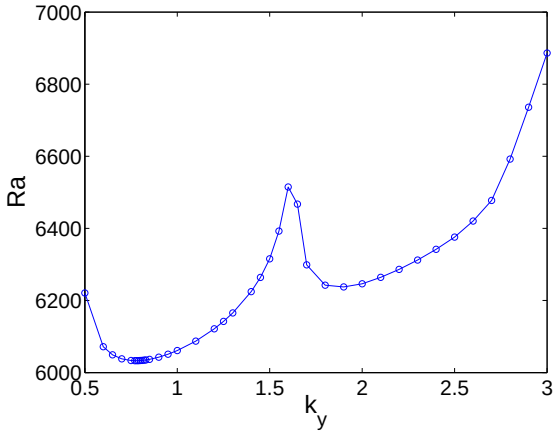

Figure 6.4: Neutral curve, $\sigma(Ra_{c2i}) = 0$ as a function of the wavenumber k_y, $A_z = 10$

Comparison of the two figures shows the presence in both cases of two similar lobes with two local minima around $k_y \sim 1.6$ and $k_y \sim 0.8$. Each minimum appears to correspond to a different instability mechanism (A and B). The minimal Rayleigh values associated with each lobe are close for $A_y = 9$ ($k_z = 2.8$) but the absolute minimum (critical Rayleigh number) is

associated with the higher wavenumber, while it corresponds to the lower wavenumber in the case $A_y = 10$ ($k_z = 2.5$).

The nature of the most unstable mechanism is therefore quite sensitive to the exact value of the wavenumbers allowed in both the vertical and transverse directions. Moreover, since the growth rate of each instability is relatively close, competition between the different mechanisms is likely to take place. This will be examined in more detail using nonlinear simulations in the next section.

6.3 Nonlinear simulations $A_y = 8$ & $A_y = 9$

6.3.1 Characteristics of the simulations

In this section, we use DNS to study the sequence of bifurcations and route to temporal chaos of the flow. As in the previous chapters, the physical domain contains four vertical rolls i.e $A_z \sim 8 - 10$. We now choose a large enough spanwise dimension for the plate to include critical spanwise wavelengths, which requires $A_y \sim 8 - 10$ as well. To simulate such domains, we used 40 and 160 Chebyshev modes for the spatial discretizations in the directions x and z, respectively, and 130 Fourier modes for the y-direction. The initial condition is taken as the base flow Eq. (3.1) in all cases. The time required for the flow to converge is about 10000 convective time units, which represents about 200 hours on the super-cluster ADA in IDRIS-CNRS with 8 processors. Due to the computing cost of such a configuration, the number of test cases is limited. Only one configuration $A_y = 8$ and width $A_z = 9$ is considered. For the chosen wavenumber $k_y = 1.57$, $k_z = 2.79$, which is very close to the critical wavenumber, linear stability results predict that mode A should be observed at $Ra > Ra_c = 6056$. Calculations were therefore carried out at $Ra = 6050, 6070, 6080, 6100, 6150, 6180, 6200, 6250$ and 6300. We only show results for the four cases $Ra = 6050, 6100, 6150, 6250, 6300$ (represented with circles of different colours in Figure 6.2) which present original features.

6.3.2 $Ra_c = 5708 < Ra < Ra_{c2} = 6056$: 2D steady rolls

As seen earlier, the first bifurcation is a supercritical pitchfork bifurcation. For comparison purposes with higher Rayleigh numbers, Figure 6.5 obtained for $Ra = 6050$ shows that the 2D flow consists of four steady co-rotating rolls. As mentioned in Chapter 3 and 4, the vertical translation invariance is replaced with a D_4 symmetry, and the centro-symmetry due to the Boussinesq approximation is conserved.

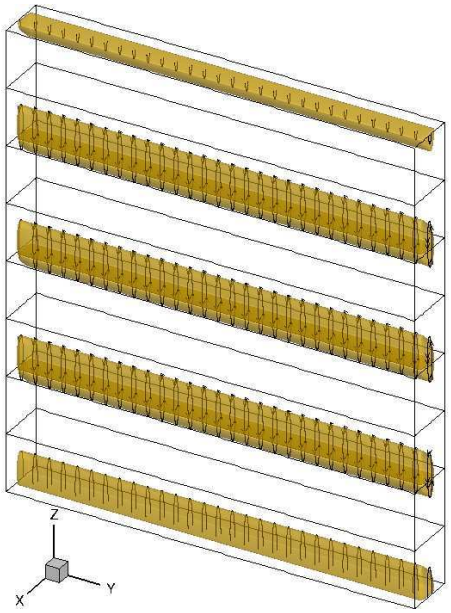

Figure 6.5: Isosurface of Q-criterion $Q = 0.1$ and streamlines, $Ra = 6050$.

6.3.3 $Ra = 6100 > Ra_{c2}$: Transient 3D steady pattern

The timeseries of the temperature measured at the point (0.0381, 0.122, 4.96), located in the hot boundary layer, is plotted in Figure 6.6 (a). Three different states can be identified from the original conduction state. A first plateau corresponding to 2D rolls is observed for some time, then the flow becomes three-dimensional.

3D pattern associated with instability A: wavy rolls

An enlargement of the temperature signal for the times $4000 < t < 5500$ is represented in logarithmic scale in Figure 6.6 (b). The amplitude of temperature disturbance grows exponentially

for $4000 < t < 4500$, which corresponds to the linear growth rate of the most unstable eigenmode, then increases at a lower rate for $t > 4700$ before the perturbation amplitude satures. By using the same argument [60] as was used in section 3.5.1, this evolution shows that the coefficient of the cubic term in the normal form of the pitchfork bifurcation is negative, therefore this bifurcation is supercritical. Again, it is also a circle bifurcation owing to the invariance of the equations with respect to transverse translations.

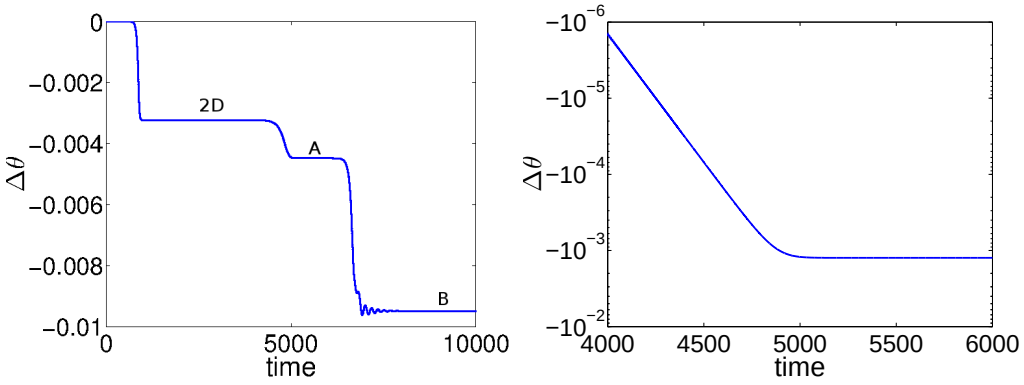

(a) (b)

Figure 6.6: (a): Time series of temperature at point (0.0381, 0.122, 4.96) in the boundary layer near the hot wall at $Ra = 6100$; (b): An enlargement of (a) for $4000 < t < 5500$ on a logarithmic scale.

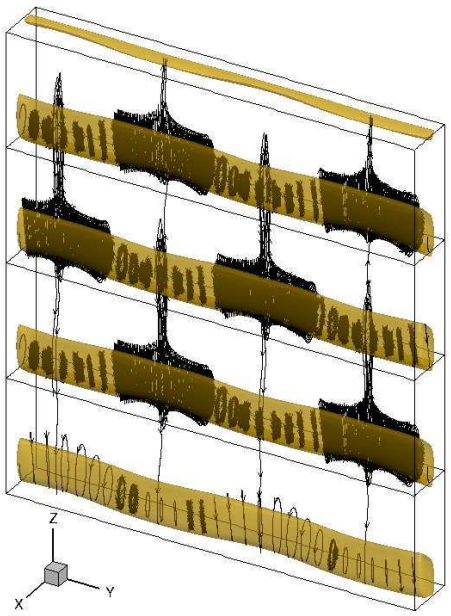

Figure 6.7: Isosurface of Q-criterion $Q = 0.1$ and streamlines, at $t = 6000$, $Ra = 6100$.

Chait and Korpela's stability analysis predicts that instability A consisting of steady, wavy rolls with $k_y = 1.6$ and $k_z = k_{zc}/2$ should be observed. This is supported by our results as we found the most unstable spanwise mode to be $k_y = 1.6$. Examination of the flow for the second plateau confirms this conjecture. The flow structure of this 3D pattern consists of 4 steady corotating rolls with a wavy distortion in the transverse direction, which represents a $D_2 \times D_4$ symmetry. As can be seen in Figure 6.7, at the location of a "pinch", the streamlines escape from a roll to join the adjacent roll above it. This connection between the rolls is somewhat similar to the vortex-pairing observed in the mixing layer [62], which is also a subharmonic instability. Figure 6.8 represents the 2D streamline plots on four different vertical planes and shows the distortion of the rolls in both the vertical and the transverse directions. Owing to the wavy motion, the center of the rolls varies in the vertical direction, but the size of the rolls remains more or less constant.

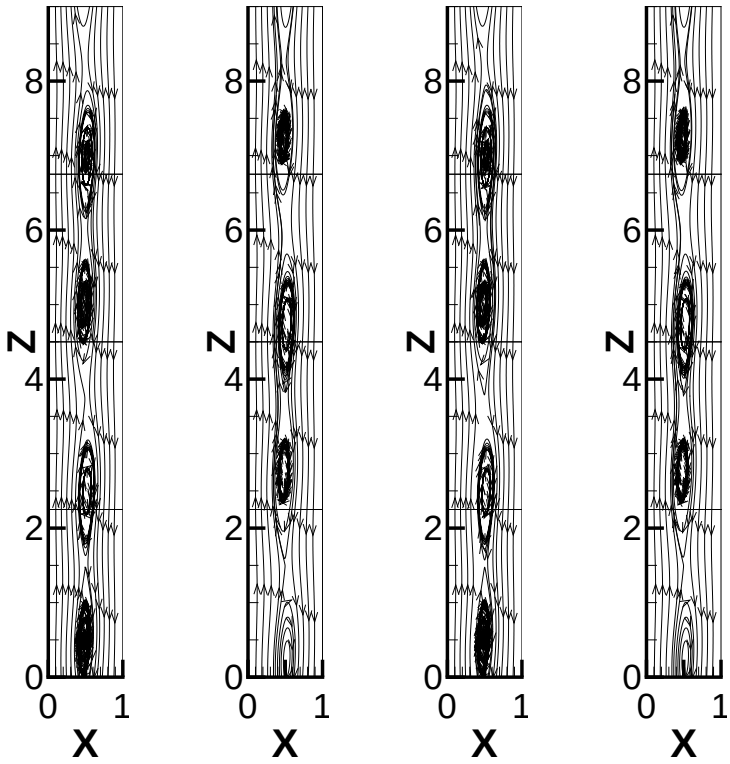

(a) $y = 0.977$ (b) $y = 2.931$ (c) $y = 4.947$ (d) $y = 6.982$

Figure 6.8: Streamlines at different vertical planes, $t = 6000$, $Ra = 6100$.

The temperature contour on the vertical plane $x = 0.0381$ is represented in Figure 6.9

(a). We checked that similar remarks to those described below could be made if we considered any other vertical plane. The corresponding spatial spectrum $\hat{\theta}(i_y, i_z)$ where j and k are the indices of the spanwise y and vertical z wavenumbers is shown in Figure 6.9 (b). It can be seen that $\hat{\theta}(0,4)$, $\hat{\theta}(2,2)$, which respectively represent the 2D rolls and the wavy distortion, are the principal modes constituting the pattern.

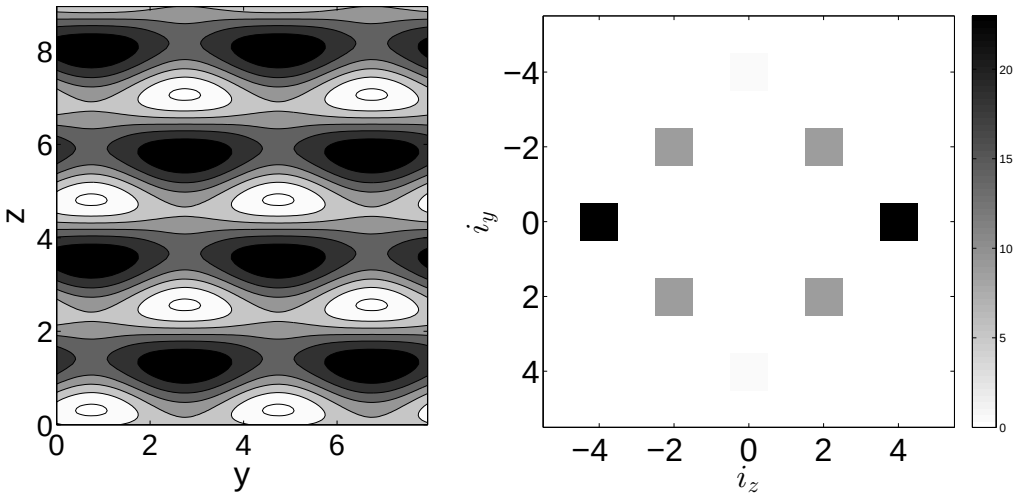

(a) (b)

Figure 6.9: (a) The temperature contour on the vertical plane $x = 0.0381$, (b) the corresponding 2D Fourier modes $|\hat{\theta}(i_y, i_z)|$ $(i_y, i_z = -5, 5)$ for the fluctuations, $t = 6000$, $Ra = 6100$.

Second steady 3D pattern

As can be seen in Figure 6.6 (a), the temperature perturbation with respect to the base flow shifts from the second plateau, which corresponds to the pattern of monotone instability A, to a third plateau at $t \sim 7000$. The local oscillation of timeseries in Figure 6.6 (a) at $t \sim 7000$ suggests the instability is subcritical. The final flow pattern is shown in Figure 6.10. Although remains of pattern A are still present, the dominant feature of the flow consists of transverse rolls with streamline excursions over a single, limited portion of its spanwise extent - which we will call the defect. The defects form an oblique line in the (x, z) plane. The orientation of the oblique line can be either from the top-right to the bottom-left or from the top-left to the bottom right, because of the invariance of the system (1.1-1.4) under reflection symmetry with respect to any plane $y = cst$. The spanwise extent of each defect is about one (inter-plate

distance) and it typically involves three vertical structures.

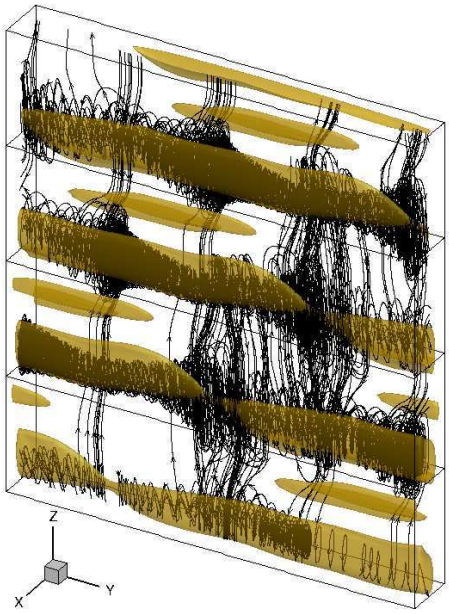

Figure 6.10: Isosurface of Q-criterion $Q = 0.1$ and streamlines for the flow pattern B, at $t = 9000$, $Ra = 6100$. Some streamlines associated with the lowest roll cannot be represented due to a limitation of the graphics package.

The symmetry of the new solution is $D_1 \times D_4$. Figure 6.11 represents the flow streamlines on four selected vertical planes. The rolls remain aligned in the transverse direction y, but the size of the rolls varies along the transverse direction y (compared this with Figure 6.8).

The temperature field on the vertical plane $x = 0.0381$ is represented in Figure 6.12 (a), and its corresponding 2D Fourier spectrum at $t = 8000$ in Figure 6.12 (b), which confirms that the principal modes associated with the pattern are $\hat{\theta}(0, 4)$ and $\hat{\theta}(1, -1)$. Since the equations (1.1)-(1.4) are invariant by reflection with respect to any plane $y = cst$, the modes $\hat{\theta}(1, -1)$ and $\hat{\theta}(1, 1)$ are equivalent solutions. For simplicity, we mention the modes only with the positive indices in the text. The mode $\hat{\theta}(1, 1)$ shows that this 3D pattern involves the smallest spanwise wavenumber allowed by the domain and appears to correspond to the instability B described by Chait and Korpela [32], as a skewed varicose instability, in which the rolls are thickening and thinning in the transverse direction. Note that the coupling between the pure roll mode $\hat{\theta}(0, 4)$ and transverse instability mode $\hat{\theta}(1, -1)$ is relatively strong, as the energy of mode $\hat{\theta}(1, 3)$ is substantial.

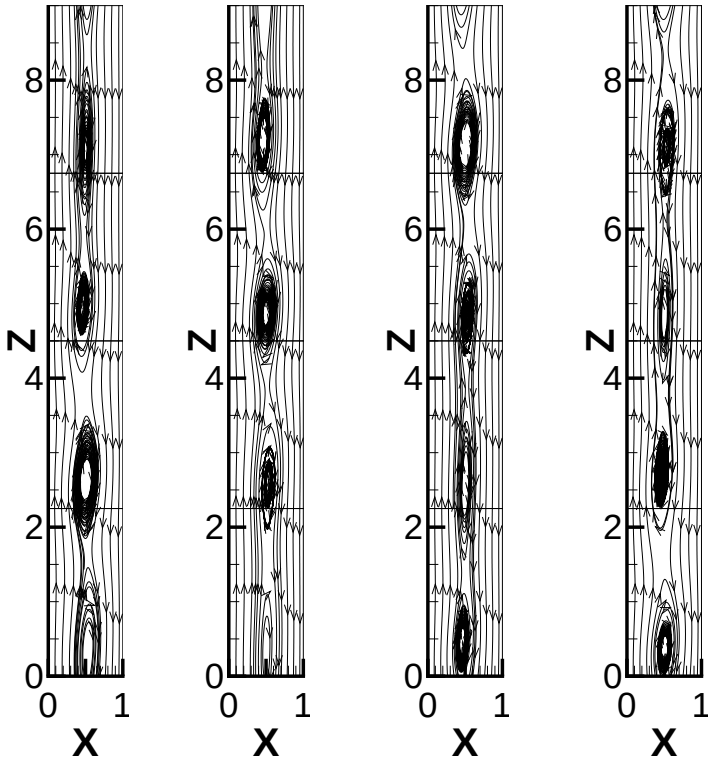

(a) $y = 0$ (b) $y = 1.954$ (c) $y = 4.031$ (d) $y = 6.046$

Figure 6.11: Streamlines on different vertical planes, $t = 8000$, $Ra = 6100$.

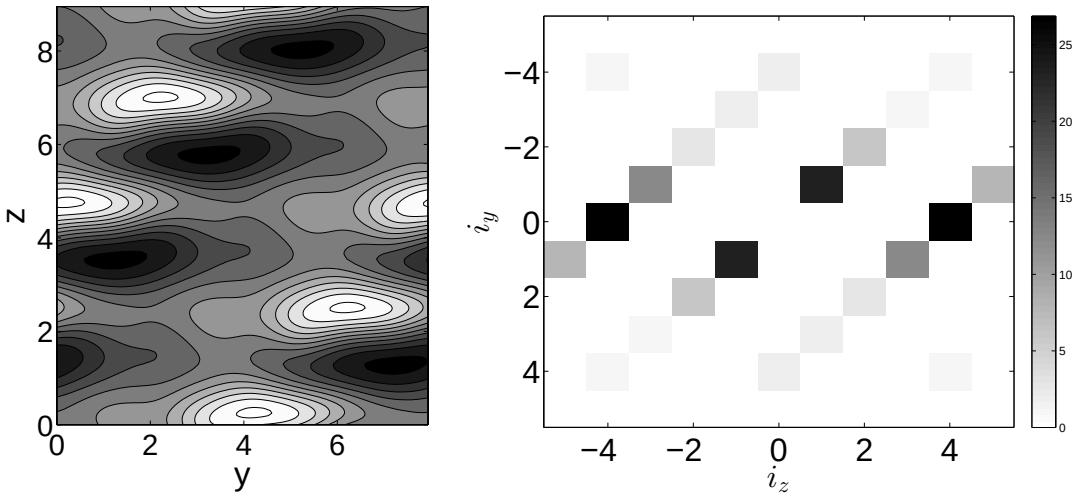

(a) (b)

Figure 6.12: (a) The temperature contours in the vertical plane $x = 0.0381$, (b) the corresponding spatial 2D Fourier mode $|\hat{\theta}(i_y, i_z)|$ $(i_y, i_z = -5, 5)$ for the fluctuations, $t = 8000$, $Ra = 6100$.

Although the Rayleigh number of the configuration is very close to the critical Rayleigh of instability A, it seems that mode A is already unstable to instability B. A simulation with pattern A obtained at $Ra = 6100$ as the initial condition was performed, when Ra was decreased to $Ra = 6060$ (quite close to $Ra_{c2} = 6056$), the asymptotic state obtained was also pattern B. This suggests us that the pattern A predicted by the linear stability analysis seems to be always unstable to the pattern B through a subcritical instability. Since we were not able to carry out simulations for intermediate Rayleigh numbers, we can also conjecture the existence of a small Rayleigh domain over which modes A and modes B coexist. We therefore suspect the presence of a cusp bifurcation involving three equilibria: the straight (2D) rolls, the wavy rolls (A) and the defect rolls (B) as well.

6.3.4 $6150 \leq Ra \leq 6200$: 3D time-dependent flow

The 3D pattern becomes time-dependent when Ra is increased to 6150. The temperature timeseries at the point (0.0381, 0.122, 4.96) in the boundary layer near the hot wall is plotted in Figure 6.13 (a). Figure 6.13 (b) shows that it corresponds to a periodic signal of frequency $f_1^{Large} = 0.00536$, which is much lower than $f_1 = 0.036$ found in Chapter 4 for a constrained configuration. Identification of a similar frequency at $Ra = 6180$ and $Ra = 6200$ leads us to conjecture that this is a Hopf bifurcation.

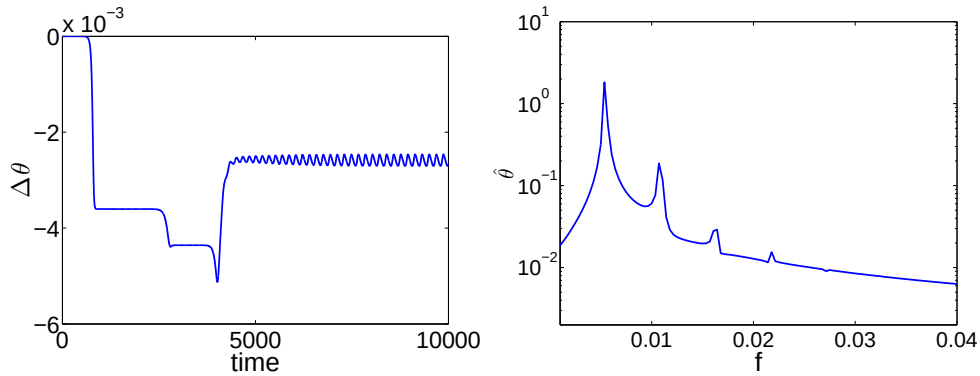

(a) (b)

Figure 6.13: (a): Time series of temperature at the point (0.0381, 0.122, 4.96) in the boundary layer near the hot wall, $Ra = 6150$ (b): Temporal Fourier spectrum of the periodic portion $t \in [8000, 10000]$ of the signal (a).

Figure 6.14 represents the flow structures at two different instants. The flow structures consist of 4 corotating rolls with a defect, as can be seen in Figure 6.14 (a). In Figure 6.14 (b), the discontinuities of criterion-Q isosurface disappear, which indicates that the defect region shrinks. The periodic oscillation is characterized by the growth and shrink of the defect associated with streamline excursions.

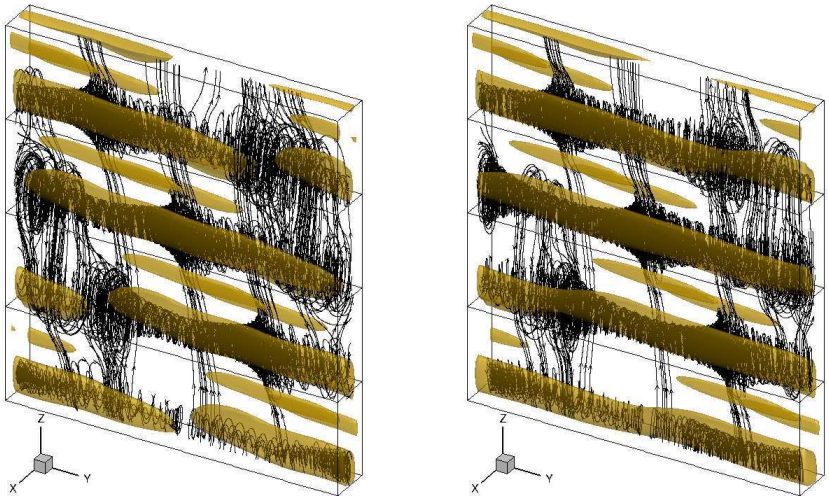

(a) $t = 8770$ (b) $t = 8850$

Figure 6.14: Flow structures at two different instants: iso-surface of Q-criterion $Q = 0.1$ and streamlines, $Ra = 6150$.

The temperature contours on the vertical plane $x = 0.0381$ at different instants are represented in Figure 6.15 (left). The corresponding Fourier spectra are shown in Figure 6.15 (right). Besides the spanwise invariant mode $\hat{\theta}(0, 4)$ and a trace of the wavy mode A $\hat{\theta}(2, 2)$ we can see the presence of a new mode $\hat{\theta}(1, 1)$ in the pattern, and its interaction with the mode $\hat{\theta}(0, 4)$.

The temporal evolution of the principal modes $\hat{\theta}(0, 4)$, $\hat{\theta}(1, 1)$ are shown in Figure 6.16. These two modes oscillate periodically. The mode $\hat{\theta}(0, 4)$ corresponding to the primary rolls has an almost constant amplitude, while the mode $\hat{\theta}(1, 1)$ has a significant amplitude variation. These two modes represent 84.17% of the total energy for the perturbations.

6.3.5 $Ra = 6250$: Period-doubling bifurcation

The temporal behavior of the flow is modified when Ra is further increased to $Ra = 6250$. The timeseries of the temperature perturbation at the point (0.0381, 0.122, 4.96) is shown in

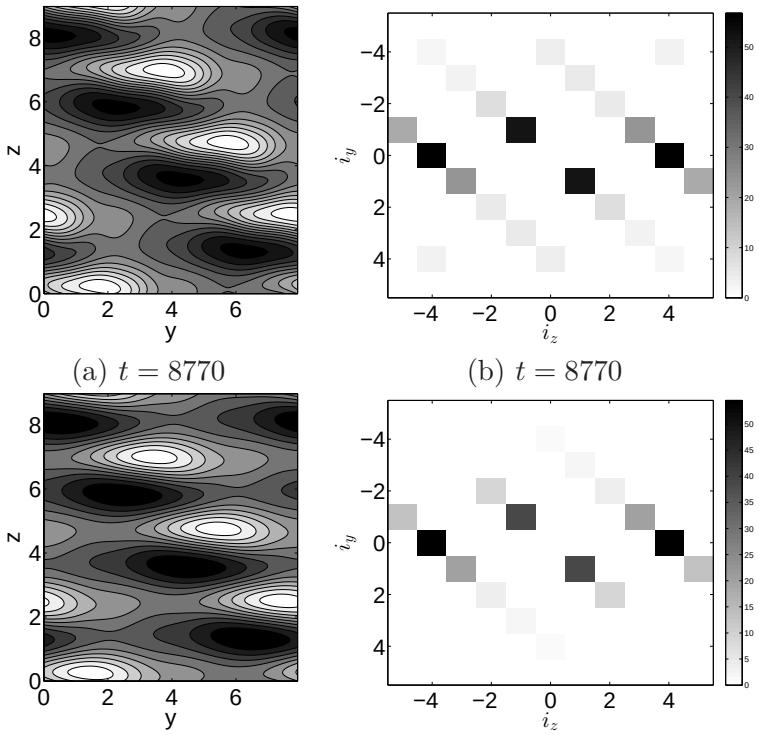

(a) $t = 8770$ (b) $t = 8770$

(c) $t = 8850$ (d) $t = 8850$

Figure 6.15: Left column: the temperature contours on the vertical plane $x = 0.0381$, Right column: corresponding spatial 2D Fourier modes $|\hat{\theta}(i_y, i_z)|$ $(i_y, i_z = -5, 5)$ for the fluctuations, $Ra = 6150$.

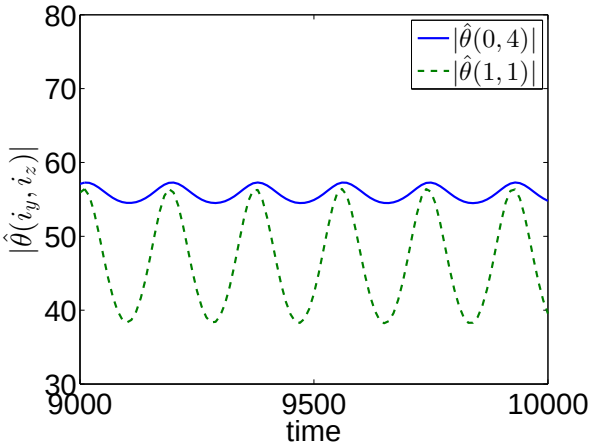

Figure 6.16: Temporal evolution of the spectral coefficients $|\hat{\theta}(i_y, i_z)|$ on the plane $x = 0.0381$ for two principal modes: $Ra = 6150$

Figure 6.17 (a). The Fourier spectrum of the periodic portion $t \in [5000, 8000]$ in Figure 6.17 (b) shows that the largest amplitude is located at the frequency $f_1^{Large} = 0.00536$, which is identical to that found in the previous subsection 6.3.4 at $Ra = 6150$, while the second largest amplitude corresponds to the frequency $f_{1/2}^{Large} = 0.00286 \sim f_1^{Large}/2$.

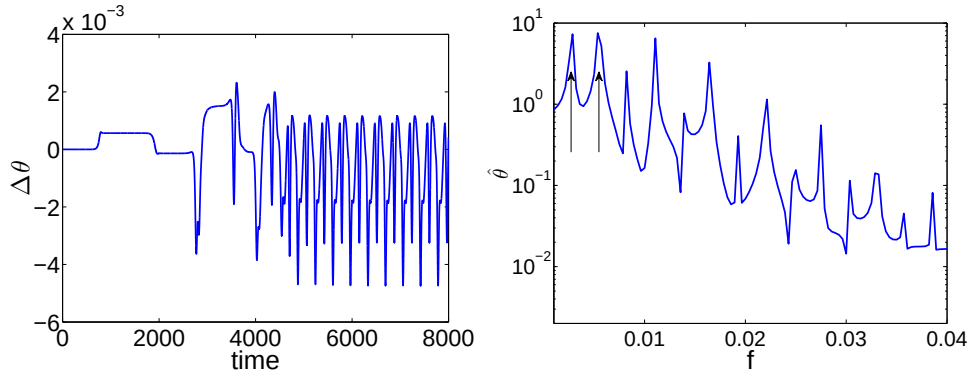

(a) (b)

Figure 6.17: (a): Time series of temperature perturbation at the point (0.0381, 0.122, 4.96) in the boundary layer near the hot wall, $Ra = 6250$. (b): Temporal Fourier spectrum of the periodic portion $t \in [5000, 8000]$ of the signal (a).

The topology of the flow again consists of 4 rolls which are distorted in the transverse direction. The evolution of the flow structure during an oscillation period (which is twice as large as the previous case $Ra = 6150$) is represented in Figure 6.18. Comparing Figures 6.18 (a) and (d), we can see that the positions of defects are shifted about half a wavelength $A_y/2$ in the y-direction for half of doubled-period. Then they return to their original positions after another half doubled-period.

The temperature contours on the vertical plane $x = 0.0381$ and corresponding spatial Fourier spectrum at the same instants of Figure 6.18 are represented in Figures 6.19 and 6.20. The principal modes are $\hat{\theta}(0, 4)$, $\hat{\theta}(2, 2)$, $\hat{\theta}(1, 1)$ are present as well as the mode $\hat{\theta}(1, 3)$. The latter results from the interaction between the modes $\hat{\theta}(0, 4)$ and $\hat{\theta}(1, 1)$. This behavior suggests that the pattern dynamics is a superimposition or competition of the modes associated with both monotone instabilities A and B. The three principal modes and the mode $\hat{\theta}(1, 3)$ represent respectively 84.87% and 7.37% of the energy of the perturbations, thus these four modes together contribute 92.24% of the perturbation energy.

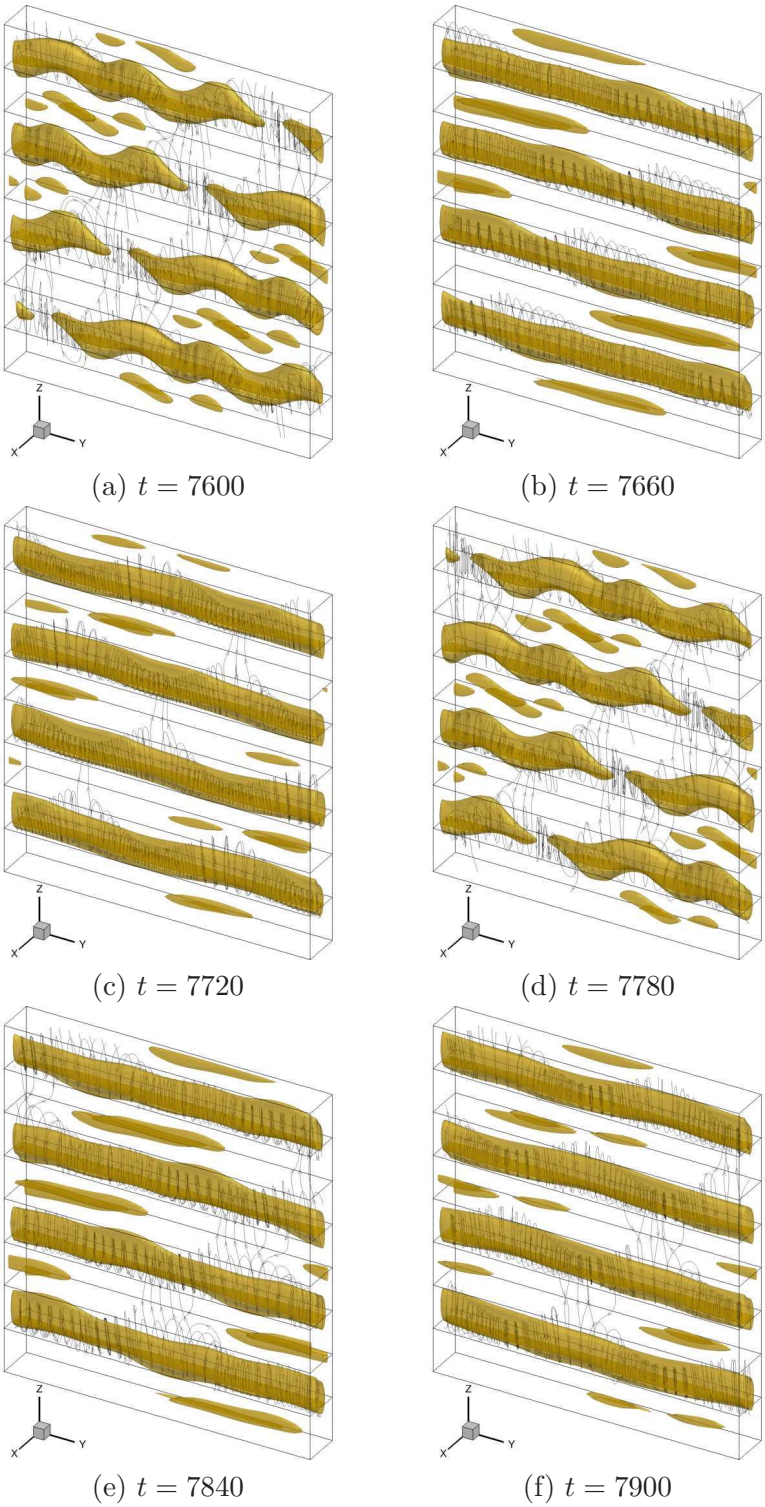

(a) $t = 7600$ (b) $t = 7660$

(c) $t = 7720$ (d) $t = 7780$

(e) $t = 7840$ (f) $t = 7900$

Figure 6.18: Flow structures at different instants spanning one temporal oscillation: iso-surface of Q-criterion $Q = 0.1$ and streamlines, $Ra = 6250$.

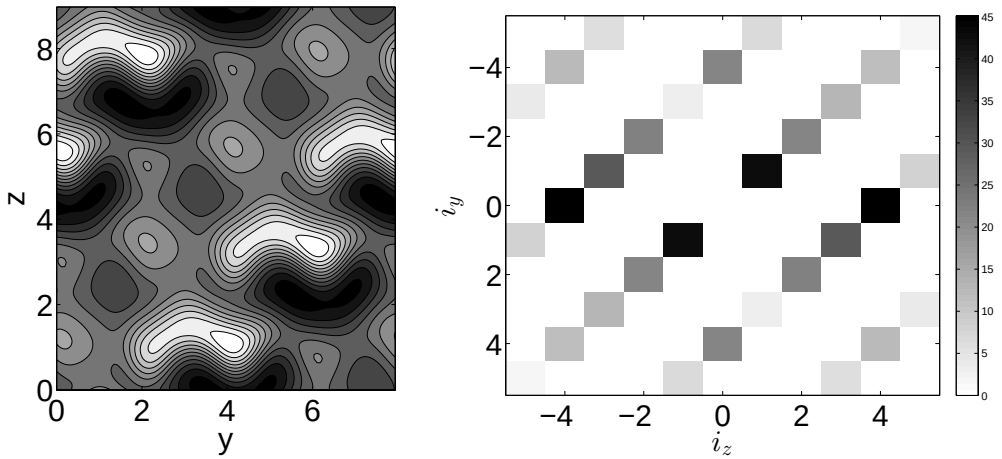

(a) $t = 7600$ (b) $t = 7600$

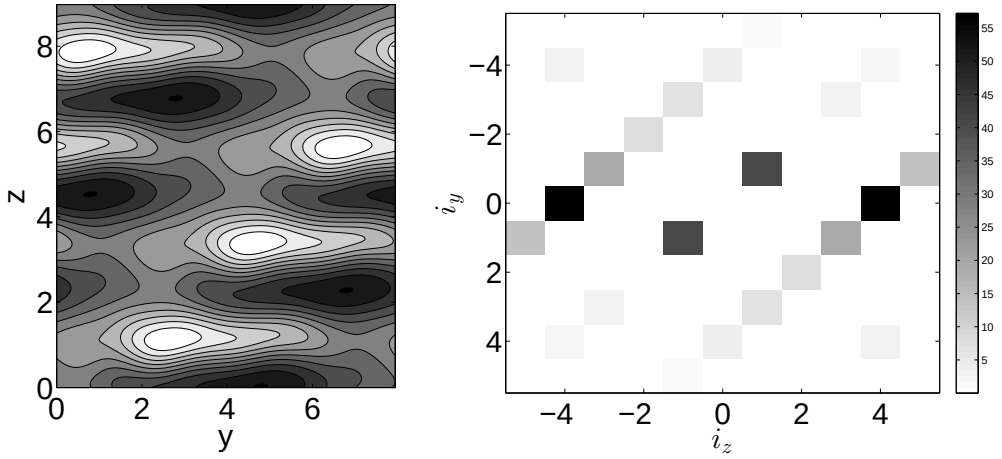

(c) $t = 7660$ (d) $t = 7660$

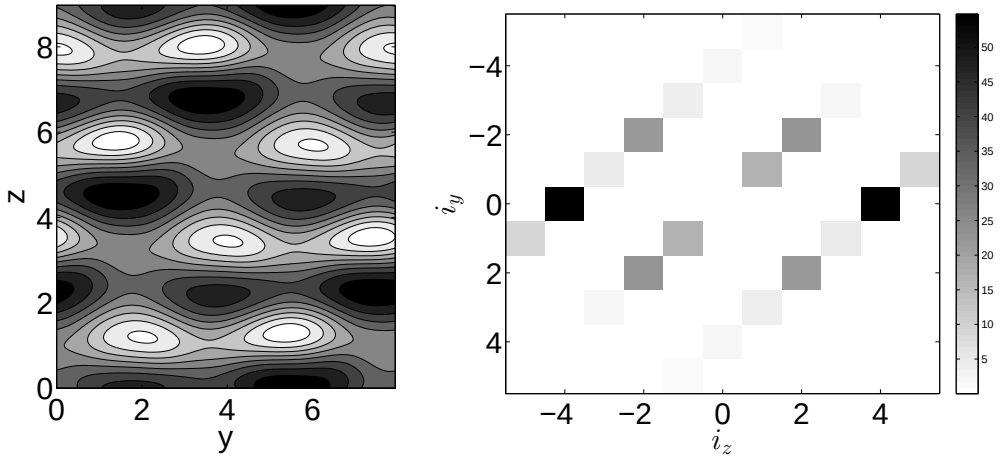

(e) $t = 7720$ (f) $t = 7720$

Figure 6.19: Left column: the temperature contours on the vertical plane $x = 0.0381$; Right column: the corresponding spatial Fourier modes $|\hat{\theta}(i_y, i_z)|$ $(i_y, i_z = -5, 5)$ for the fluctuations, $Ra = 6250$. (to be continued in Figure 6.20)

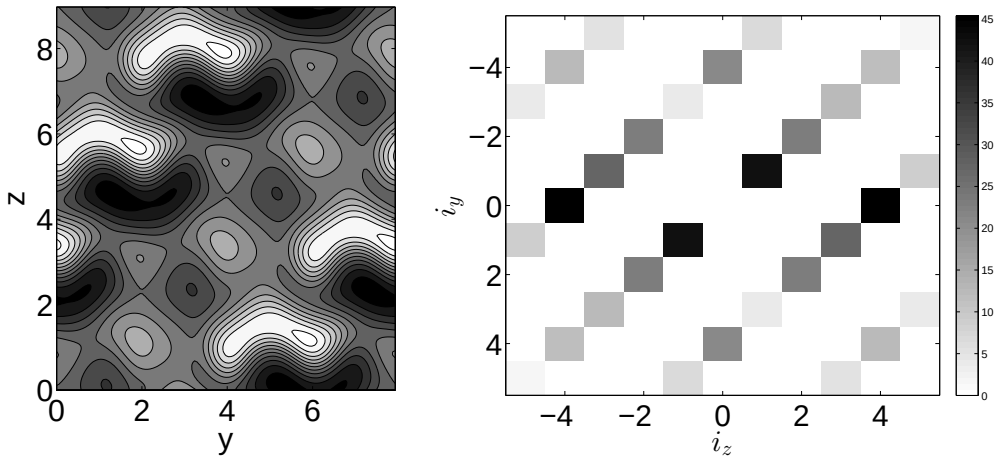

(a) $t = 7780$ (b) $t = 7780$

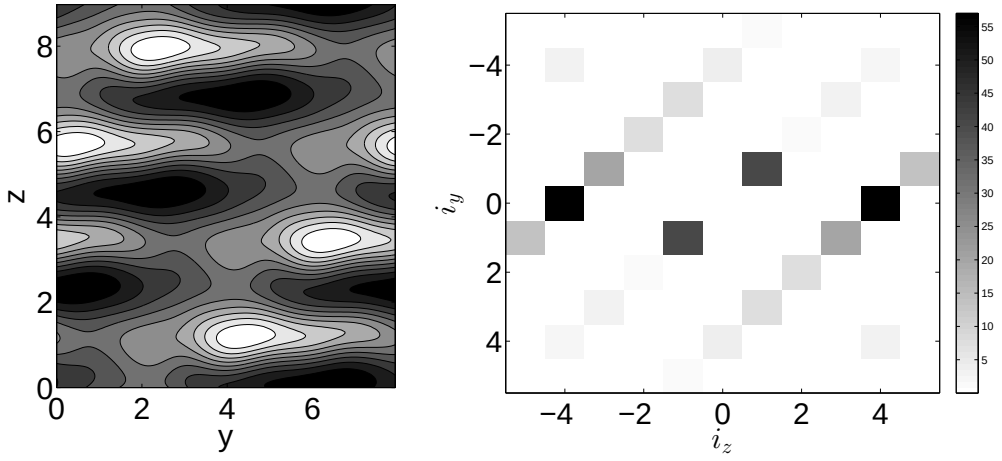

(c) $t = 7840$ (d) $t = 7840$

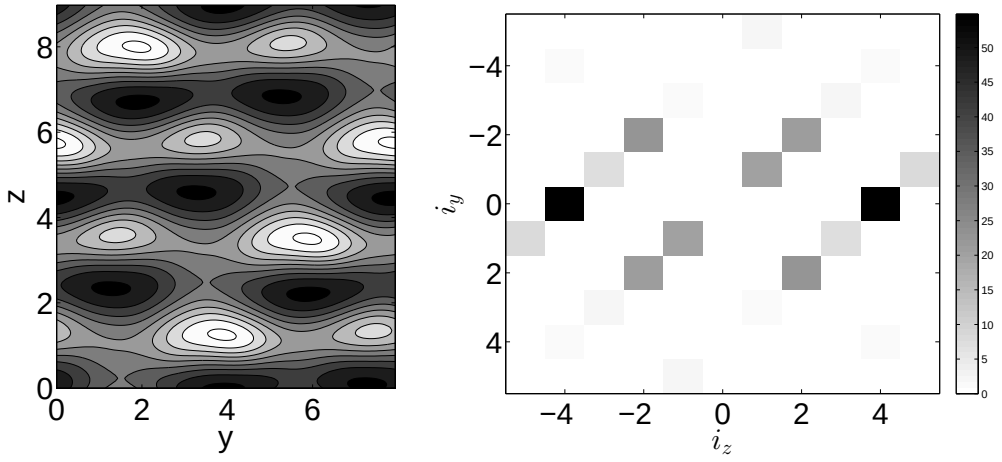

(e) $t = 7900$ (f) $t = 7900$

Figure 6.20: Left column: the temperature contours on the vertical plane $x = 0.0381$; Right column: the corresponding spatial Fourier mode $|\hat{\theta}(i_y, i_z)|$ $(i_y, i_z = -5, 5)$ for the fluctuations, $Ra = 6250$.

The temporal evolution of the principal modes $\hat{\theta}(0,4)$, $\hat{\theta}(2,2)$, $\hat{\theta}(1,1)$ are shown in Figure 6.21. All three modes oscillate periodically. The mode $\hat{\theta}(0,4)$ corresponding to the primary rolls has the largest amplitude. The mode $\hat{\theta}(1,1)$ corresponding to instability mechanism B has the second largest amplitude. The mode $\hat{\theta}(1,3)$ representing the interaction of mode $\hat{\theta}(0,4)$ and $\hat{\theta}(1,1)$ has almost the same amplitude as the mode $\hat{\theta}(2,2)$, which describes the wavy structures of the rolls associated with mechanism A. The mode $\hat{\theta}(0,4)$ oscillates almost in phase opposition with respect to the other modes. The mode $\hat{\theta}(1,3)$ and $\hat{\theta}(1,1)$ oscillate almost in phase, while between $\hat{\theta}(2,2)$ and $\hat{\theta}(1,1)$, there is a small phase shift about 1/8 of the doubled time-period.

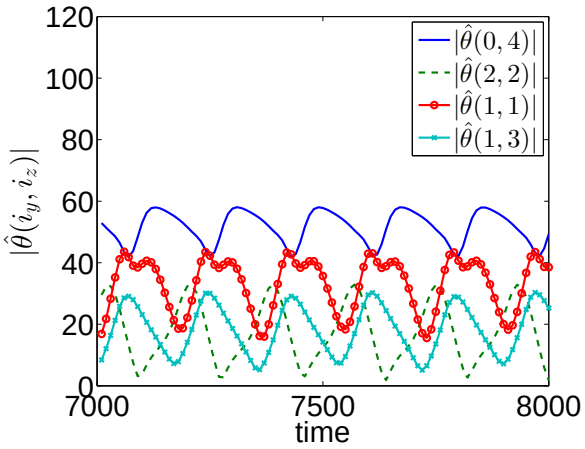

Figure 6.21: Temporal evolution of the spectral coefficients $|\hat{\theta}(i_y, i_z)|$ on the plane $x = 0.0381$ for four modes: $Ra = 6250$

6.3.6 $Ra \geq 6300$: Temporal chaos

When Ra is increased to $Ra = 6300$, the flow becomes temporally chaotic, as shown by the temperature timeseries at the point (0.0381, 0.122, 4.96) in Figure 6.22 (a). The corresponding Fourier transform of the signal $t \in [5000, 8000]$ is quasi-continuous, as can be seen in Figure 6.22 (b).

The evolution of the flow structure becomes more complex, as shown in Figures 6.23 and 6.24. The four unsteady distorted rolls are still the principal structures. For intermittent periods of time, the flow appears to be essentially 2D as can be seen in Figures 6.23 (a) (f) and 6.24 (d), but in general the flow structure is strongly 3D as can be seen in Figures 6.23 (d) (e) and

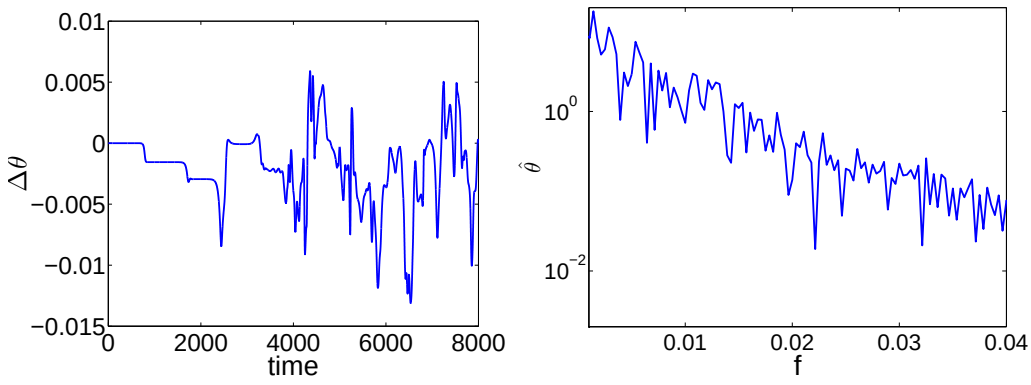

(a) (b)

Figure 6.22: (a): Timeseries of temperature perturbation at the point (0.0381, 0.122, 4.96) in the boundary layer near the hot wall, $Ra = 6300$ (b): Temporal Fourier spectrum of the chaotic portion $t \in [5000, 8000]$ of the signal (a).

6.24 (c). Pattern A is seen to be dominant at times (Figures 6.23 (b) and 6.24 (b)).

The time-averaged 2D Fourier spectral coefficients $|\hat{\theta}(i_y, i_z)|$ of the temperature distribution on the vertical plane $x = 0.0381$ for $t \in [7000, 8000]$ is represented in Figure 6.25 (a). It shows that the principal modes are still $\hat{\theta}(0,4)$, $\hat{\theta}(2,2)$, $\hat{\theta}(1,1)$. The three principal modes represent 78.75% of the total energy of the perturbations. The mode $\hat{\theta}(1,3)$ representing the interaction between the mode $\hat{\theta}(0,4)$, $\hat{\theta}(1,1)$ becomes significant. With $\hat{\theta}(1,3)$, these four modes contribute 87.81% of the total perturbation energy. This confirms that the spatial organization of the flow is still very strong and limited to only a few wavenumbers corresponding to a combination of instability mechanisms. The temporal evolution of these four principal modes is chaotic, as shown in Figure 6.25 (b).

6.4 Conclusion

The goal of this chapter is to examine how temporal chaos develops in larger configurations. Previous linear stability results have indicated that the 2D rolls characterized by a wavenumber k_z are unstable to two kinds of 3D steady disturbances: one corresponding to a vertical pairing of the rolls with a transverse modulation (instability A, wavy modes) and one consisting of a periodical thickening and thinning of the rolls (instability B, roll defect modes). We use an

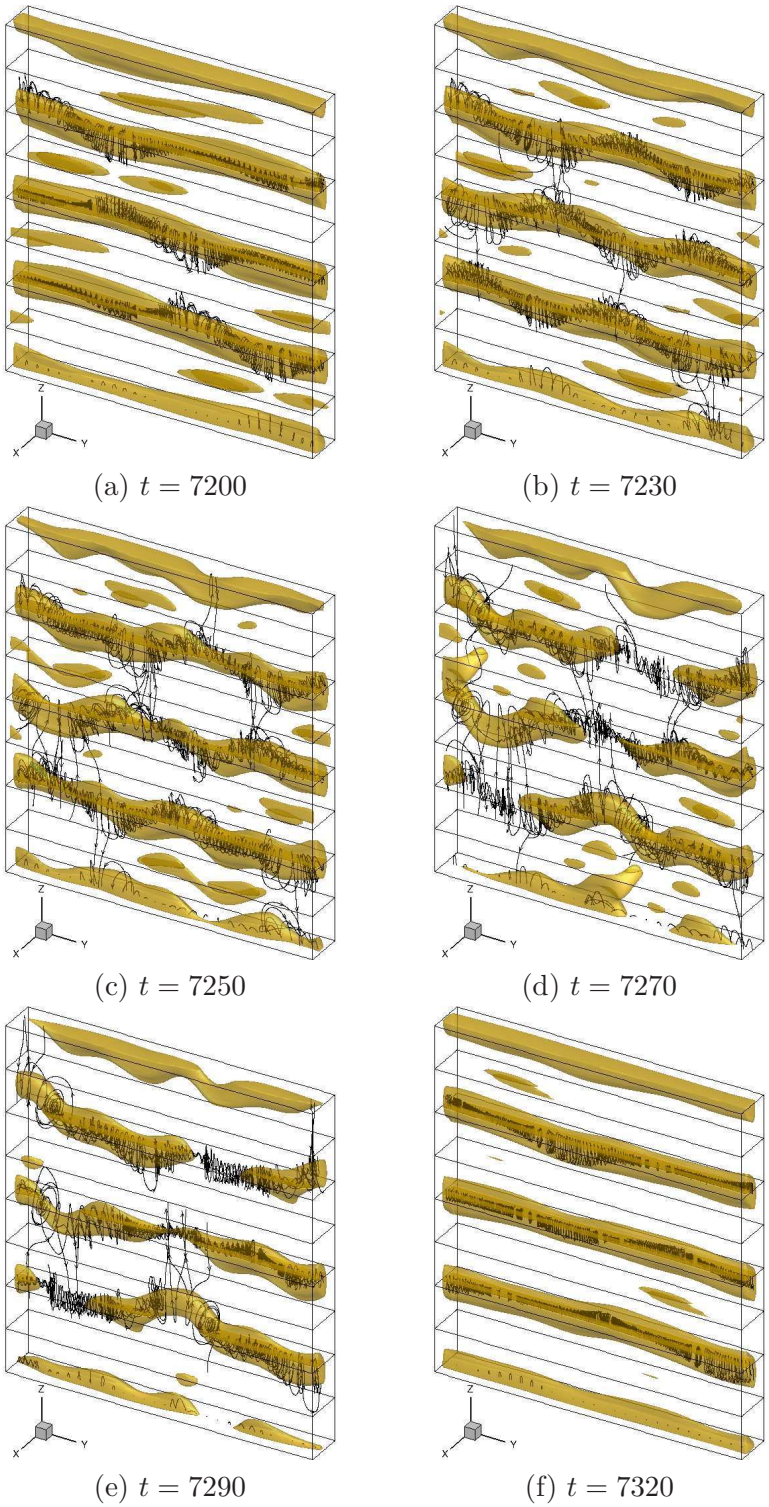

(a) $t = 7200$ (b) $t = 7230$

(c) $t = 7250$ (d) $t = 7270$

(e) $t = 7290$ (f) $t = 7320$

Figure 6.23: Flow structures at different instants: iso-surface of Q-criterion $Q = 0.1$ and streamlines, $Ra = 6300$. (to be continued in Figure 6.24)

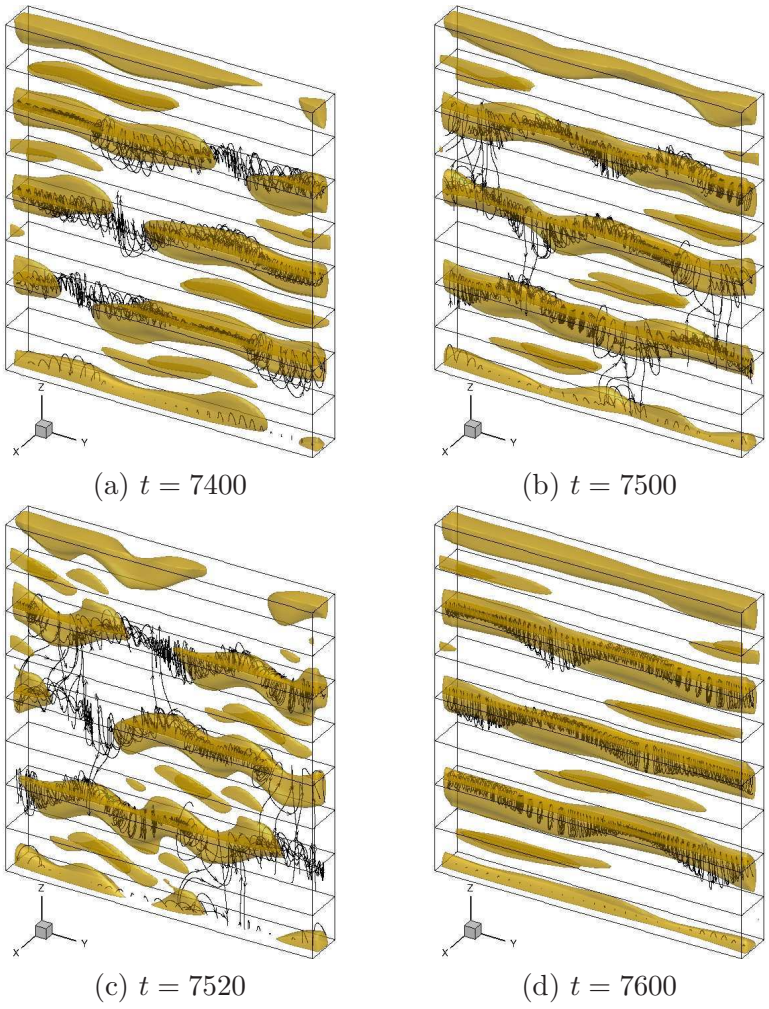

(a) $t = 7400$ (b) $t = 7500$

(c) $t = 7520$ (d) $t = 7600$

Figure 6.24: Flow structures at different instants: iso-surface of Q-criterion $Q = 0.1$ and streamlines, $Ra = 6300$.

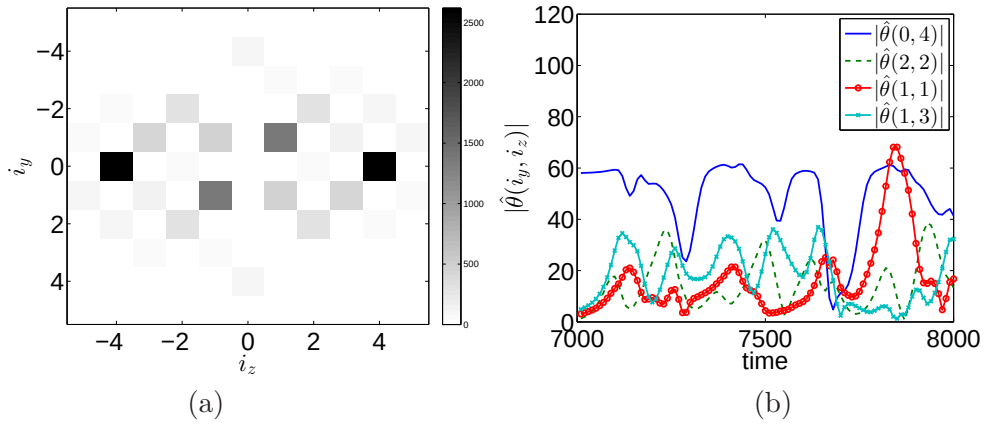

(a) (b)

Figure 6.25: (a) The time-averaged 2D Fourier spectral coefficient $|\hat{\theta}(i_y, i_z)|$ $(i_y, i_z = -5, 5)$ of the temperature fluctuations on the vertical plane $x = 0.0381$ for $t \in [7000, 8000]$; (b) Temporal evolution of the spectral coefficients $|\hat{\theta}(i_y, i_z)|$ on the plane $x = 0.0381$ for four modes: $Ra = 6300$

Arnoldi method to recompute some of these results. In particular we wish to examine how a small change k_z can affect the stability results. We find that the critical spanwise number and the corresponding most unstable mode are sensitive to the value of k_z, and that the critical Rayleigh numbers associated with mechanisms A and B are close to each other. To determine if and how a competition between the different patterns develops, we turn to direct numerical simulations for a particular choice of the plate periodic dimensions A_z and A_y, which corresponds to a fixed value of k_z and allows a range of suitable unstable wavenumbers k_y. All the results are summarized in Table 6.1. For the choice $A_z = 9$, we expect that the flow becomes unstable to the A mechanism around $Ra_{c2A} = 6056$. Owing to the cost of the simulations, a few Rayleigh numbers are selected around $Ra_{c2A} = 6056$. For a Rayleigh number $Ra = 6100$, which is close to the critical value, we observe the loss of stability of the 2D rolls, and also the appearance of mode A, but only as a transient. The solution then converges to a steady state which appears to be more consistent with instability B. This discrepancy with the linear stability predictions highlights the role of nonlinear simulations. Further bifurcations were then observed. The 3D steady flow associated with instability B becomes time-dependent at $Ra = 6150$, as the size of the defect associated with streamline excursions grows and shrinks periodically. Finally, the flow becomes temporally chaotic at $Ra = 6300$ but conserves a highly organized spatial structure, which is described with three Fourier modes corresponding to a superposition of the different

instability mechanisms brought to light by linear stability theory. This shows that although the validity range of its predictions can be severely limited - in our case the flow reaches temporal chaos for a Rayleigh number which is less than 10% higher than that associated with the primary instability - linear stability analysis remains useful beyond that domain, as it can help us to understand the physics of the flow as it becomes more complex and finally turbulent. This highlights the complementary role of linear stability analysis and nonlinear simulations.

Table 6.1: Summary of bifurcations and associated flow structures and symmetries for 3D simulations, $A_y = 8$, $A_z = 9$, $T = 1/f_1^{Large}$.

Ra	Nature of bifurcation	Flow structures	Dominant wavenumbers	Spatial symmetry Temporal symmetry
$Ra < Ra_c = 5708$		1D base flow		$O(2) \times O(2)$ steady
$Ra_c < Ra < Ra_{c2} = 6056$	supercritical circle pitchfork	2D corotating rolls	$k_y = \infty$ $k_z = 2.79$	$O(2) \times D_4$ steady
$Ra_{c2} < Ra \leq 6100$	supercritical	3D pinched rolls (A)	$k_y = \infty$, $k_z = 2.79$	$D_2 \times D_4$
($Ra = 6100$ at $t = 5500$)	circle pitchfork		$k_y = 1.57$, $k_z = 1.396$	steady
($Ra = 6100$ at $t > 7000$)	subcritical	3D broken rolls (B)	$k_y = \infty$, $k_z = 2.79$	$D_1 \times D_4$
			$k_y = 0.785$, $k_z = 0.698$	steady
$6150 \leq Ra \leq 6200$	supercritical Hopf	3D broken rolls	$k_y = \infty$, $k_z = 2.79$ $k_y = 0.785$, $k_z = 0.698$	$D_1 \times D_4$ T-periodic
$Ra = 6250$	period-doubling	3D pinched and broken rolls	$k_y = \infty$, $k_z = 2.79$ $k_y = 1.57$, $k_z = 1.396$ $k_y = 0.785$, $k_z = 0.698$	$D_1 \times D_4$ 2T-periodic
$Ra = 6300$		3D pinched and broken rolls	$k_y = \infty$, $k_z = 2.79$ $k_y = 1.57$, $k_z = 1.396$ $k_y = 0.785$, $k_z = 0.698$ $k_y = 0.785$, $k_z = 2.093$	no symmetry chaotic

Chapter 7

Conclusion

The focus of the present study is the sequence of instabilities leading to chaos for the air flow between two infinite differentially heated vertical plates. Our goal has been to examine the influence of three-dimensional effects for the transition to chaos. A mapping of that route has been established in two and three dimensions as shown in Table 7.1.

Owing to Squires' theorem, the nature of the first instability is two-dimensional. We confirmed that it occurs at a critical Rayleigh number Ra_c of 5708 with the critical vertical number $k_{zc} = 2.81$. By using multi-scale analysis, a Ginzburg-Landau equation was derived analytically, which is able to predict correctly the amplitude of the 2D rolls for the Rayleigh number within a limited range (10%) of Ra_c. It was also found that the nature of this first instability is absolute.

Then 2D DNS simulations were carried out to study the sequence of instabilities in the configuration $A_z = 10$. The base flow bifurcates to 2D steady rolls (secondary flow) through a supercritical circle pitchfork bifurcation at $Ra_c = 5708$. Then, a second bifurcation occurs at $Ra = 13500$. The flow becomes oscillatory, and the steady four-roll pattern turns into a periodic three-roll one with a characteristic frequency $f = 0.032$, which is similar to the natural frequency of the mixing layer when scaled with the inter-plate distance and reference velocity. When Ra is further increased, the temporal evolution of the three unsteady rolls becomes quasi-periodic, then apparently chaotic, while the characteristic frequency f remains dominant. As Ra is further increased beyond $Ra = 18000$, the flow becomes steady again, and the three oscillatory rolls give way to two steady rolls. This suggests that the occurrence of pure temporal chaos is limited by the development of a vertical instability, which leads to a long-wavelength modulation of the spatial pattern. The two steady rolls remain stable over a range of Rayleigh number, as no chaotic behavior is observed up to $Ra = 21000$.

A 3D DNS simulation was then carried out in a domain allowing some interaction between the vertical rolls ($A_z = 10$), but constrained in the transverse direction ($A_z = 1$). The situation differs from the 2D case by the onset of the second bifurcation, which occurs at a lower Rayleigh number $Ra_{c2} \sim 9980$. The 2D rolls become unstable and turn into a steady 3D pattern through a supercritical circle pitchfork bifurcation. The flow structure is characterized by secondary counter-rotating vortices connecting the principal convection rolls (tertiary flow). When the Rayleigh number is further increased past $Ra_{c3} \sim 11270$, the steady 3D pattern becomes oscillatory through a Hopf bifurcation, as the intensities of the transverse rolls and the counter-rotating vortices oscillate in quasi-phase opposition. A sequence of period-doubling bifurcations is observed at higher Rayleigh numbers. However, in the configuration $A_z = 10$, it is only a transient feature. The multiply periodic flow gives way to complex spatiotemporal dynamics when $Ra \geq 12100$ and a competition between different wavelengths is rapidly apparent in the flow pattern. The global behavior of heat transfer is established up to $Ra = 15000$, where Nu generally increases with Ra by at most 25%, with discontinuities as the flow goes through bifurcations.

The vertical dimension of the simulation domain was then reduced so as to allow for a single primary roll $A_z = 2.5$, hence constituting a minimal flow unit. In this case the sequence of period-doubling bifurcations becomes a persistent feature, through which the flow evolves towards temporal chaos. The flow is characterized by the modulated pulsation of a three-dimensional spatially localized structure, similar to the tertiary flow, which consists of an array of identical transverse rolls connected by secondary vortices or braids. The temporal behavior of the flow shares a large amount of common features with one-dimensional maps. Estimates for the Feigenbaum constant from the first few period-doubling bifurcations are reasonably close to the theoretical value. When Ra is further increased, a crisis-induced intermittency is observed, as the location of the flow structures randomly switches from one position to another, which is separated from the first one by half a vertical roll wavelength. A periodic window occurs for higher Rayleigh numbers, which then gives way to chaotic behavior at still higher Rayleigh numbers. The intermittency observed is reminiscent of that created by heteroclinic connections

and is likely to be the consequence of the $O(2)$ symmetry of the problem.

We then consider larger domains in both the vertical and transverse dimensions. We first determine the transverse size of the domain which will allow us to observe the development of instabilities predicted by linear stability theory. Linear stability analysis of the secondary flow using the Arnoldi method confirms the existence of two transverse instability mechanisms - denoted A and B - associated with two different spanwise wavenumbers. The growth rate of the two instabilities is very sensitive to the wavelength of the rolls (i.e the periodic height of the plate): for a small variation in the size of the rolls around their critical value, the A mechanism becomes more unstable than the B mechanism and vice-versa.

We choose to study the flow in the domain with $A_y = 8$ and $A_z = 9$. Only a few Rayleigh numbers were examined, owing to the computing cost of the simulations. Through a supercritical circle pitchfork bifurcation, the 2D rolls lead to a steady 3D pattern, consistent with that associated with mechanism A, which is predicted by linear stability theory. This 3D pattern has a $D_2 \times D_4$ symmetry. The flow consists of rolls with a wavy distortion in the transverse direction, and local pairing of the rolls in the vertical direction. However this 3D pattern is itself unstable to 3D disturbances. Through a subcritical instability, it turns into another steady 3D pattern, consistent with the B mechanism. The size of the rolls periodically shrinks and grows over the transverse direction. The location over which streamline excursions are observed is called the defect. This new 3D pattern has a $D_1 \times D_4$ symmetry. When Ra is further increased to 6150, the 3D pattern becomes oscillatory through a Hopf bifurcation. The defect region grows and shrinks periodically in this regime. At higher Rayleigh numbers, the temporal behavior of the flow becomes more complex. At $Ra = 6250$ a period-doubling bifurcation is observed, and both wavenumbers associated with instability A and B are present at all times. At $Ra = 6300$, the flow still contains only the few modes associated with the secondary instability mechanisms, but the dynamics of these modes is now chaotic.

To summarize, we have confirmed that 3D effects are essential for the transition of the flow to chaos in the periodic configuration. The influence of the domain dimensions on the transition to chaos was examined in detail. As can be expected, the instability mechanisms and

the sequence of bifurcations undergone by the flow crucially depend on the wavelengths allowed in the domain. It would be interesting to determine whether domains of reduced size may help us understand the physics of the flow in larger configurations and at higher Rayleigh numbers. Due to limited computer resources, we have been unable to simulate the flow in the larger domain at high Rayleigh numbers. It would be interesting to determine if the 3D structures consisting of rolls linked by braids of vorticity, found in the confined configuration $A_y = 1$ can also be found in the larger domain at $Ra > 11000$. In addition, although the predictions of linear stability may be valid for only a very small range of Rayleigh numbers, we have found in the large domain that linearly unstable modes play an important role in transition, and constitute the spatial backbone of the flow in the temporally chaotic regime. Whether coherent structures of the turbulent regime at very high Rayleigh numbers can also be described in terms of basic instability modes remains an open question.

Table 7.1: Summary of flow structures at different Rayleigh numbers in different configurations.

Ra	2D $A_z = 10$	3D $A_y = 1$ $A_z = 2.5$	3D $A_y = 1$ $A_z = 10$	3D $A_y = 8$, $A_z = 9$
$Ra < Ra_c = 5708$	1D base flow			
$Ra_c < Ra < Ra_{c2} = 6056$	2D steady corotating rolls			
$Ra_{c2} = 6056 < Ra \leq 6100$ ($Ra = 6100$ at $t = 5500$) ($Ra = 6100$ at $t > 7000$)	2D steady corotating rolls			3D steady flow broken rolls (A) broken rolls (B)
$6150 \leq Ra \leq 6200$	2D steady corotating rolls			oscillating 3D broken rolls
$Ra = 6250$	2D steady corotating rolls			period-doubling 3D pinched & broken rolls
$6300 \leq Ra \leq 6500$	2D steady corotating rolls			temporally chaotic flow 3D pinched & broken rolls
$6500 \leq Ra \leq 9980$	2D steady corotating rolls			
$9980 \leq Ra \leq 11270$	2D steady corotating rolls	steady 3D pinched rolls connected by vortices braids		
$11270 \leq Ra \leq 12000$	2D steady corotating rolls	oscillating 3D pinched rolls connected by vortices braids		
$Ra \geq 12100$	2D steady corotating rolls	period-doubling temporal chaos	Eckhaus-like instability temporal chaos	
$12546 \leq Ra \leq 13500$	2D steady corotating rolls	crisis-induced intermittency temporal chaos		
$13500 \leq Ra \leq 15300$	3 oscillating rolls			
$15400 \leq Ra \leq 15600$	3 quasiperiodic oscillating rolls			
$15700 \leq Ra \leq 17000$	3 chaotic oscillating rolls			
$18000 \leq Ra \leq 21000$	2 steady rolls with unequal size			

Appendix A

Operators expanded in the multi-scale analysis

In the weakly nonlinear analysis section, the operators M, L and b in the system Eq. (3.9) are expanded by the asymptotic expansions as Eq. (3.21)-Eq. (3.23). The operators developed at different orders of ϵ read as

$$M_0 = \begin{bmatrix} \nabla_0^2 & 0 \\ 0 & 1 \end{bmatrix}; \qquad M_1 = \begin{bmatrix} 2\frac{\partial}{\partial z_0}\frac{\partial}{\partial z_1} & 0 \\ 0 & 0 \end{bmatrix}; \qquad M_2 = \begin{bmatrix} \frac{\partial^2}{\partial z_1^2} & 0 \\ 0 & 0 \end{bmatrix}; \tag{A.1}$$

$$L_0 = \begin{bmatrix} \frac{Pr}{\sqrt{Ra_c}}\nabla_0^4 - W\frac{\partial}{\partial z_0}\nabla_0^2 + \frac{\partial^2 W}{\partial x^2}\frac{\partial}{\partial z_0} & Pr\frac{\partial}{\partial x} \\ \frac{\partial \Theta}{\partial x}\frac{\partial}{\partial z_0} & \frac{1}{\sqrt{Ra_c}}\nabla_0^2 - W\frac{\partial}{\partial z_0} \end{bmatrix}; \tag{A.2}$$

$$L_1 = \begin{bmatrix} 4\frac{Pr}{\sqrt{Ra_c}}\frac{\partial}{\partial z_0}\frac{\partial}{\partial z_1}\nabla_0^2 - W\frac{\partial}{\partial z_1}\nabla_0^2 - 2W\frac{\partial}{\partial z_1}\frac{\partial^2}{\partial z_0^2} + \frac{\partial^2 W}{\partial x^2}\frac{\partial}{\partial z_1} & 0 \\ \frac{\partial \Theta}{\partial x}\frac{\partial}{\partial z_1} & \frac{2}{\sqrt{Ra_c}}\frac{\partial}{\partial z_0}\frac{\partial}{\partial z_1} - W\frac{\partial}{\partial z_1} \end{bmatrix}; \tag{A.3}$$

$$L_2 = \begin{bmatrix} 2\frac{Pr}{\sqrt{Ra_c}}\frac{\partial^2}{\partial z_1^2}(\nabla_0^2 + 2\frac{\partial^2}{\partial z_0^2}) - 3W\frac{\partial}{\partial z_0}\frac{\partial^2}{\partial z_1^2} & 0 \\ 0 & \frac{1}{\sqrt{Ra_c}}\frac{\partial^2}{\partial z_1^2} \end{bmatrix}$$
$$+ \begin{bmatrix} -\frac{1}{2}\frac{Pr}{\sqrt{Ra_c^3}}\nabla_0^4 - \frac{W}{2Ra_c}\frac{\partial}{\partial z_0}\nabla_0^2 + \frac{1}{2Ra_c}\frac{\partial^2 W}{\partial x^2}\frac{\partial}{\partial z_0} & 0 \\ 0 & -\frac{1}{2}\frac{1}{\sqrt{Ra_c^3}}\nabla_0^2 - \frac{W}{2Ra_c}\frac{\partial}{\partial z_0} \end{bmatrix} \tag{A.4}$$

$$b_{0,\psi}(\phi_\alpha,\phi_\beta)=\left(\frac{\partial\psi_\alpha}{\partial z_0}\frac{\partial}{\partial x}-\frac{\partial\psi_\alpha}{\partial x}\frac{\partial}{\partial z_0}\right)\nabla_0^2\psi_\beta \tag{A.5}$$

$$b_{0,\theta}(\phi_\alpha,\phi_\beta)=\left(\frac{\partial\psi_\alpha}{\partial z_0}\frac{\partial}{\partial x}-\frac{\partial\psi_\alpha}{\partial x}\frac{\partial}{\partial z_0}\right)\theta_\beta \tag{A.6}$$

$$b_{1,\psi}(\phi_\alpha,\phi_\beta)=\left(\frac{\partial\psi_\alpha}{\partial z_1}\frac{\partial}{\partial x}-\frac{\partial\psi_\alpha}{\partial x}\frac{\partial}{\partial z_1}\right)\nabla_0^2\psi_\beta+2\left(\frac{\partial\psi_\alpha}{\partial z_0}\frac{\partial}{\partial x}-\frac{\partial\psi_\alpha}{\partial x}\frac{\partial}{\partial z_0}\right)\frac{\partial}{\partial z_0}\frac{\partial}{\partial z_1}\psi_\beta \tag{A.7}$$

$$b_{1,\theta}(\phi_\alpha,\phi_\beta)=\left(\frac{\partial\psi_\alpha}{\partial z_1}\frac{\partial}{\partial x}-\frac{\partial\psi_\alpha}{\partial x}\frac{\partial}{\partial z_1}\right)\theta_\beta \tag{A.8}$$

where $\nabla_0=\frac{\partial^2}{\partial x^2}+\frac{\partial^2}{\partial z_0^2}$, Ra_c is the critical Rayleigh number found in the linear stability analysis, W is the vertical velocity of the base flow, and Θ is the temperature of the base flow.

The coefficients of Eq. (3.72) are presented as follows:

$$c_1=\begin{bmatrix}c_{11}\\c_{12}\end{bmatrix},\qquad c_2=\begin{bmatrix}c_{21}\\c_{22}\end{bmatrix},\qquad c_3=\begin{bmatrix}c_{31}\\c_{32}\end{bmatrix},\qquad c_4=\begin{bmatrix}c_{41}\\c_{42}\end{bmatrix} \tag{A.9}$$

$$c_{11}=-(\hat{\psi}_1''-k_c^2\hat{\psi}_1) \tag{A.10}$$

$$c_{12}=-\hat{\theta}_1 \tag{A.11}$$

$$c_{21}=-\frac{1}{2}Ra_c^{-1.5}Pr(\hat{\psi}_1^{(4)}-2k_c^2\hat{\psi}_1''+k_c^4\hat{\psi}_1)$$
$$-\frac{1}{2Ra_c}(W(ik_c\hat{\psi}_1''-ik_c^3\hat{\psi}_1)-\frac{\partial^2W}{\partial x^2}ik_c\hat{\psi}_1) \tag{A.12}$$

$$c_{22}=-\frac{1}{2}Ra_c^{-1.5}(\hat{\theta}_1''-k_c^2\hat{\theta}_1)-\frac{1}{2Ra_c}Wik_c\hat{\theta}_1 \tag{A.13}$$

$$c_{31}=2ik_c\hat{\psi}_1^{*(3)}\hat{\psi}_{21}-2ik_c^3\hat{\psi}_1'^*\hat{\psi}_{21}+ik_c\hat{\psi}_1''^*\hat{\psi}_{21}'-ik_c^3\hat{\psi}_1^*\hat{\psi}_{21}'-ik_c\hat{\psi}_1''\hat{\psi}_{22}'+ik_c^3\hat{\psi}_{22}'\hat{\psi}_1$$
$$+ik_c\hat{\psi}_1\hat{\psi}_{22}^{(3)}+4ik_c^3\hat{\psi}_1^*\hat{\psi}_{21}'-ik_c\hat{\psi}_1^*\hat{\psi}_{21}^{(3)}-2ik_c\hat{\psi}_1'^*\hat{\psi}_{21}''+8ik_c^3\hat{\psi}_1'^*\hat{\psi}_{21} \tag{A.14}$$

$$c_{32}=2ik_c\hat{\psi}_{21}\hat{\theta}_1'^*-ik_c\hat{\psi}_{22}'\hat{\theta}_1+ik_c\hat{\psi}_{21}'\hat{\theta}_1^*+ik_c\hat{\psi}_1\hat{\theta}_{22}'-ik_c\hat{\psi}_1^*\hat{\theta}_{21}'-2ik_c\hat{\psi}_1'^*\hat{\theta}_{21} \tag{A.15}$$

$$c_{41}=\frac{2Pr}{\sqrt{Ra_c}}(\hat{\psi}_1''-3k_c^2\hat{\psi}_1)-3Wik_c\hat{\psi}_1-2C_gik_c\hat{\psi}_1$$
$$+\left(-4ik_c^3\frac{Pr}{\sqrt{Ra}}+3Wk_c^2+\frac{\partial^2W}{\partial x^2}\right)\hat{\psi}_{24}+\left(\frac{4Pr}{\sqrt{Ra}}ik_c-W\right)\hat{\psi}_{24}''-C_g\left(\hat{\psi}_{24}''-k_0^2\hat{\psi}_{24}\right) \tag{A.16}$$

$$c_{42}=\frac{1}{\sqrt{Ra_c}}\hat{\theta}_1+\frac{\partial\Theta}{\partial x}\hat{\psi}_{24}+\left(\frac{2}{\sqrt{Ra}}ik_c-W\right)\hat{\theta}_{24}-C_g\hat{\theta}_{24} \tag{A.17}$$

where k_c is the critical wavenumber found in the linear stability analysis and C_g is the group

velocity calculated in the problem at order ϵ^2. $\hat{\psi}^*$ denotes the complex conjugate of $\hat{\psi}$, and $\hat{\psi}^{(n)}$ denotes the n-th derivatives of $\hat{\psi}$ with respect to x. $\hat{\psi}_1$ and $\hat{\theta}_1$ are the stream function and temperature components of the eigenvector $\hat{\psi}_1$ obtained in the linear stability analysis ($\phi_1 = [\psi, \hat{\theta}]^T$).

Bibliography

[1] H. Bénard. Les tourbillons cellulaires dans une nappe liquide. *Rev. Gén. Sci pures et appl.*, 11:1261–1271 & 1309–1328, 1900.

[2] Lord Rayleigh. On the convective currents in a horizontal layer of fluid when the higher temperature is on the under side. *Phil. Mag.*, 32:529–546, 1916.

[3] P. Manneville. Rayleigh-Bénard convection: Thirty years of experimental, theoretical, and modeling work. In I. Mutabazi, J. Wesfreid, and E. Guyon, editors, *Dynamics of Spatio-Temporal Cellular Structures*, volume 207 of *Springer Tracts in Modern Physics*, pages 41–65. Springer New York, 2006.

[4] G.K Batchelor. Heat transfer by free convection across a closed cavity between vertical boundaries at different temperatures. *Quart. Appl. Math*, 12(3):209–233, 1954.

[5] A.E. Gill and A. Davey. Instability of a buoyancy-driven system. *J. Fluid Mech.*, 35(4):775–798, 1969.

[6] S. Paolucci and D.R. Chenoweth. Transition to chaos in a differentially heated vertical cavity. *J. Fluid Mech.*, 201:379–410, 1989.

[7] P. Le Quéré. Onset of unsteadiness, routes to chaos and simulations of chaotic flows in cavities heated from the side: a review of present status. In *10th Intl. Heat Trans. Conf.*, volume 1 of *I Chem E Symposium Series*, pages 281–296, 1994.

[8] S. Xin and P. Le Quéré. Direct numerical simulation of two-dimensional chaotic natural convection in a differentially heated cavity of aspect ratio 4. *J. Fluid Mech.*, 304:87–118, 1995.

[9] E.R.G. Eckertf and W.O. Carlson. Natural convection in an air layer enclosed between two vertical plates with different temperatures. *International Journal of Heat and Mass Transfer*, 2:106–120, 1961.

[10] J.W. Elder. Laminar free convection in a vertical slot. *J. Fluid Mech.*, 23(1):77–98, 1965.

[11] C.M. Vest and V.S. Arpaci. Stability of natural convection in a vertical slot. *J. Fluid Mech.*, 36:1–15, 1969.

[12] Y. Oshima. Experimental studies of free convection in a rectangular cavity. *J. Phys. Soc. Japan*, 30(3):872–882, 1971.

[13] S. A. Korpela. A study on the effect of Prandtl number on the stability of the conduction regime of natural convection in an inclined slot. *International Journal of Heat and Mass Transfer*, 17(2):215 – 222, 1974.

[14] R.F. Bergholz. Instability of steady natural convection in a vertical fluid layer. *J. Fluid Mech.*, 84(4):743–768, 1978.

[15] J. Tao and F. Zhuang. Absolute and convective instabilities of the natural convection in a vertical heated slot. *Phys. Rev. E*, 62(6):7957–7960, 2000.

[16] P.G. Daniels and M. Weinstein. Nonlinear stability of convective flow between heated vertical planes. *J. Eng. Math.*, 24:179–188, 1989.

[17] J.M. Cornet and C.H. Lamarque. Nonlinear behavior of the instability of steady natural convection in a vertical air layer. *Mech. Res. Comm*, 24:179–188, 1997.

[18] J. Mizushima and K. Gotoh. Nonlinear evolution of the disturbance in a natural convection induced in a vertical fluid layer. *J. Phys. Soc. Japan*, 52:1206–1214, 1983.

[19] J. Mizushima and Y. Saito. Equilibrium characteristics of the secondary convection in a vertical fluid layer between two flat plates. *Fluid Dyn. Res.*, 2:183–191, 1987.

[20] J. Mizushima. Equilibrium solution of the secondary convection in a vertical fluid layer between two flat plates. *Fluid Dyn. Res.*, 5:289–299, 1990.

[21] J. Mizushima and H. Tanaka. Transition routes of natural convection in a vertical fluid layer. *Phys. Fluids*, 14:21–24, 2002.

[22] J. Mizushima and H. Tanaka. Transition routes of natural convection in a vertical fluid layer. *J. Phys. Soc. Jap.*, 71:2898–2906, 2002.

[23] S. Xin. *Simulation Numérique de Convection Naturelle Turbulente*. Ph.D. thesis, Université Paris VI, 1993.

[24] D. R. Chenoweth and S. Paolucci. Gas flow in vertical slots with large horizontal temperature differences. *Phys. Fluids*, 28:2375–2374, 1985.

[25] D. R. Chenoweth and S. Paolucci. Natural convection in an enclosed vertical air layer with large horizontal temperature differences. *J. Fluid Mech*, 169:173–210, 1986.

[26] P. Le Quéré. A note on multiple and unsteady solutions in a tall cavity. *ASME J. Heat Transfer*, 112:965, 1990.

[27] S. Wakitani. Flow patterns of natural convection in an air-filled vertical cavity. *Phys. Fluids.*, 10:1924, 1998.

[28] H. Gunes. Low-order dynamical models of thermal convection in high-aspect-ratio enclosures. *Fluid Dyn. Res.*, 30:1–30, 2002.

[29] B. Lartigue, S. Lorente, and B. Bourret. Multicellular natural convection in a high aspect ratio cavity: experimental and numerical results. *Int. J. Heat Mass Transfer*, 43:3157–3170, 2000.

[30] J. L. Wright, H. Jin, K. G. T. Hollands, and D. Naylor. Flow visualization of natural convection in a tall, air-filled vertical cavity. *Int. J. Heat Mass Transfer*, 49:889–904, 2006.

[31] M. Nagata and F.H. Busse. Three-dimensional tertiary motions in a plane shear layer. *J. Fluid Mech.*, 135:1–26, 1983.

[32] A. Chait and S.A. Korpela. The secondary flow and its stability for natural convection in a tall vertical enclosure. *J. Fluid Mech.*, 200:189–216, 1989.

[33] R.M. Clever and F.H. Busse. Tertiary and quarternary solutions for convection in a vertical fluid layer heated from the side. *Chaos, Solitons, Fractals*, 5(10):1795–1803, 1995.

[34] A. Suslov and S. Paolucci. Stability of non-boussinesq condition via the complex Ginzburg-Landau model. *Fluid Dyn. Res.*, 35:159–203, 2004.

[35] A. Suslov and S. Paolucci. Nonlinear analysis of convection flow in a tall vertical enclosure under non-Boussinesq conditions. *J. Fluid Mech.*, 344:1–41, 1997.

[36] J.-P. Eckmann. Roads to turbulence in dissipative dynamical systems. *Reviews of Modern Physics*, 53(4):643–654, 1981.

[37] J. Maurer and A. Libchaber. Rayleigh-Bénard convection experiment in liquid helium; frequency locking and onset of turbulence. *Le Journal de Physique Lettres*, 40:419–423, 1979.

[38] M. Giglio, S. Musazzi, and U. Perini. Transition to chaotic behavior via a reproducible sequence of period-doubling bifurcations. *Phys. Rev. Lett.*, 47(4):243–246, 1981.

[39] Y. Pomeau and P. Manneville. Intermittent transition to turbulence in dissipative dynamical systems. *Communication in Mathematical Physics*, 74:189–97, 1980.

[40] P. Bergé, M. Dubois, P. Manneville, and Y. Pomeau. Intermittency in Rayleigh-Bénard convection. *Le Journal de Physique - Lettres*, 41:149–153, 1980.

[41] R.J.A. Janssen and R.A.W.M. Henckes. Influence of Prandtl number on instability mechanisms and transition in a differentially heated square cavity. *J. Fluid Mech.*, 290:319–344, 1995.

[42] H. Ishida, S. Kawase, and H. Kimoto. The second largest Lyapunov exponent and transition to chaos of natural convection in a rectangular cavity. *Int. J. Heat Mass Transfer*, 49:5035–5048, 2006.

[43] A. Lizee and J.I.D. Alexander. Chaotic thermovibrational flow in a laterally heated cavity. *Phys. Rev. E*, 56(4):4152–4156, 1997.

[44] D.A. Bratsun, A.V. Zyuzgin, and G.F. Putin. Non-linear dynamics and pattern formation in a vertical fluid layer heated from the side. *International Journal of Heat and Fluid Flow*, 24(6):835 – 852, 2003.

[45] J. R. Phillips. Direct simulations of turbulent unstratified natural convection in a vertical slot for Pr=0.71. *Int. J. Heat Mass Transfer*, 39(12):2485–2494, 1996.

[46] J.W. Elder. Turbulent free convection in a vertical slot. *J. Fluid Mech.*, 23:99–111, 1965.

[47] T.A.M. Versteegh and F.T.M. Nieuwstadt. Turbulent budgets of natural convection in an infinite, differentially heated, vertical channel. *Int. J. Heat Fluid Flow*, 19:135–149, 1998.

[48] T.A.M. Versteegh and F.T.M. Nieuwstadt. A direct numerical simulation of natural convection between two infinite vertical differentially heated walls scaling laws and wall functions. *Int. J. Heat Mass Transfer*, 42:3673–3693, 1999.

[49] M. Wang, S. Fu, and G. Zhang. Large-scale spiral structures in turbulent thermal convection between two vertical plates. *Phys. Rev. E*, 66:066306, Dec 2002.

[50] P. Hall. Vortex-wave interactions: long-wavelength streaks and spatial localization in natural convection. *J. Fluid Mech.*, 703:99–110, 2012.

[51] A. Sergent and P. Le Quéré. Long time evolution of large scale patterns in a rectangular Rayleigh-Bénard cell. In K. Bajer, J. Kopec, M. Kursa, K. Kwiatkowski, and P. Podziemski, editors, *13th European Turbulence Conference(ETC), 12-15 September 2011, Warsaw*, volume 318 of *Journal of Physics Conference Series*, 2011.

[52] B. Podvin and A. Sergent. Proper orthogonal decomposition investigation of turbulent Rayleigh-Bénard convection in a rectangular cavity. *Phys. Fluids*, 23(10):105106, 2012.

[53] S. Xin, J. Chergui, and P. Le Quéré. 3D spectral parallel multi-domain computing for natural convection flows. In D. Tromeur-Dervout, G. Brenner, D.R. Emerson, and J. Erhel, editors, *Parallel Computational Fluid Dynamics 2008*, volume 74 of *Lecture Notes in Computational Science and Engineering*, pages 163–171. Springer Berlin Heidelberg, 2011.

[54] P. Le Quéré. Numerical methods for incompressible flow. Lecture Notes, Université Pierre et Marie Curie, Paris, France, 2010.

[55] G. Labrosse. *Méthodes spectrales: méthodes locales, méthodes globales, problèmes d'Helmholtz et de Stokes, équations de Navier-Stokes*, chapter 12, pages 168–170. Technosup. Ellipses, 2011.

[56] P. Haldenwang, G. Labrosse, S. Abboudi, and M. Deville. Chebyshev 3-D spectral and 2-D pseudospectral solvers for the Helmholtz equation. *J. Comput. Phys.*, 55:115–128, 1984.

[57] D.W. Ruth. On the transition to transverse rolls in an infinite vertical fluid layer - a power series solution. *Int. J. Heat Mass Transfer*, 22:1199–1208, 1979.

[58] C. Cossu. Introduction to hydrodynamic instabilities. Lecture Notes, Ecole Polytechnique, Palaiseau, France, 2009.

[59] P. Huerre. Open shear flow instabilities. In G.K.Batchelor, H.K. Moffatt, and M.G. Worster, editors, *Perspectives in fluid dynamics A collective introduction to current research*, pages 159–229. Cambridge University Press, 2000.

[60] R.D. Henderson and D. Barkley. Secondary instability in the wake of a circular cylinder. *Phys. Fluids*, 8:1683–1685, 1996.

[61] J.C.R. Hunt, A.A. Wray, and P. Moin. *Eddies, streams, and convergence zones in turbulent flows*, volume 1, pages 193–208. Center for Turbulence Research, Stanford University, 1988.

[62] C. Ho and P. Huerre. Perturbed free shear layers. *Ann. Rev. Fluid Mech.*, 16:365–424, 1984.

[63] S. Randrianifahanana. Écoulement de convection naturelle en grande cavité. Internship report, Master 1, Université Pierre et Marie Curie, 2013.

[64] J. Jiménez and P. Moin. The minimal flow unit in near-wall turbulence. *Journal of Fluid Mechanics*, 225:213–240, 4 1991.

[65] P. Manneville. Review course on instabilities in hydrodynamics. Lecture notes, Instabilities in Hydrodynamics 2012 Summer School, 2012.

[66] J. C. Sprott. *Chaos and Time-Series Analysis*, chapter 5. Oxford University Press, 2003.

[67] E. Ott. *Chaos in Dynamical Systems*. Cambridge University Press, 2002.

[68] C. Grebogi, E. Ott, F. Romeiras, and J. Yorke. Critical exponent for crisis-induced intermittency. *Phys. Rev. A*, 36:5365–5380, 1987.

[69] M.J.Feigenbaum. Universal behavior in nonlinear systems. *Los Alamos Sciences*, 1:4–27, 1980.

[70] E.N. Lorenz. Deterministic nonperiodic flow. *J. ATM. SCI.*, 20:130–141, 1963.

[71] P. Manneville. *Instabilities, chaos and turbulence*. Imperial College Press, 2004.

[72] C. Grebogi, E. Ott, and J. Yorke. Chaotic attractor in crisis. *Phys. Rev. Lett.*, 48:1507–1510, 1982.

[73] C. Grebogi, E. Ott, and J. Yorke. Crisis, sudden changes in chaotic attractor and chaotic transients. *Physica D*, 7:181–200, 1983.

[74] G. Benettin, L. Galgani, A. Giorgilli, and J. Strelcyn. Lyapunov characteristics exponent for smooth dynamical system and for hamiltonian system: a method for computing all of them. *Meccanica*, 15:9–30, 1980.

[75] J.D. Scheel. *Rotating Rayleigh-Bénard Convection*. Ph.D. thesis, California Institut of Technology, 2007.

[76] J. D. Scheel and M. C. Cross. Lyapunov exponents for small aspect ratio Rayleigh-Bénard convection. *Phys. Rev. E*, 74:066301, Dec 2006.

[77] Z. Gao, A. Sergent, B. Podvin, S. Xin, P. Le Quéré, and L.S. Tuckerman. On the transition to chaos of natural convection between two infinite differentially heated vertical plates. *Phys. Rev. E*, 88:023010, Aug 2013.

[78] I. Melbourne, P. Chossat, and M. Golubitsky. Heteroclinic cycles involving periodic solutions in mode interactions with O(2) symmetry. *Proceedings of the Royal Society of Edinburgh: Section A Mathematics*, 113:315–345, 1989.

[79] D. Armbruster, J. Guckenheimer, and P. Holmes. Heteroclinic cycles and modulated travelling waves in systems with O(2) symmetry. *Physica D*, 29:257–282, 1987.

[80] C. Gissinger. A new deterministic model for chaotic reversals. *The European Physical Journal B*, 85(4):1–12, 2012.

[81] B. Gallet, J. Herault, C. Laroche, F. Pétrélis, and S. Fauve. Reversals of a large scale field generated over a turbulent background. *Geophysical & Astrophysical Fluid Dynamics*, 106:468–492, 2012.

[82] J.C. Sommerer, W.L. Dittio, C. Grebogi, E. Ott, and M.L.Spano. Experimental confirmation of the theory for critical exponent of crisis. *Physics Letters A*, 153:105–109, 1991.

[83] S. Xin and P. Le Quéré. Linear stability analysis of natural convection flows in a differentially heated square cavity with conducting horizontal walls. *Phys. Fluids*, 13(9):2529–2542, 2001.

[84] C. K. Mamun and L. S. Tuckerman. Asymmetry and Hopf bifurcation in spherical couette flow. *Phys. Fluids*, 7:80–91, 1995.

[85] S. Xin. Instabilité de convection naturelle en cavité et méthodes numériques adaptées. *11e Ecole de printemps de Mécanique des Fluides Numériques, Oléron, France*, June 7-13th, 2009.